A MEASUREMENT

OF THE K^0 (890) RADIATIVE WIDTH

BY

DUNCAN L. CARLSMITH

DECEMBER,1984

THE UNIVERSITY OF CHICAGO

A MEASUREMENT OF THE K0 (890) RADIATIVE WIDTH

A DISSERTATION SUBMITTED TO THE FACULTY OF THE DIVISION OF PHYSICAL SCIENCES IN CANDIDACY FOR THE DEGREE OF DOCTOR OF PHILOSOPHY

DEPARTMENT OF PHYSICS

BY

DUNCAN L. CARLSMITH

CHICAGO,ILLINOIS

DECEMBER,1984



ACKNOWLEDGEMENTS

I wish to thank my thesis advisor Bruce Winstein for suggesting this measurement and for his support and assistance in carrying out the experiment and the data analysis.

All of the collaborators on the FNAL E617 experiment deserve acknowledgement. The University of Chicago collaborators were Robert Bernstein, Gregory Bock, David Coupal, James Cronin, George Gollin, Hamish Norton, Wen Keling, Koichiro Nishikawa, and Bruce Winstein. Collaborators from Saclay were Bernard Peyaud, René Turlay, and Armand Zylberstein.

Special thanks go to R. Lynn Keller for her encouragement and patience.

For help in the design and construction of the apparatus, I thank the University of Chicago engineering services group, Thomas Shea and Adrian Alexander in particular, and the Enrico Fermi Institute electronics development group. Fermilab and the Meson Area staff provided valuable assistance. This work was supported by the National Science Foundation.

Table of Contents

	page
ACKNOWLEGDEMENTS	. ii
LIST OF ILLUSTRATIONS	. v
LIST OF TABLES	ix
ABSTRACT	. x
Chapter	
I. INTRODUCTION TO VECTOR MESON RADIATIVE DECAYS	1
II. PRINCIPLE OF THE MEASUREMENT	4
A. Introduction B. Production of Mesons in the Electromagnetic Field of a Nucleus C. Backgrounds Resulting From Strong Production Processes III. EXPERIMENTAL TECHNIQUE A. General Considerations B. Overview of the Beamline and Apparatus	. 17
C. Data Aquisition Hardware D. Data Sets and Triggers E. Alignment and Calibration of the Apparatus F. Simulation of the Experiment IV. DATA REDUCTION	. 64
A. Event Reconstruction and Event Selection B. $K_L \rightarrow \pi^+ \pi^- \pi^0$ Events C. $K' \rightarrow K_S \pi^o$ Events D. Neutron Background Events	
V. NORMALIZATION OF OBSERVED K* DECAYS	. 102
VI. EXTRACTION OF THE K° (890) RADIATIVE WIDTH	. 129
VII. SUMMARY AND CONCLUSIONS	. 150

TABLE OF CONTENTS--(continued)

Appendices	
A. CALCULATION OF RADIATIVE DECAYS IN THE QUARK MODEL	154
B. SEARCH FOR COULOMB PRODUCTION OF THE K° (1430)	157
REFERENCES	161

LIST OF ILLUSTRATIONS

Pigu	nre	page
1.	Single photon exchange diagram describing the transition	
	$a \rightarrow a'$ induced by the electromagnetic field of a nucleus A	7
2.	Production and decay of the K ⁰ (890) in the	
	Gottfried-Jackson frame.	9
3.	Diagrams and amplitudes describing the Coulomb production	
	and strong decay of the K^{o} and K^{o} .	11
4.	Beam profiles as determined from reconstructed $K\pi_3$ events.	21
5.	Schematic of the apparatus.	23
6.	Front and side views of a drift chamber.	25
7.	G hodoscope segmentation used in the K* trigger	39
8.	Lead glass segmentation used in the K* trigger.	41
9.	Typical pattern of energy deposition in the lead glass for a	
	$\pi^+\pi^-\pi^o$ event	43
10.	Integral of the distribution of drift times for single muon events	49
11.	Distribution of the ratio (E/P) of the energy deposited in the lead	
	glass to the momentum measured in the drift chambers for a sample	
	of tracks from the charged mode data.	51

LIST OF ILLUSTRATIONS--(continued)

		page
12.	Lead glass response to electrons.	55
13.	Variation of a) the mean and b) root-mean-square width of the	
	π^0 mass with the least energetic of the two photons	
	for identified $K\pi_3$ decays.	57
14.	Energy dependance of the lead glass position resolution as deduced	
	from electron initiated showers.	59
15.	Distribution of the distance of closest approach of tracks	
	for $K\pi_3$ decays.	67
16.	Distribution of a) the $\pi^+\pi^-$ invariant mass and b) the	
٠	reconstructed vertex along the beam direction for events	
	in which two charged particles and one π^0	
	were reconstructed	71
17.	Distribution of the $\pi^+\pi^-$ invariant mass for $K\pi_3$ events.	73
18.	Distribution of the $\gamma\gamma$ invariant mass for $K\pi_3$ events.	75
19.	Distribution of the $\pi^+\pi^-\pi^0$ mass for $K\pi_3$ events.	77
20.	Transverse momentum distributions for the two targets	
	for $K\pi_3$ events.	79
21.	Vertex distribution for $K\pi_3$ events before the application of the	
	upstream vertex cut.	81
22.	Distribution of the $\pi^+\pi^-$ invariant mass in the neighborhood	
	of the K_S mass.	85

LIST OF ILLUSTRATIONS--(continued)

		page
23.	Distribution of the $K_S\pi^0$ invariant mass for the K_S rich	
	event sample for various bins of t' for the two targets.	8
24.	Distribution of the K_S vertex along the beam direction	
	for $K^{\bullet} \to K_S \pi^{\bullet}$ events in the mass	
	range .8-1.0 GeV^2 and with $t' < .01 GeV^2$.	89
25.	Distribution of the reconstructed π^0 mass	
	for $K^{\bullet} \rightarrow K_S \pi^{\bullet}$ events.	91
26.	Decay angular distributions in the Gottfried-Jackson frame	
	for $K^{\bullet} \rightarrow K_S \pi^{\bullet}$ decays.	93
27.	Transverse momentum distributions for K^{\bullet} events in the upstream	
	and downstream regions of the decay volume for the two	
	targets.	9
28.	Proton-pion invariant mass distribution.	99
29.	Distribution of the $\pi^+\pi^-\pi^0$ mass for K_S wing events.	101
30.	Momentum dependance of the acceptance for K^{0} , $K\pi_3$,	
	and Ke ₃ decays.	107
31.	Distribution of the variable BRAC (defined in the text) for	
	$K \rightarrow \pi e \nu$ decays.	113
32.	Distribution of the total charged momentum, $ \vec{p}_{\pi} + \vec{p}_{\epsilon} $,	
	for Ke ₃ decays.	115
33.	Distribution of the K_L momentum for unambiguous Ke_3 events	117

LIST OF ILLUSTRATIONS--(continued)

		page
34.	K_L momentum distribution for $K\pi_3$ decays.	119
35.	Some distributions for $K_L \rightarrow \pi^+\pi^-$ decays.	121
36.	Momentum distribution for identified $K_L \rightarrow \pi^+\pi^-$ events	123
37.	Comparison of momentum spectrum shape as deduced from Ke ₃	
	events with the results of a previous measurement.	125
38	Distribution of the $K_S\pi^0$ mass for events with t'<.01 GeV ²	133
39.	Transverse momentum distribution for $K_L \rightarrow \pi^+\pi^-\pi^0$ decays	137
40.	Experimental K^* differential production cross section	
	for the copper target.	139
41.	Experimental K' differential production cross section	
	for the lead target.	141
42.	Energy dependance of the $K^{os}(890)$ production cross section	
	integrated from t'=0 to t'=.01 GeV ² .	143

LIST OF TABLES

Table	page
1. Properties of the Targets	26
2. Properties of the Drift Chambers	27
3. Properties of the Lead Glass	28
4. Normalization and Correction Factors	103
5. Parameters Describing the K_L Momentum Spectrum	110
6. Calculation of the $K_L \rightarrow \pi^+ \pi^-$ Branching Ratio	127
7. Calculation of the $K_L \rightarrow \pi^+ \pi^- \pi^0$ Branching Ratio	128
8. Results of Fits to the Differential Production Cross Section	145
9. Systematic Error Estimates	147

ABSTRACT

Coulomb production of the K^{o} (890) was observed in the 100-200 GeV energy range. From the production cross section, the radiative width of the K^{o} (890) was found to be $116.5\pm5.7\pm5.1$ KeV in reasonable agreement with the result of a previous less precise measurement and with the prediction of the naive quark model if the magnetic moments of the constituent quarks are deduced from baryon magnetic moments.

CHAPTER I

INTRODUCTION TO VECTOR MESON RADIATIVE DECAYS

C. Becchi and G. Morpugo, in 1965, were the first to point out that radiative decays of vector (V) mesons to pseudoscalar (P) mesons ($J^P=1^-\rightarrow J^P=0^-+\gamma$) are accessible to experiment and sensitive to the magnetic moments of the constituent quarks. A number of vector meson radiative decay widths have since been measured and the phenomenology of $VP\gamma$ transitions has been analyzed in a variety of quark models. In the simplest model, the pseudoscalar and vector states are regarded as S-wave bound states of a quark and an anti-quark in the singlet and triplet spin states respectively. The rate for the spontaneous spin-flip transition in which a photon with wavevector \vec{k} and polarization vector $\vec{\epsilon}$ is emitted is calculated assuming a transition amplitude of the form:

$$M_{VP} \approx \langle V | \sum_{q} \mu_{q} \vec{\sigma}_{q} \cdot (\vec{\epsilon} \times \vec{k}) e^{i \vec{k} \cdot \vec{z}_{q}} | P \rangle$$
 (1.1)

where $\mu_q = e_q/2m_q$ is the magnetic moment of the q-th quark and $\vec{\sigma}_q$ represents the Pauli matrices. In the long wavelength approximation, and in case there is no quark flavor mixing in the wavefunctions that describe the vector and pseudoscalar states, the vector meson radiative width is given by:

$$\Gamma(V \to P + \gamma) = \frac{4}{3} k^3 \frac{E_P}{m_V} |\mu_q - \mu_{\bar{q}}|^2 |I_{VP}|^2$$
 (1.2)

where m_V is the mass of the vector meson, $E_P = \sqrt{m_P^2 + k^2}$ is the recoil energy of the pseudoscalar meson, and $I_{VP} = \int \psi_V^* \psi_P \ dV$ is the overlap integral of the spatial wavefunctions. The factor E_P/m_V is a relativistic phase space correction to the usual k^3 dependance of the magnetic dipole transition rate and is suggested by identifying the nonrelativistic decay amplitude with the Lorentz invariant transition amplitude in the rest frame (see Appendix A).

In the context of the naive quark model, the quark charges, e_q , are known while the effective masses, m_q , are less well understood. The naive quark model analysis of baryon magnetic moments in terms of constitutent quark moments suggests the values $m_q \approx m_d \approx 330~MeV$ and $m_e \approx 510~MeV$: the breaking of SU(6) symmetry amongst baryon magnetic moments appears to be accounted for in part by the large mass of the strange quark. Precise measurements of vector meson radiative widths, in particular of the radiative widths of strange vector mesons, provide an opportunity to test this hypothesis and to test the validity of the naive quark model.

A new measurement of the K° (890) radiative width, $\Gamma(K^{\circ}$ (890) $\to K^{\circ} + \gamma$), is reported here. The result is significantly more precise than the only previously reported value⁴ and complements, in particular, the result of a recent measurement of the radiative width of the K^{+} (890).⁵ In the ratio of the radiative width of the K° to the radiative width of the K^{+} , phase space and spatial wavefunction overlap factors are expected to cancel. In the naive quark model, this ratio may be expressed in terms of quark moments alone:

$$\frac{\Gamma(K^{\circ} \to K^{\circ} + \gamma)}{\Gamma(K^{+} \to K^{+} + \gamma)} = \left[\frac{\mu_{s} + \mu_{d}}{\mu_{s} + \mu_{u}}\right]^{2} \tag{1.4}$$

In the SU(6) symmetry limit in which each quark moment is expected to be proportional to its electric charge with a common scale factor, this ratio is 4, while if quark moments are deduced according to the naive quark model from measured baryon magnetic moments, a value 1.64 is predicted.

Our measurement takes advantage of the Primakoff effect: the radiative width is determined from the cross section for the production of the K° (890) in a reaction of the form $K^{\circ}+A\rightarrow K^{\circ}$ (890)+A where A is a heavy nucleus. At high energy, this reaction takes place predominantly through the interaction of the K° with the electromagnetic field of the nucleus and the cross section for this electromagnetic excitation process is related by detailed balance to the radiative width in a well known way. In the next chapter, we describe the Primakoff effect and the relation between the radiative width and the production cross section. In succeeding chapters, the experiment and the data analysis are detailed. The implications of our result for $\Gamma(K^{\circ}$ (890) $\rightarrow K^{\circ}+\gamma)$ are discussed in the concluding chapter. We have also searched for the production of the K° (1430). Our upper limit for the radiative width of the K° (1430) and its theoretical interpretation are discussed in an appendix.

CHAPTER II

PRINCIPLE OF THE MEASUREMENT

A. Introduction

Direct observation of the decay $K^{o} \rightarrow K^{o} + \gamma$ is difficult because the radiative branching ratio is small ($\approx .2$ %). The inverse reaction $K^{\circ}+\gamma \rightarrow K^{\circ}$ provides an alternative method to determine the radiative width. This reaction may be observed with a Ko beam and a virtual photon target in the form of the electromagnetic field of a nucleus. In general, the cross section for the excitation of a stable particle, a, to any excited state, a', by single photon exchange with a nucleus, A, (Figure 1) is proportional to the radiative width $\Gamma(a \rightarrow a \gamma)$. This excitation mechanism is referred to as Coulomb production, and also as the Primakoff effect. The essence of our experiment was a measurement of the cross section for Coulomb production of K^{o} (890) mesons with a high energy, broad band K_L beam incident upon copper and lead targets with K^{o} meson production identified via the observation of the strong decay mode $K^{o} \longrightarrow K^{o} \pi^{o}$. The radiative width of the K° (890) determines the magnitude of the production cross section and was readily extracted.

In this chapter, Coulomb production will be discussed in some detail. Strong production backgrounds to the Coulomb production of vector mesons are relatively

small at high energy. We will describe what is known about these backgrounds and how they may be distinguished from Coulomb production in the extraction of the radiative width. The formalism presented below has been discussed many times. We therefore only point out the features that are important to our measurement and refer the reader to the literature for derivations and elaboration of the formulae.

B. Production of Mesons in the Electromagnetic Field of a Nucleus

At high energy and for small production angles, the differential cross section for Coulomb production of a narrow state a may be expressed as a function of the square of the four momentum transferred to the nucleus in the form

$$\frac{d\sigma}{dt} (a+A \to a^{\bullet} + A) = \pi \alpha Z^{2} \left[\frac{2S_{a^{\bullet}} + 1}{2S_{a} + 1} \right] \frac{\Gamma(a^{\bullet} \to a + \gamma)}{k^{3}} \frac{t'}{t^{2}} |f_{C}|^{2} \equiv |F_{C}(t)|^{2} \quad (2.1)$$

Here, α is the fine structure constant, Z is the atomic number of the target nucleus, S_a and S_a are the spins of a and a', $k=(m_a^2-m_a^2)/2m_a$ is the rest frame decay momentum in the transition $a'\to a+\gamma$, $\Gamma(a'\to a+\gamma)$ is the radiative width, and t is defined as the magnitude of the square of the momentum transfer q by

$$t = |q^2| = |(a-a^*)^2| = |(A^* - A)^2|$$
 (2.2)

where the particle name denotes the corresponding 4-momentum vector. The related variable t' is defined to be t minus it's minimum value, $t' \equiv t - t_{\min}$. The minimum momentum transfer is dictated by the mass change in the production process and at high energy is given by $t_{\min} = (m_a^2 - m_a^2)/2P_a$ where P_a is the labora-

Figure 1. Single photon exchange diagram describing the transition $a \rightarrow a'$ induced by the electromagnetic field of a nucleus A.

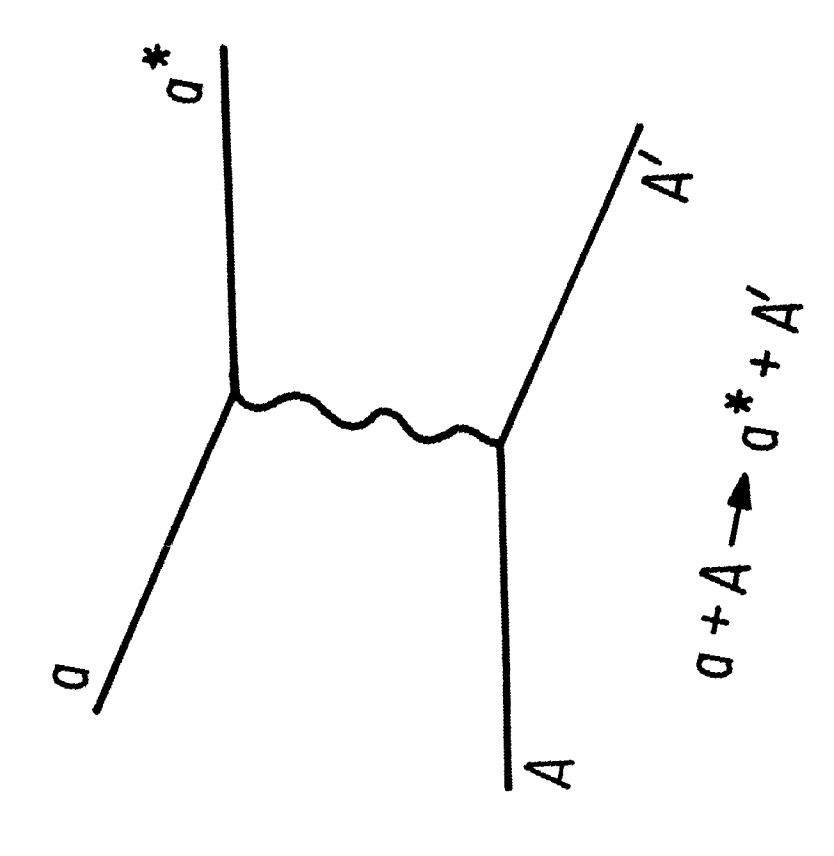
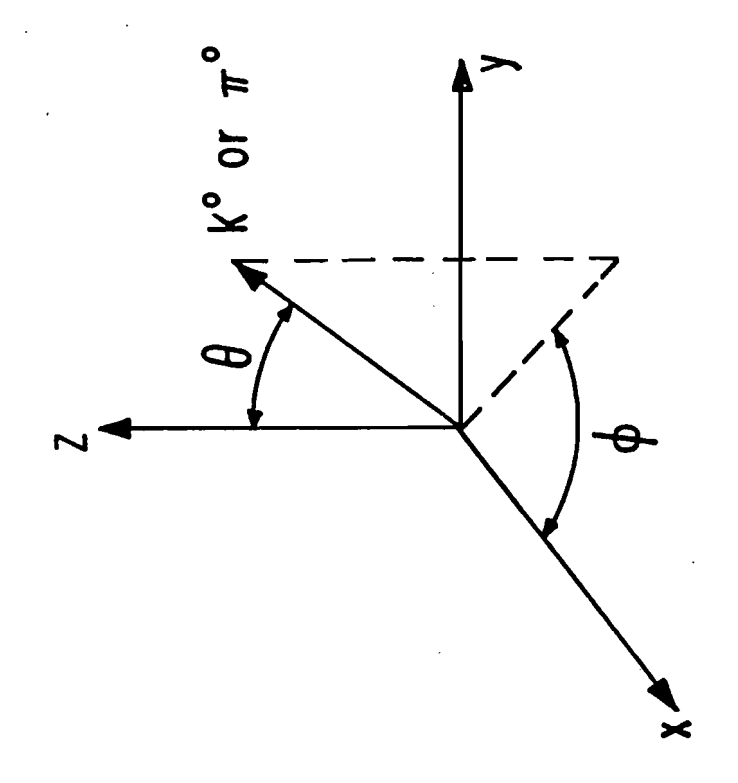


Figure 2. Production and decay of the K^0 (890) in the Gottfried-Jackson frame.



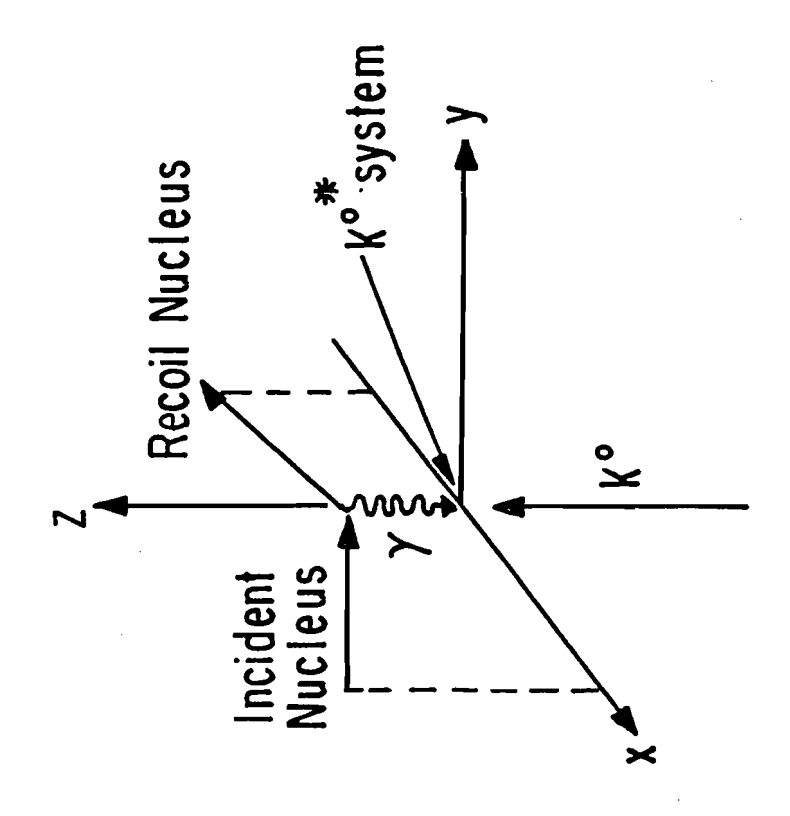


Figure 3. Diagrams and amplitudes describing the Coulomb production and strong decay of the K^{o*} and \overline{K}^{o*} . The production amplitudes have opposite sign.

 $< K^{\circ} \pi^{\circ} | K^* > < K^* | K^{\circ} \gamma > =$ $- \langle \overline{\mathsf{K}^{\mathsf{o}}} \, \pi^{\mathsf{o}} | \overline{\mathsf{K}^{\mathsf{*}}} \rangle \langle \overline{\mathsf{K}^{\mathsf{*}}} | \overline{\mathsf{K}^{\mathsf{o}}} \gamma \rangle$ $K_1 A \longrightarrow K^* A' \longrightarrow (K_S \pi^\circ) A'$

tory momentum of the beam particle a. The electric form factor of the nucleus, f_C , when modified to account for absorption effects, has the approximate form $\int_C e^{-R^2} f$ where R is the nuclear radius.

The form of the differential cross section is readily understood in the language of Feynman diagrams. The factor Γ/k^3 represents the coupling constant at the production vertex in the single photon exchange diagram. The factor αZ^2 is the square of the nuclear charge which is the coupling constant at the target vertex. The photon propagator contributes a factor $1/t^2$. Parity and angular momentum conservation require that the cross section vanish in the exact forward direction $(t=t_{\min})$. The nuclear form factor characterizes the charge distribution in the nucleus.

The most striking feature of Coulomb production at high energy is the production angular distribution. The photon propagator causes the production cross section to peak strongly at a small angle or equivalently at small momentum transfer. For production close to the forward direction, we may write $t=t_{\min}+|P_a\theta|^2$ where θ is the production angle in the laboratory of a' relative to the beam direction. The peak in the cross section occurs when $t=2t_{\min}$. For $K^a'(890)$ production at 150 GeV, $t_{\min}\approx 3\times 10^{-6}$ GeV² and the cross section peaks at production angle of 12 μ rad. In this region of momentum transfer, the nuclear form factor is approximately equal to unity: Coulomb production is a highly peripheral process and the production cross section is largely independant of the details

of the nuclear charge distribution. The energy transferred to the nucleus, given by $q_o \approx \vec{q}^2/2m_A$, is negligibly small: the nucleus recoils elastically in the production process.

Because we used a broad band K_L beam, the energy dependance of the Coulomb production cross section was important to our analysis. While the position of the peak in the production angular distribution decreases toward zero angle inversely with the square of the beam energy, the value of the production cross section at the peak increases. The total Coulomb production cross section is found to increase logarithmically with energy. This increase may be qualitatively understood if we notice that with higher available energy, the transverse momentum transfer required to satisfy the kinematic constraints decreases, and the more peripheral regions of the electromagnetic field may contribute to the production amplitude.

An additional characteristic of Coulomb production is the decay angular distribution of the produced particle. The production and decay of the particle a' are conveniently described in the Gottfried-Jackson frame which is the a' rest frame in which the z-axis is along the direction of the incident meson and the y-axis is normal to the production plane. The production and decay of the $K^{a'}$ are illustrated in Figure 2. In the Gottfried-Jackson frame, the z-component, m, of the spin of the K' is determined by the helicity of the photon. Parity conservation excludes the production of the m=0 state while the $m=\pm 1$ states are excited with equal amplitude. For a two-body decay to pseudoscalar mesons characterized by

spherical-polar angles θ and ϕ , angular momentum conservation requires that the decay products be in a relative P-wave which may be described by spherical harmonic functions. The decay angular distribution therefore has the form

$$\frac{dN}{d\Omega} = \frac{1}{2} |Y_{1,1} + Y_{1,-1}|^2 = \frac{3}{4\pi} \sin^2 \theta \sin^2 \phi$$
 (2.3)

This decay angular distribution is characteristic of single vector exchange in the production process, in this case the exchange of a photon.¹⁰

Finally it is important to note the consequence of a selection rule which is specific to our particular experiment. For an incident K_L meson, the neutral final state produced through the K' channel is exclusively $K_S \pi^o$, as opposed to $K_L \pi^o$. This selection rule results from the relative minus sign between the amplitudes for the production and decay of the K^{o^o} and \overline{K}^{o^o} , as illustrated in Figure 3, and applies to the exchange of any system of odd charge conjugation parity, in particular to single photon exchange.¹¹ Conversely, even charge conjugation exchanges do not contribute to the $K_S\pi^0$ channel.

C. Backgrounds resulting from strong production processes

Backgrounds to the production of vector mesons in the Coulomb field of a heavy nucleus arise from strong production mechanisms and constituted the principal source of uncertainty in first generation measurements of vector meson radiative widths. As has been discussed by Stodolsky¹², strong production close to the forward direction is enhanced by the coherent superposition of the production amplitudes from the individual nucleons in the nucleus. In general, single particle

exchange amplitudes which do not couple the production process to a change in the spin or isospin of the nucleons interfere constructively, while other exchange amplitudes interfere destructively. The exchange of isoscalar, natural parity $(P=(-)^J)$ mesons such as the ω consequently dominate peripheral strong production on heavy nuclei. (As was mentioned above, the exchange of even charge conjugation parity systems such as the pion are rigorously excluded from contributing to $K_S\pi^o$ elastic production.)

The differential cross section for peripheral strong production of vector mesons on various nuclei has been observed to have the form:

$$\frac{d\sigma}{dt}(a+A\to a'+A) = A^2 C_S t' |f_S|^2 \equiv |F_S(t)|^2$$
 (2.4)

where A is the mass number of the nucleus, C_S is a normalization constant, and f_S is a nuclear form factor. The strong production cross section is distinguished from the Coulomb production cross section by the t-dependance which results from the short range nature of the strong interaction: the propagator for the exchange of a heavy particle such as the ω reduces to a constant at small t so the factor $1/t^2$ which appears in the Coulomb production cross section does not arise. In the kinematic region in which the amplitudes overlap, interference may take place. We may express the total production cross section as:

$$\frac{d\sigma}{dt}(a+A\rightarrow a^*+A) = |F_C(t) + e^{i\phi} F_S(t)|^2 + \frac{d\sigma}{dt}_{inelastic}$$
 (2.5)

where ϕ is the relative phase between the Coulomb amplitude, F_C , and the strong amplitude, F_S , and we have allowed for a contribution from inelastic processes

which is expected to vary relatively slowly with t. The contribution of the Coulomb amplitude may be extracted by a fit to the measured differential cross section. The precise form of the amplitudes F_C and F_S will be specified below where we describe the application of this procedure to our data.

Regge theory would predict that $C_S \approx P_a^{2(\alpha_s-1)}$ for the exchange of the ω trajectory where $\alpha_o \approx .5$ is the trajectory intercept. The strong production cross section is expected to fall with a power law momentum dependance, $C_S \approx 1/P_a$. Although the precise power law is not well determined by existing data, it is to be expected that strong production contributes only a small part of the total K^{oo} production at energies of the order of 100 GeV or greater.

CHAPTER III

EXPERIMENTAL TECHNIQUE

A. General Considerations

A measurement of the Coulomb production cross section for the reaction $K^{o}+A\rightarrow K^{o}+A$ requires a K^{o} beam, a target, and an apparatus capable of identifying K^{o} production with well understood efficiency and good angular resolution. The measurement was made with two side-by-side K_L beams in the meson center beamline at the National Accelerator Laboratory. A copper target was placed in one beam and a lead target was placed in the adjacent beam. The decay products of K^{o*} mesons produced in these targets were observed with an apparatus downstream of this point. The use of copper and lead targets provided a test of the Z dependance of the Coulomb production cross section. The cross sections for the two targets were measured simultaneously. The beamline and apparatus had been designed to study the $\pi^+\pi^-$ and $\pi^o\pi^o$ decays of K_L and K_S mesons¹³ and with only minor modifications were nearly ideally suited to the measurement of the Coulomb production cross section through the observation of the decay $K^{\bullet} \rightarrow K_S \pi^0$. We chose to concentrate on the charged decay $K_S \rightarrow \pi^+\pi^-$. The charged particles were observed with a sequence of drift chambers. The positions and energies of the photons resulting from the decay of the π^0 were measured with a lead glass electromagnetic calorimeter. The drift chambers and the lead glass will be described below. The flux normalization was naturally provided by observation of the $K_L \rightarrow \pi^+ \pi^- \pi^0$ decay mode which is similar in topology to and identical in particle content with the observed K^* decays. The normalization events were observed simultaneously with the signal events thereby minimizing systematic error in the flux determination.

In this chapter we describe the physical layout and operation of the experiment including descriptions of the beamline, apparatus, data aquisition hardware, trigger logic, and calibration procedures. Due to the limited geometrical acceptance of the apparatus, we relied upon a computer simulation of the experiment to determine the acceptance corrections neccessary to fix the normalization of the production cross section. This simulation will also be described.

B. Overview of the Beamline and Apparatus

The beam mesons were produced by 400 GeV protons incident on a 38 cm berylium target at 0 degrees. Typically 5×10^{12} protons were delivered to the target in each .9 second pulse with pulses separated by \approx 15 seconds. Magnets were used to sweep the charged secondary particles produced by the primary protons away from the direction of a neutral beam. A 7.6 cm lead filter followed by a sweeping magnet significantly reduced the photon intensity in the beam. An additional filter consisting of 25 cm of carbon and 145 cm of berylium was used to enhance the K_L /neutron ratio. This enhancement results from the preferential

absorption of neutrons with respect to kaons at high energy. Collimators were placed so as to produce two nearly parallel beams of rectangular cross section subtending a solid angle of 4.5×10^{-8} steradian/beam. The copper and lead targets were placed in the adjacent beams at a distance of 406 meters from the proton target. The beam profile at the target position as determined from reconstructed $K_L \rightarrow \pi^+ \pi^- \pi^0$ decays is shown in Figure 4. Due to pair conversion in the targets of the photons resulting from the decay of the π^0 , the observable Coulomb production rate in the targets saturates at a target thickness of ≈ 1 radiation length, and decreases with greater target thickness due to absorption of the incident beam. The target thickness (.635 cm) was chosen to approximately maximize the number of observed Coulomb production events. Near the maximum, the observable production rate is insensitive to the target length and has only a linear dependance on the pair conversion cross section which is known to high accuracy. The target parameters are given in Table 1.

A diagram of the apparatus appears in Figure 5. Downstream of the K^{\bullet} production targets, there was an evacuated decay region in which decays of K_S and K_L mesons were observed to take place. This region began with two adjacent, 1.6 mm thick, scintillation counters (RA) which were placed in the beams approximately 3.5 cm downstream of the K^{\bullet} production targets and which covered the illuminated area of the targets. These counters were used to veto inelastic interactions in which charged particles were produced in the targets. The decay region ended with a 66 element hodoscope which consisted of two planes (H,V) of adjacent 1.3

Figure 4. Beam profiles as determined from reconstructed $K\pi_3$ events. The result of a simulation are shown by the open circles.

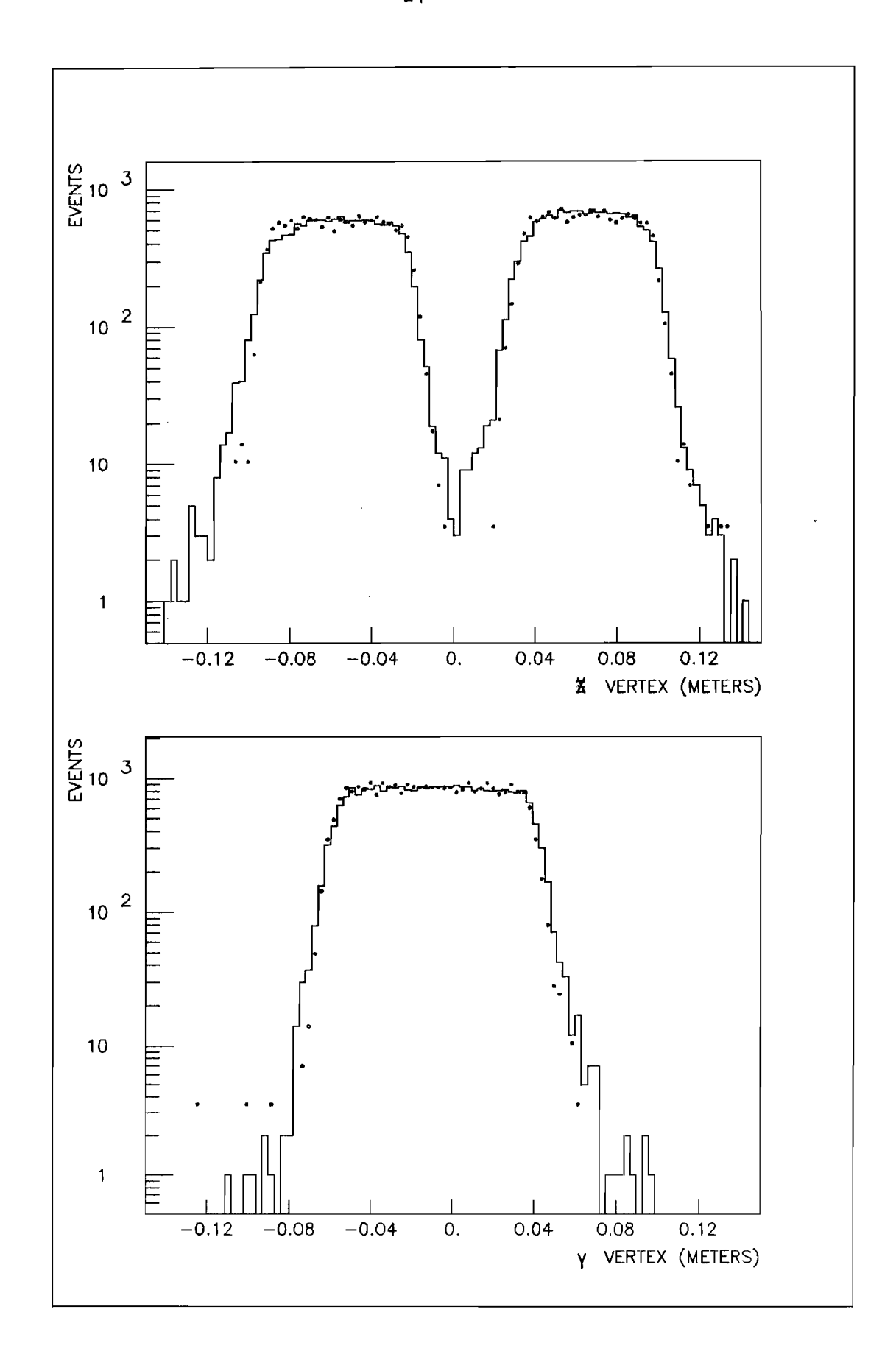


Figure 5. Schematic of the apparatus.

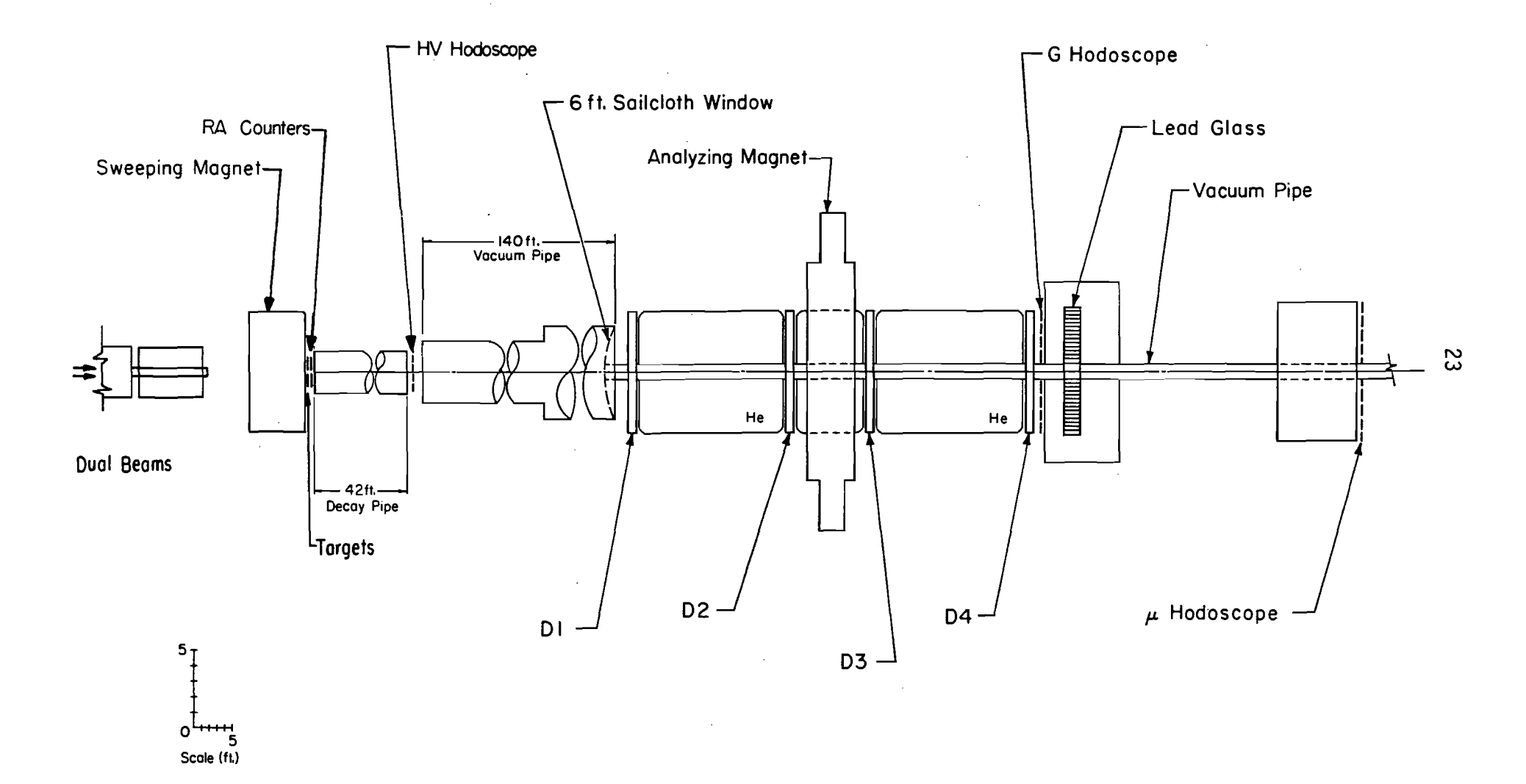


Figure 6. Front and side views of a drift chamber. Each chamber contained two planes of horizontal drift cells and two planes of vertical drift cells. Dimensions are in inches.

VERTICAL WIRES

WIRES

BEAM

FOIL LAYER

85.5

95.5

TABLE 1
PROPERTIES OF THE TARGETS

29	82
	02
63.54	207.19
.6396±.0016	.6421±.0033
10 cm × 15 cm	10 cm × 15 cm
8.894±.031	11.348±.063
	.6396±.0016 10 cm × 15 cm

TABLE 2
PROPERTIES OF THE DRIFT CHAMBER

Dimensions	1 m × 2 m	
Central box dimensions	18 cm × 30 cm	
Sense wire planes	2 (vertical) + 2 (horizontal)	
Sense wires/plane	104 (vertical),55 (horizontal)	
Maximum drift distance	2.286 cm	
Gas Mixture	Argon-Ethane (50% mixture)	
Gas Pressure	1 Atmosphere	
High Voltage	4.8 KeV	
Field Wires	Cu-Be	102 micron diameter
Sense Wires	Au plated W	25 micron diameter

TABLE 3
PROPERTIES OF THE LEAD GLASS

Array dimensions	122 cm × 227 cm × 60 cm
Block size	5.8 cm × 5.8 cm × 60 cm
Number of blocks	804
Glass type	Schott F2
Refractive index	1.6
Radiation length	3 cm

cm wide, scintillation counters filling an area of 28 cm × 56 cm. This hodoscope was used to trigger on charged particles exciting from the decay region. An evacuated pipe followed in which the secondary particles separated from one another. This volume was bounded by thin vacuum windows. A magnetic spectrometer was used to measure the momenta of the charged particles: four drift chambers (D1-D4) were used to pinpoint the positions of the charged particle trajectories while momentum analysis was provided by a rectangular aperature (2.5 m by 1 m) magnet which had an average \(\int Bdl \) of 212 MeV. Helium filled bags were placed between the drift chambers in an effort to minimize multiple Coulomb scattering. At the downstream end of the spectrometer was a 40 element hodoscope (G) used for triggering. The positions and energies of photons were measured with an 804 element rectangular array of rectangular lead glass blocks which was placed downstream of the G hodoscope. A 3 meter thick iron filter followed by a 13 element hodoscope (μ) provided for muon identification. A rectangular beam pipe passed through the center of the spectrometer and of the lead glass and allowed the beams to pass unobstructed to a beam dump. In addition, a number of scintillation counters (not shown) were positioned so as to veto events with particles outside the acceptance of the apparatus. These counters were each preceded with lead (1.9 cm) and were hence sensitive to photons.

A sketch of the drift chamber appears in Figure 6 and drift chamber parameters are given in Table 2. Each chamber included two planes of sense wires for each of two orthogonal directions. The two planes which measured each

coordinate were offset relative to one another to resolve the left-right ambiguity associated with a signal on any one sense wire. Many wires terminated on a central box through which the beam pipe passed. The box was supported stably by 16 twisted strand steel cables. In the drift chamber at the downstream end of the spectrometer, all horizontal wires were glued to a G10 strip which ran vertically down the center of the chamber. The wires were broken at this point and electronic readout was provided at both ends. These split wires and the box wires were useful in correlating the side and top views of track pairs. The vertical planes of the first and third chambers were equipped with mean time circuitry. 14 Each adjacent pair of sense wires was provided with a circuit which produced a signal in case both sense wires registered the passage of a charged particle through the drift chamber. The signal was produced at a time which was independent of where in the drift cell the particle passed. A linear analog sum of the mean time signals from all pairs of adjacent wires for each chamber provided a measure of the number of charged tracks which passed through the drift chamber at any given time.

Parameters describing the lead glass are listed in Table 3. The most important parameters are the longtudinal depth and the transverse block size. The 20 radiation length depth provided for near complete (\approx 97%) containment of electromagnetic showers which is important in obtaining good energy resolution. The transverse spread of a shower resulted in energy deposition in a "cluster" of lead glass blocks. The relatively small transverse block size was chosen to give acceptable shower position information on the basis of energy sharing. Efficient

Cherenkov light collection was ensured by total internal reflection from the highly polished block faces. These polished faces also allowed the array to be stacked with minimal space between adjacent blocks. Optical decoupling of adjacent blocks was achieved with a 13 micron aluminized mylar wrap. Careful temperature stabilization was necessary to prevent thermal stresses at the block faces to which the phototube assemblies were attached. The array was therefore housed in a light-tight temperature stabilized enclosure. Changes in the response of the array over time were monitored with a light flasher system. Light from a single triggerable high voltage spark gap was linked to each block through an optical fiber. Computer triggered calibration data was generated between and during beam pulses. Thus long and short term gain drifts as well as rate dependances could be studied.

C. Data Aquisition Hardware

We used a microprocessor based drift chamber electronic readout system developed at the University of Chicago for a different experiment. This system has been described elsewhere.¹⁵ In our application, a drift time digitization unit of 6.3 nanoseconds was chosen and corresponded to a drift distance of 315 microns. The microprocessors were responsible for scanning for valid data, subtracting a clock stop time from the encoded drift times, and sending this information to a buffer memory. Two microprocessors, each dedicated to the readout of two drift chambers, operated in parallel. An interface between the microprocessors and the

buffer memory coordinated the data transfer.

The lead glass readout was performed by a Lecroy 2285 ADC system. This system is based on a 12-bit linear analog to digital converter. With our choice of phototube gain, the .25 pCoulomb one count ADC sensitivity corresponded to a sensitivity of 17 MeV and the dynamic range extended up to 65 GeV. This ADC system possesses some novel features. First automatic pedestal subtraction is performed by a dedicated CAMAC processor which maintains pedestal data in an internal memory. This capability is essential to the second feature, namely the possibility of sparse readout. During data aquisition, the processor searches for valid pedestal subtracted data exceeding a variable preset threshold. Only those data above threshold and the data in some neighboring ADC channels are sent by the processor to the central computer and recorded. The number of neighbors to be read out is determined by a variable preset window parameter.

To take advantage of these features, the pedestals were sampled by the online data aquisition program between each beam spill. The average of five consequtive pedestals for each ADC channel was closely monitored by the online program. When significant pedestal drifts were detected, the pedestals stored in the ADC processor were updated. The size of the pedestal drifts determines a lower bound on the sensitivity threshold if the advantage of sparse readout is to be maintained. With considerable effort, short term pedestal drifts were reduced to of the order of 1 count and the threshold was set to 5 counts corresponding to an energy deposition of 83 MeV. The window parameter was set such that only the data in the

nearest neighbors of above threshold channels were recorded. This choice represented a compromise between energy resolution and data aquisition deadtime. As the window is increased, many more ADC data must be dealt with for each event. On the other hand, a small window results in the loss of the information in those ADC channels which are below readout threshold and also outside the window of any channel which does not exceed threshold. This loss of information resulted in an effective nonlinearity in the response of the lead glass detector, particularly at low energy. A correction for this effect will be described below.

The event trigger was used to open a 175 nanosecond gate during which time the ADC system was sensitive. The lead glass signals were delayed by coaxial cable to arrive within this gate. At the end of the gate, analog to digital conversion was initiated and the ADC data was available 220 microseconds after this point. ADC readout took place in parallel with the trigger initiated drift chamber readout with drift chamber data being assembled in a buffer memory. This phase of the data aquisition required approximately 1 msec per event. Following ADC readout, the buffer was examined for drift chamber data and a complete event record was assembled and passed to a queue to be written to magnetic tape. Under typical running conditions, we recorded 100 to 150 such event records during each beam pulse with a data aquisition associated deadtime of $\approx 17\%$.

Data was logged to magnetic tape at 1600 bytes per inch with a PDP-11 computer. The data aquisition software was based on the MULTI system which allowed for the easy introduction of online monitoring. The information actually written to magnetic tape for each event consisted in the latch bits associated with each scintillation counter in the experiment, the wire numbers and drift times associated with hits in the drift chamber, and the channel number and data of select ADC channels. In addition, we recorded diagnostic information such as the proton beam intensity monitor reading and the magnet current. Interspersed with event data records were data records containing light flasher and pedestal data used in the offline analysis of the lead glass behavior.

D. Data Sets and Triggers

The primary data set on which this analysis is based was collected during a two week period during the spring of 1982. The data collected specifically to study Coulomb production were supplemented by data collected to study neutral kaon decays and data collected for purposes of calibration and alignment. In this section, the running conditions which distinguished the data sets refered to in this analysis will be described.

The "K'" data set was obtained with the configuration of the apparatus as just described. The K' trigger was designed to accept $\pi^+\pi^-\pi^0$ events and, in order to minimize data aquisition deadtime, to discriminate against decay modes of the K_L other than the $K_L \rightarrow \pi^+\pi^-\pi^0$ ($K\pi_3$) mode. Rejection of the semi-leptonic and $3\pi^0$ decays was particularly important. The basic idea was to require that two and only two charged particles exit the decay region and that at least one photon enter the lead glass. The neutron flux in our "neutral meson beam" was another important

experimental consideration. The neutron to K_L ratio at the K' production targets was estimated to be 7:1. The RA anticounters placed just downstream of the K' production targets were used to reduce the sensitivity of the apparatus to neutron interactions in the targets. As a consequence of placing these counters in veto in the trigger, the charged decay modes $K' \rightarrow K' \pi^-, K' \pi^+$ were not observed. The apparatus was sensitive only to the neutral decay $K' \rightarrow K_S \pi^0$.

The K' trigger consisted of the following. The RA counters were put in veto to suppress events due to inelastic interactions in the targets. The HV hodoscope was used to require that charged particles be exiting the decay region. The precise requirement was that there be a hit in at least one counter in both the horizontal and vertical directions and that no more than two horizontal counters have hits. In addition, no horizontal counter was allowed to have a signal exceeding 10 times the minimum ionization level. Such a signal would have corresponded to a nuclear interaction in the scintillator. We required in addition that two and only two charged particles be accepted by the spectrometer. The mean time signals were used to require at least two hits with good mean time in the first or the third of the drift chambers where the drift chamber numbering scheme begins at the upstream end of the spectrometer. Two well separated hits in the G hodoscope at the downstream end of the spectrometer were required. The G hodoscope was sectioned into six nonoverlapping pieces as illustrated in Figure 7. Hits in at least two of these sections were required and an event was vetoed if more than two individual G counters were hit.

In order to suppress the abundant semileptonic decays of the K_L , one photon was required in addition to the two charged particles. The photon trigger was formed as follows. The lead glass signals were sampled by fast linear adders developed at the University of Chicago. These adders were configured to sum the sample signals from contiguous groups of nine blocks. These sums were further concatenated using LRS Model 428 linear adders to produce signals proportional to the total energy deposition in the six regions of the glass as illustrated in Figure 8. These signals were discriminated with a threshold corresponding to approximately 1.8 GeV. We required at least one such shower signal and, in addition, demanded that no charged particle had entered the corresponding region of the glass. The latter requirement was achieved with the G hodoscope which was divided into regions which overlapped as much as possible the sections of the glass. These regions differed only slightly from those described earlier. The outer edges of the lead glass were not covered by the G hodoscope but this did not present a serious problem as the charged particles were concentrated near the beam. Events in which a photon entered the inner most ring of glass blocks were vetoed by an anticounter array in the form of a collar around the beam pipe positioned just upstream of the glass and preceded by lead. The pattern of energy deposition in the lead glass for a typical $\pi^+\pi^-\pi^0$ event is shown in Figure 9.

We shall also refer in what follows to the "charged mode" data set which was accumulated to study the charged decays of the K_L and K_S mesons, in particular the $\pi^+\pi^ (K\pi_2)$ decay mode. The semileptonic decays, $K_L \to \pi e \nu$ (Ke_3) and $K_L \to \pi \mu \nu$

 $(K\mu_3)$, and $K\pi_3$ decays were also accepted. During this data collection period, the two K^* targets were removed. A one meter thick carbon regenerator was placed in one beam while the other beam was left empty. The data comprised principally charged decays of K_L mesons originating in the empty beam and charged decays of regenerated K_S mesons originating downstream of the regenerator. For purposes of this analysis, this data was used to check our understanding of the operation of and acceptance of the apparatus. The data was also important to the cross section normalization as will be made clear below.

The charged trigger was designed to accept all events in which two charged particles were produced by a decay in the decay region and accepted by the spectrometer. The HV requirement was identical to that used in the K^* trigger. The requirement at the G hodoscope was that two and only two G counters be hit with one of the hits in the upper half of the hodoscope and the other hit in the lower half. The up/down requirement favored the $K\pi_2$ decay mode which was of special interest and which produced charged particles symmetrically placed with respect to the beam. The mean time and veto counter requirements were similar to those used in the K^* trigger.

"Muon" data was collected at various times throughout the other data taking to determine the alignment of the apparatus. This data was taken with the two beams plugged with iron upstream of the apparatus and with the analyzing magnet not excited. The trigger was designed to accept only single penetrating muons, and to maximize the muon illumination of the apparatus. The muon trigger required

Figure 7. G hodoscope segmentation used in the K^{\bullet} trigger. In the upper figure, the individual counters are shown inside a box representing the external dimensions of the lead glass. Two of the six hodoscope regions are shown in the lower figure. The others may be obtained by reflections about the horizontal and vertical directions.

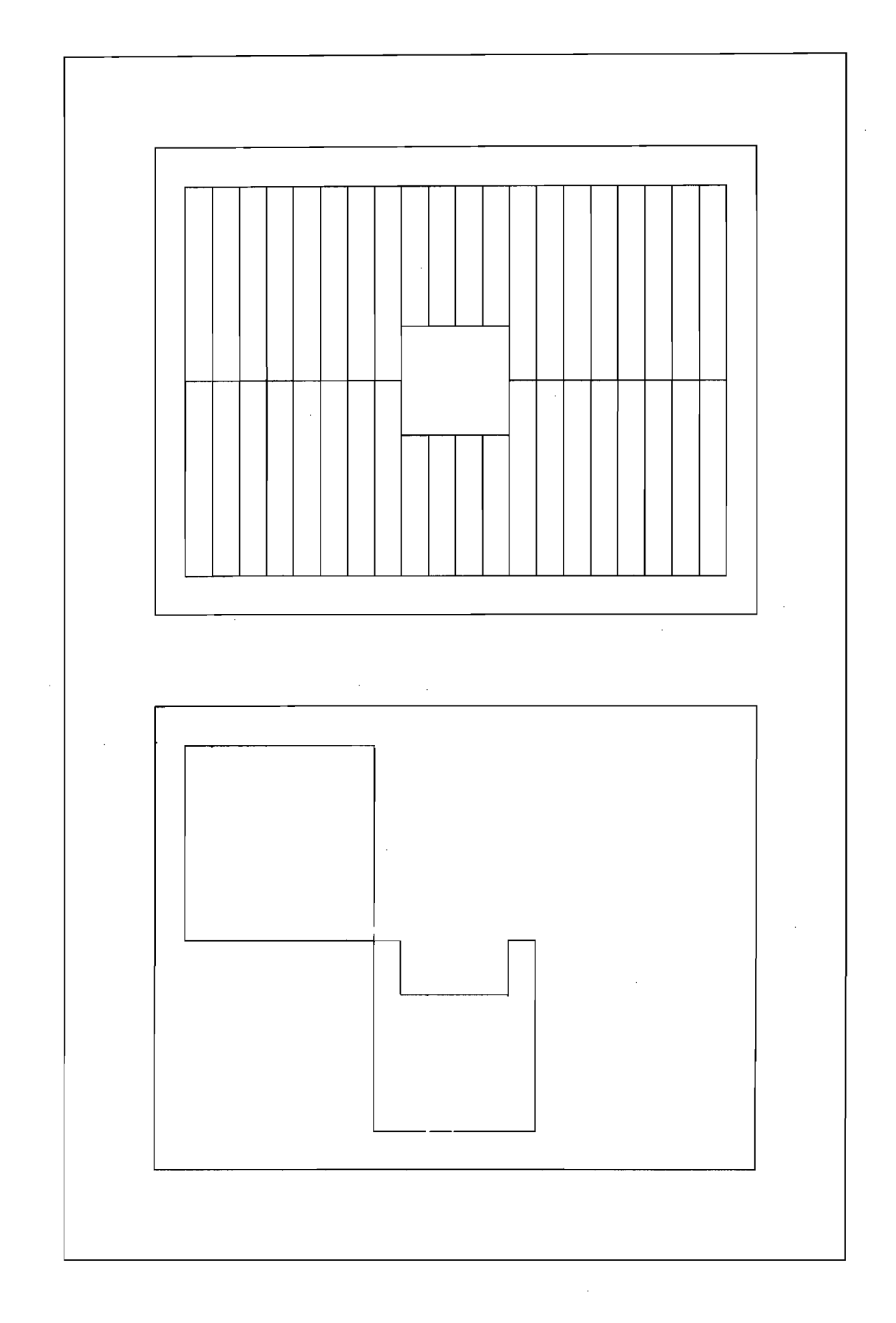
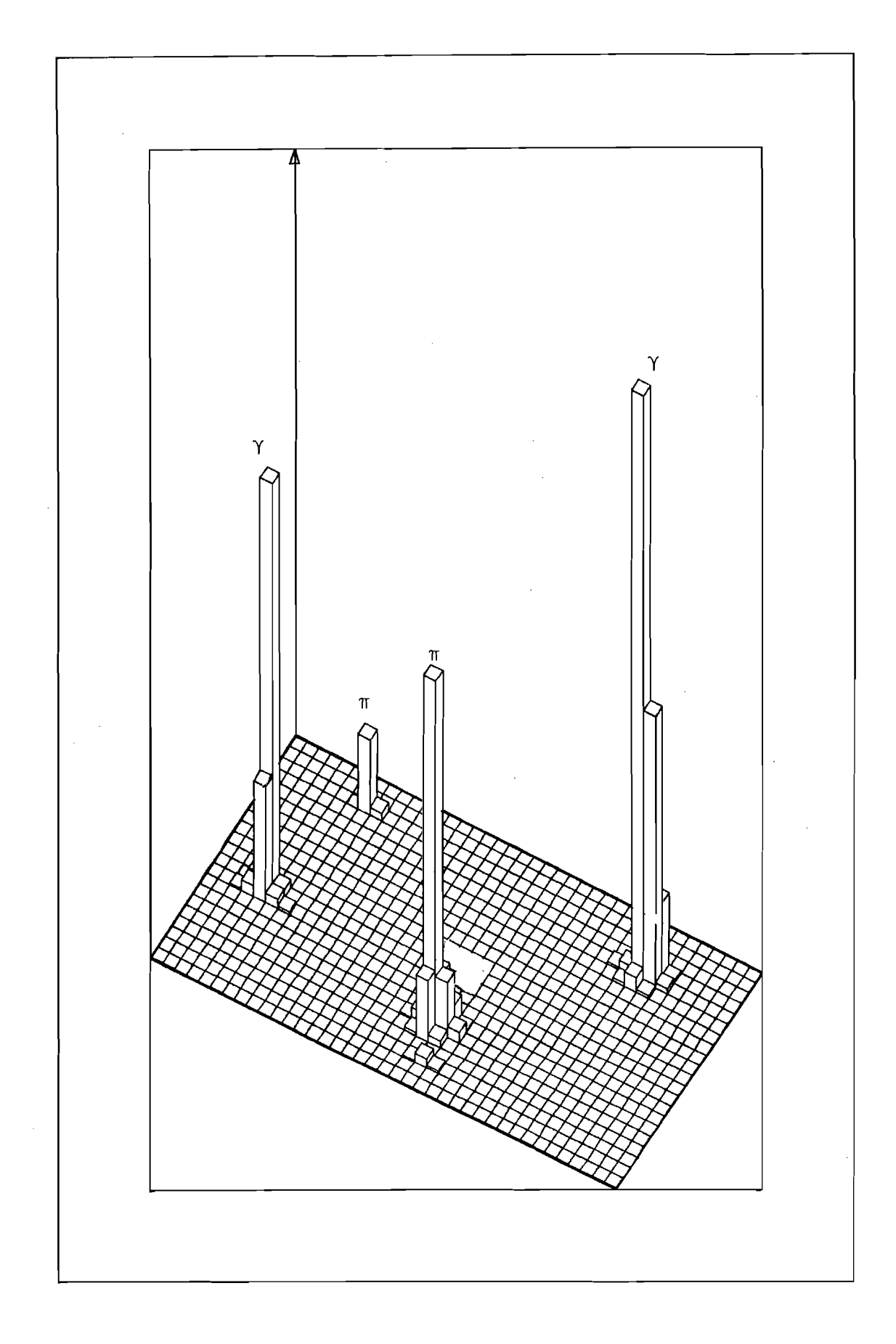


Figure 8. Lead glass segmentation used in the K^{\bullet} trigger. In the upper figure, groups of nine blocks are shown. Three upper and three lower glass regions are shown in the lower figure. The total energy in each region was used to identify photons in the K^{\bullet} trigger.

 			_					
	-							
			'	-		_		
				-				
						i k		
	 Т							
							_	

Figure 9. Typical pattern of energy deposition in the lead glass for a $\pi^+\pi^-\pi^o$ event. The vertical scale is proportional to the energy deposit per block.



simply a coincidence between a hit in the μ hodoscope and a hit in one of the hodoscope planes upstream.

E. Alignment and Calibration of the Apparatus

A precise knowledge of the positions of the elements of the apparatus was required for event reconstruction. The position of each element of the apparatus along the beam direction was determined with a tape measure while the more critical transverse positions were determined with reconstructed tracks of charged particles. Particular use was made of "straight-through" single muon events obtained with the muon trigger. The angular orientation and transverse position of each of the chambers were determined by an iterative minimization of the residuals between drift chamber hits and fitted straight tracks. The transverse positions were determined to a precision of a approximately 30 micons and the angles were determined to a precision of .1 milliradian. The procedure required the drift time to drift distance relation, which is described below, and assumed the nominal wire positions. The chamber was designed so that the wires were positioned with respect to the frame with a precision of about 25 microns. A special concern was the position of the central box to which a great number of wires were attached. A simple study indicated that the box positions did not differ significantly from the design positions. This study involved a comparison of residuals to fitted tracks between tracks which encountered box wires and tracks which did not, as a function of the distance of the track from the box. This study indicated that the ends of the wires at the box were correctly positioned to within \approx 60 microns. A similar study of the split wires in the fourth chamber suggested some shift in the epoxy strip which supported the break in these wires. This offset appeared to be fairly small, in the worst case shifting a wire position at the split by 100 microns. A complete determination of box and split wire offsets was not attempted. Analysis of all available muon data revealed small changes in the drift chamber positions with time. These changes could be correlated with drift chamber maintainence. No such shifts occurred during the K^* data taking.

In determining the position of the lead glass, it was assumed that the individual block positions conformed to an ideal rectangular grid. In setting up the array, each row of blocks was positioned with optical surveying equipment. Great care was taken to ensure a minimum of space between adjacent blocks and to ensure that the block centers corresponded as closely as possible to the ideal grid. Prior to installation, the dimensions of all blocks were precisely measured and considered by a computer program which suggested an acceptable array. The root mean square deviation from the ideal grid expected on the basis of the program was 320 microns and careful stacking produced the desired positions within measurement error (≈ 12 microns). The position of the entire array with repect to the drift chambers was determined to a precision of \approx 100 microns by correlating the projections of electron tracks to the lead glass with the centroids of the associated showers. The shower positions were determined from energy sharing as will be described below.

Drift chamber calibration involved the determination of the relation between the measured drift time and the corresponding distance of drift from the sense wire. The time-to-distance relation may be determined the integral of the distribution of drift times for straight tracks, shown in Figure 10, and was well described analytically as a linear relation with small cubic corrections at the edge of the drift cell closest to the field wires. The actual relation used in the data analysis was determined by a minimization of the residuals to fitted tracks at various times during the data taking. This procedure is described in reference 14. The effective chamber averaged spatial resolution was estimated from residuals to fitted tracks as σ =250 micron/ wire. The average drift chamber efficiency was 97% with small chamber to chamber deviations. An expected loss of efficiency in the innermost and outermost drift cells due to degradation of the electrostatic fields was observed. Particles which entered these regions were excluded from the data analysis by fiducial volume cuts.

An accurate field map of the analyzing magnet was made during a previous experiment. The variation of the \int B dl was measured with a precision of .2%. We redetermined the absolute field value for our magnet current by requiring that the reconstructed invariant mass of regenerated K_S mesons from the charged mode data coincide with the accepted world average. In addition, the integral horizontal field component was measured as a function of position over the magnet aperature by studying variations in the reconstructed K_S mass. For an average horizontal momentum kick of 212 MeV, the corresponding vertical kick varied from 0 to 4

MeV.

The decays $K_L \rightarrow \pi^{\pm} e^{\pm} \nu$ in the charged mode data set provided momentum analyzed electrons which were used to determine gain constants for each of the 804 lead glass blocks. We defined the variable E/P for reconstructed charged particles to be the ratio of the shower energy measured in the lead glass to the momentum as measured by the drift chamber spectrometer. In Figure 11, the distribution of this variable for a sample of particles from the charged mode data set is shown. Particles for which E/P was close to 1.0 were identified as electrons. Small values corresponded to particles which did not interact in the glass. In between values coresponded to hadronic showers in which only some fraction of the energy was visible. Values of E/P much greater than one resulted from shower overlap, in particular from electron bremstrahlung. Because the energy of an electromagnetic shower was shared among typically 9 blocks, an iterative approach to the gain determination was used. For each identified electron, the value of E/P was used to estimate the gain of the centermost block of the corresponding cluster and a gain adjustment for each block was determined from many events. This procedure converged in three iterations.

In Figure 12, the width and mean of the E/P distribution for electrons are shown as functions of momentum. Correcting for the small contribution to the width due to momentum resolution, the lead glass energy resolution could be represented by the form $\sigma_E/E=3\%+5\%/\sqrt{E}$ where E is in GeV. The second term has the form and magnitude expected for the contribution of photostatistics. The

Figure 10. Integral of the distribution of drift times for single muon events.

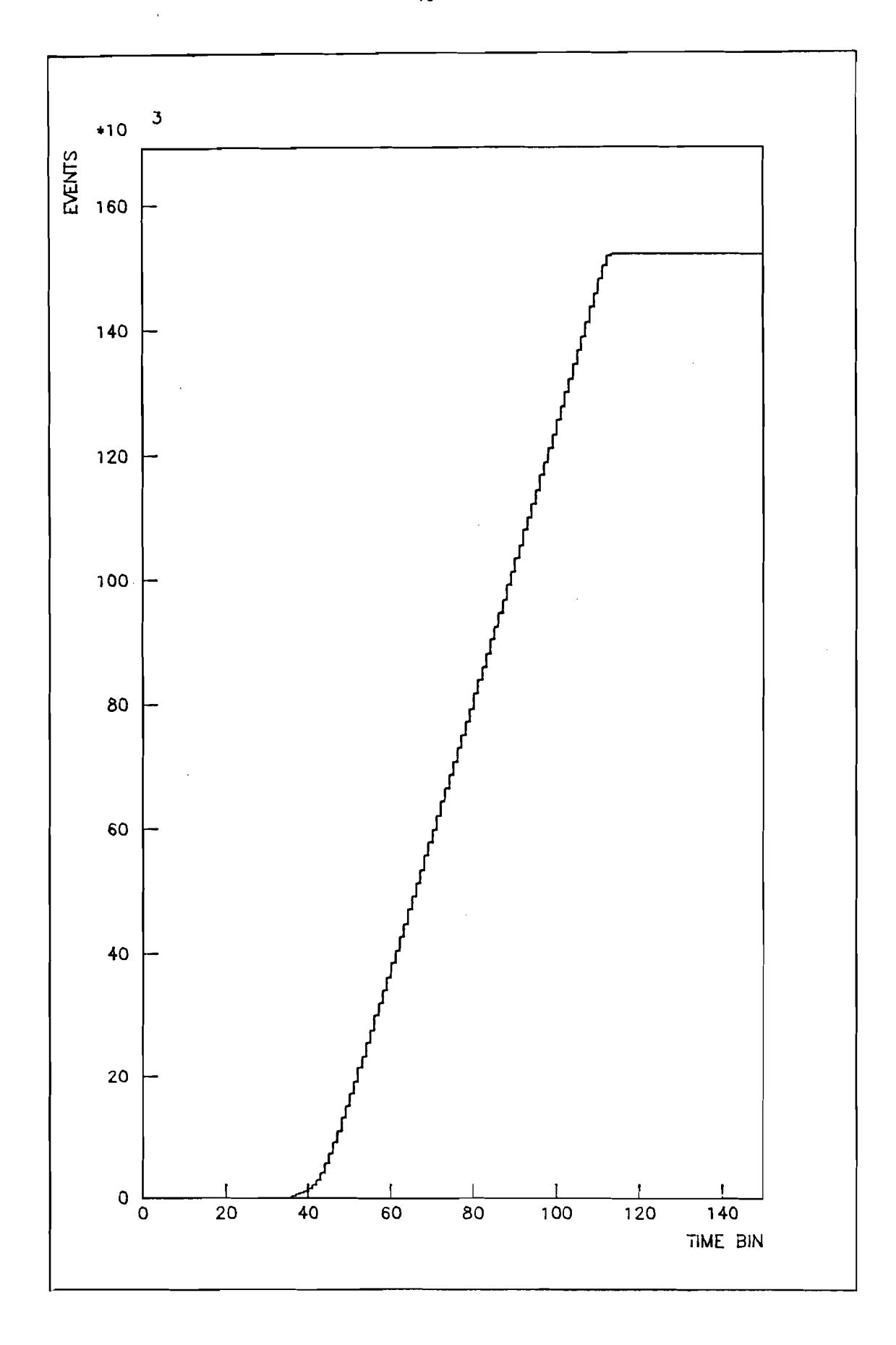
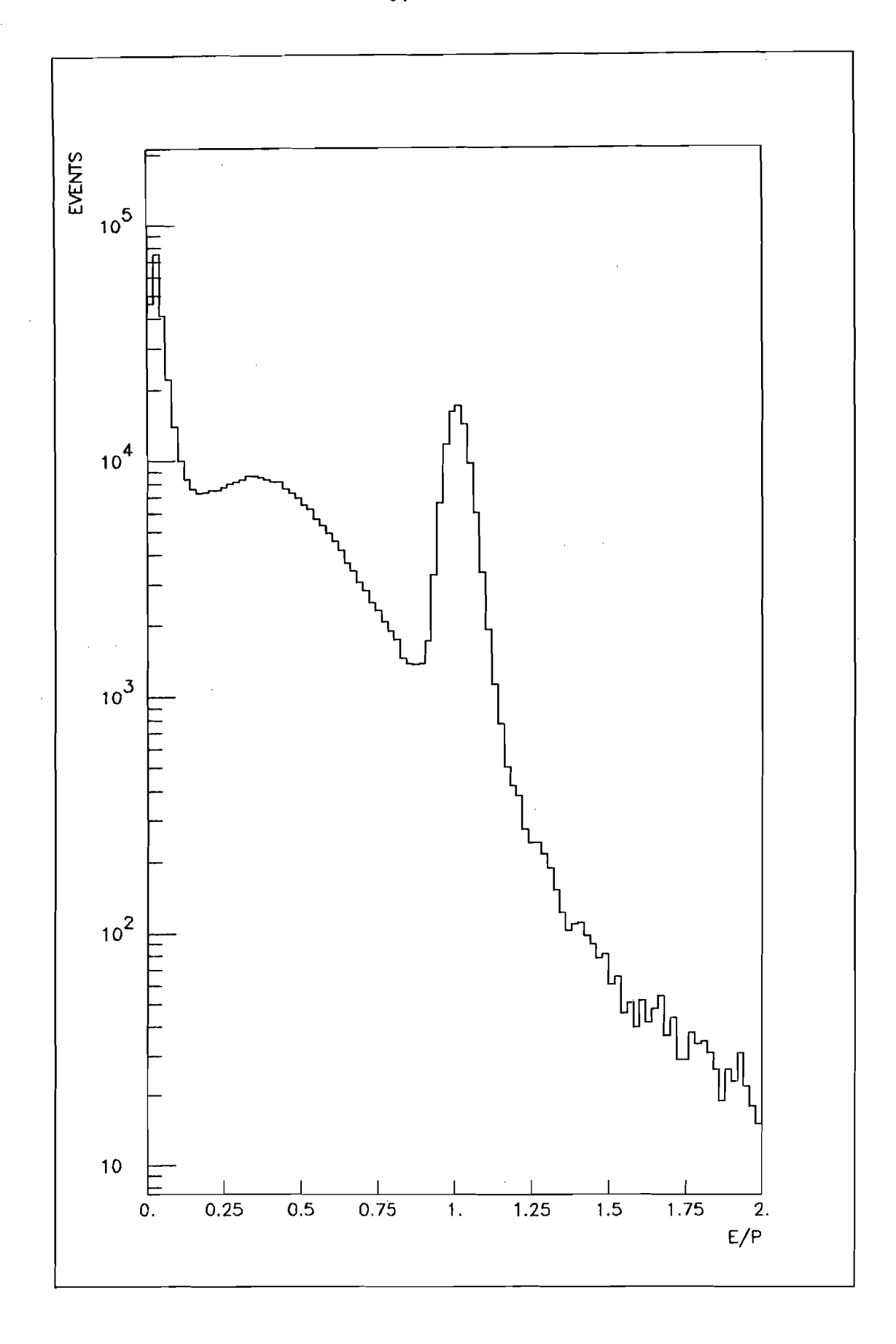


Figure 11. Distribution of the ratio (E/P) of the energy deposited in the lead glass to the momentum measured in the drift chambers for a sample of tracks from the charged mode data.



constant term represents the statistical error in the gain determination as well as systematic effects.

Nonlinearity in the lead glass response was reflected in the observed energy dependance of the mean of E/P (Figure 12b). The decrease in the ratio at low energy was attributed to the sparse readout of the lead glass by the data aquisition system. The energy loss due to sparse readout was in fact a sensitive function of the position at which a particle entered a block. A shower energy correction was therefore applied on a shower by shower basis. To determine the correction, we took advantage of the fact that the mean shower shape has only a weak energy dependance. Using just high energy showers in which many blocks were read out, the energy fraction deposited in each block was determined empirically as a function of the position of the shower center. For low energy showers, the shower center was found from the energy sharing using the available information, the energy fraction deposited in "missing" blocks (those that were not read out) was calculated, and a correction was applied.

The decrease in E/P at high energy was associated with ADC nonlinearity. Due to an oversight, during the charged mode running, the lead glass signals were incorrectly timed with respect to the ADC gate. As was found in laboratory tests, such mistimeing gives rise to nonlinearity. This timeing problem was rectified prior to the K' data taking so that nonlinearity of this origin was not expected during this period. For charged mode data, a simple energy dependant correction was applied to cluster energies which amounted to a fractional correction of .4%/GeV.

This correction was not applied to the K^* data.

The K' trigger excluded Ke_3 events so a different calibration method was required for this data set. The method was similar to the iterative electron method but was based on π_0 's. The gains were adjusted iteratively to reduce the width of the $\pi_0 \rightarrow \gamma \gamma$ mass distribution for identified $K_L \rightarrow \pi^+ \pi^- \pi^0$ events in which the π_0 origin was given by the reconstructed vertex of the two charged pions. The description of the event selection and reconstruction procedure is deferred to a later chapter. This method was limited primarily by statistics and it also converged in three iterations. The variation of the mean and width $\pi_0 \rightarrow \gamma \gamma$ mass peak for $K\pi_3$ events with the energy of the least energetic of the two photons is shown in Figure 13 and compared to the Monte Carlo prediction. The Monte Carlo prediction was based on the resolution obtained with the energy resolution for the two data sets was comparable.

Changes in the response of the lead glass array with time were monitored with the light flasher system. It was found that over the two week K' data taking period, the root mean square change in gain of the 804 blocks relative to the mean gain was .8 %. This number resulted from a comparison of the relative gains as determined by the flasher system at the beginning and end of the period. Although the flasher system was capable of tracking these small gain drifts, they made a negligible contribution to the overall resolution and were ignored. Similarly, small observed rate dependances were neglected.

Figure 12. Lead glass response to electrons. The variation with energy of a) the root mean square width and b) the mean of the E/P distribution for electrons is shown.

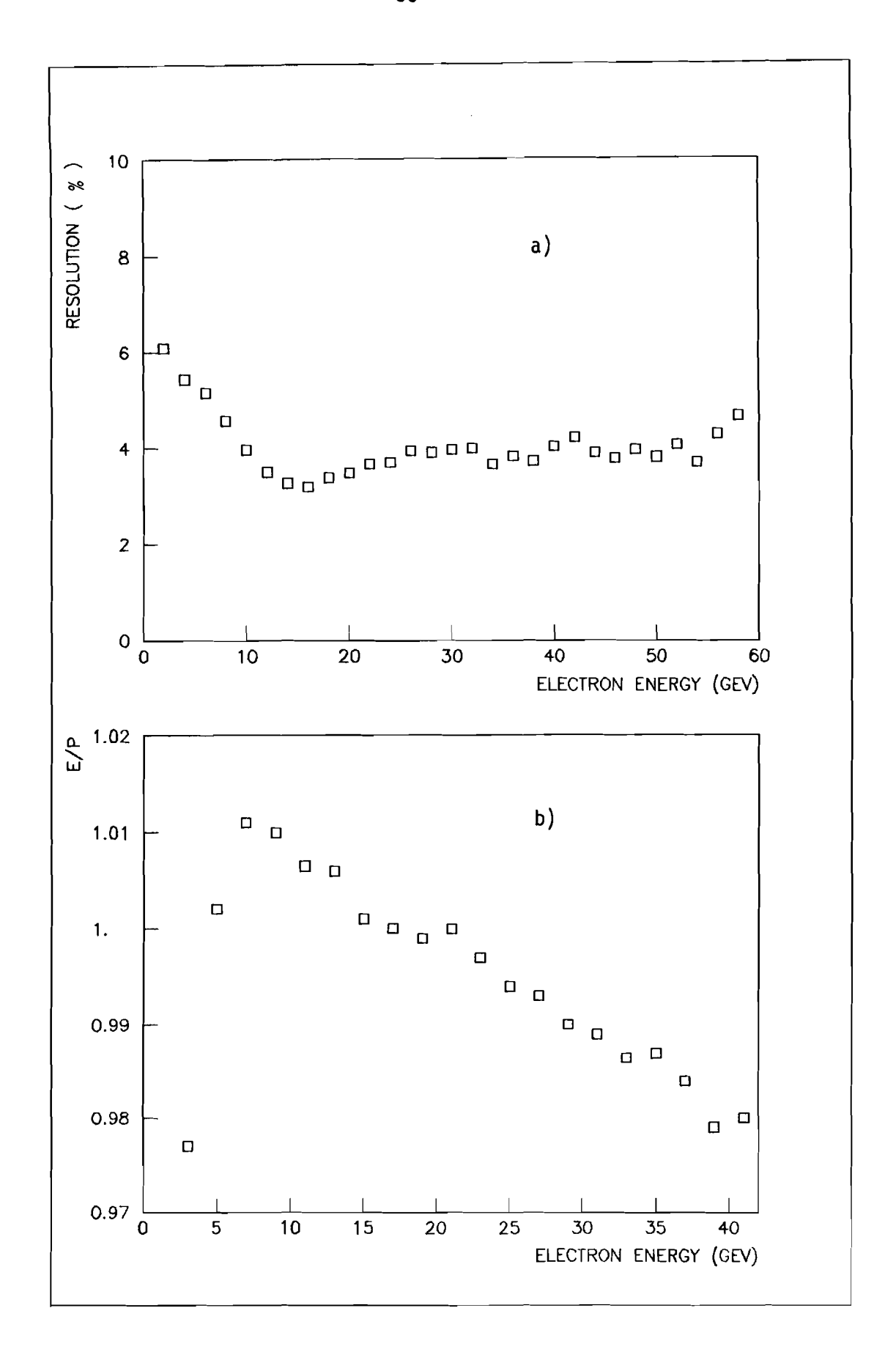


Figure 13. Variation of a) the mean and b) root-mean-square width of the π^0 mass with the least energetic of the two photons for identified $K\pi_3$ decays. The simulation assumes the resolution as measured with electrons.

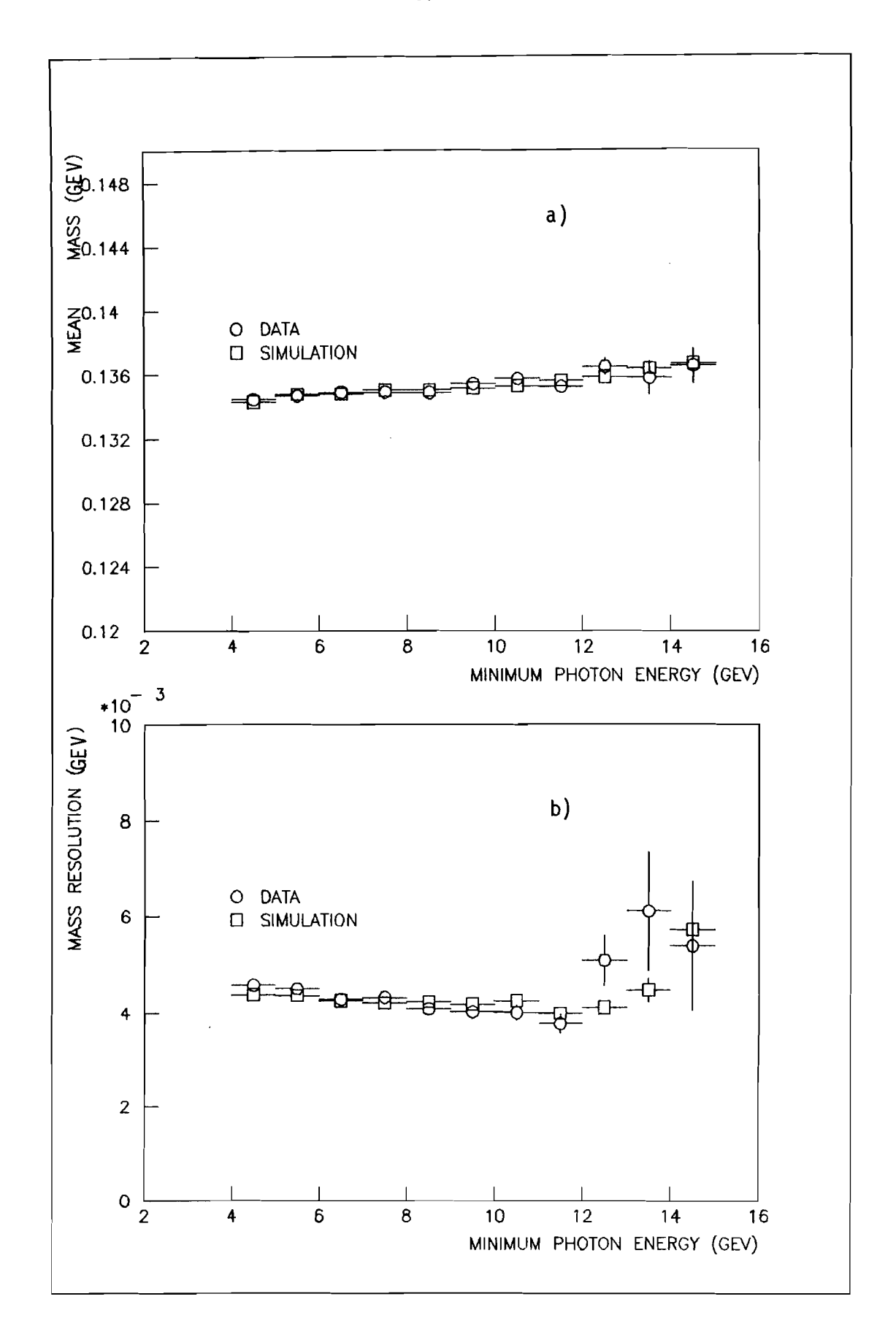
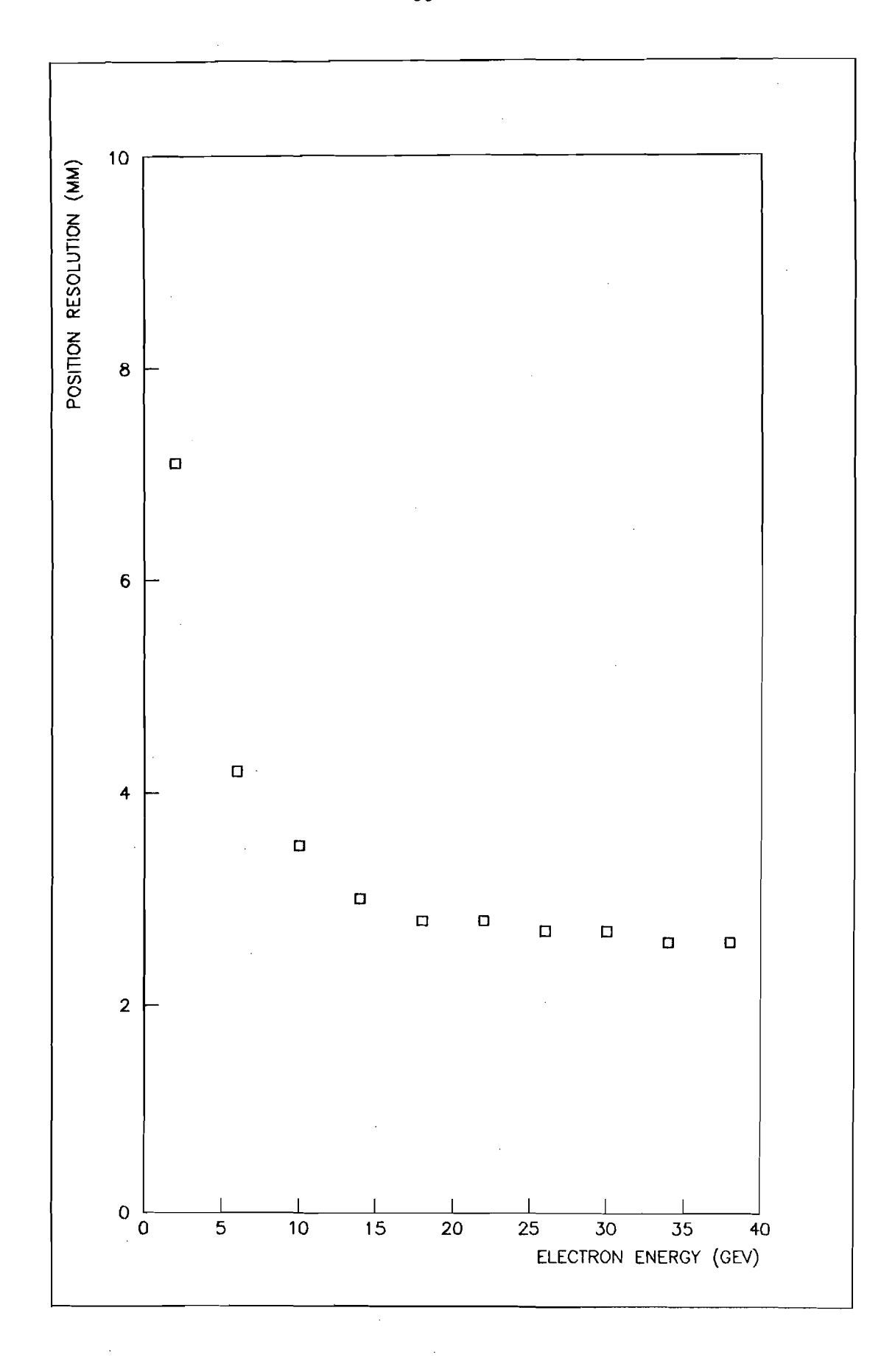


Figure 14. Energy dependance of the lead glass position resolution as deduced from electron initiated showers. The root mean square difference between the shower position as determined from the energy sharing and the electron track position projected from the drift chamber system is plotted as a function of the electron energy.



Photon positions in the lead glass were determined from the energy sharing between columns (and rows) of blocks. Using identified photon initiated showers and assuming that the photons were on average uniformly distributed over the face of the block, we determined the functional relation between photon position and the ratio of the two largest column energies from the integral of the distribution of the ratio, using the constraint that the value 1.0 correspond to a position coordinate at the block edge between two columns. No significant energy dependance to the position-ratio relation was found. The more complicated method of fitting a shape to the entire cluster was found to give a negligible improvement in the position resolution: blocks in the outer edges of a cluster contained a relatively small fraction of the energy and contributed little position information. Electrons were used to estimate the position resolution as is shown in Figure 14. The energy dependance of the position resolution has the approximate form $\sigma_z \approx 2.5 mm \sqrt{1.0 + 9.4/E}$ where the total energy E is in GeV. This form represents the resolution averaged over the block face.

F. Simulation of the Experiment

An analytic calculation of the acceptance of the apparatus for even the simplest event topology was prohibitively complicated. We therefore determined the acceptance by a standard Monte Carlo sampling technique in which the entire experiment was simulated on a computer. Comparisons of Monte Carlo simulated data to the real data also provided valuable checks on our understanding of the operation of the detector and aided the data analysis. Some important details of this simulation are presented in this section.

Simulations of K_L decay and K^* production and decay were performed for both the charged and K' triggers with account taken of the slight differences in the configurations of the apparatus and in the detector response. The simulation began at the position of the K^* production targets where K_L mesons were generated with a momentum spectrum as determined from the data (Chapter V). Coulomb production was simulated according the formulae of Chapter II. Particle decays were generated according to known physics. In particular, the three body decays of the K_L were generated using the world average values for the Dalitz plot parameters¹⁶. Interactions and decays of secondary and tertiary particles were simulated if necessary. In particular pion decay in flight was included. No attempt was made to follow converted photons. Events in which a conversion took place were expected to be vetoed by the trigger or lost during event reconstruction. Electron bremstrahlung was simulated by generating a single photon collinear with the electron at the analyzing magnet with the photon energy distributed as expected for the total bremstrahlung energy loss in the material up to that point. Multiple scattering was simulated as precisely as possible by applying the Moliere theory¹⁷ to each element of the periodic table contained in each component of the apparatus, including counters, vacuum windows, air spaces, drift chambers wires, the lead glass and the iron muon filter. The trajectories of charged particles were tracked through the analyzing magnet assuming a uniform magnetic field with the

\$\int Bdl\$ as determined from the field map and with the measured vertical momentum kick applied at the magnet center. No attempt was made to simulate the pattern of energy deposition in the individual lead glass blocks. The cluster position and energy resolution were simulated assuming Gaussian forms with the measured energy dependant root mean square widths. Similarly, no attempt was made to simulate the actual time distributions of hits in the drift chambers or any spatial variation in chamber efficiency. Rather, measured chamber averaged efficiencies and resolutions were applied to Monte Carlo data. Trigger counters were assumed to be completely efficient. A comparison of the counter illuminations for data and Monte Carlo showed that this was an excellent approximation.

The smeared Monte Carlo data was analyzed with the same computer programs (Chapter IV) as the real data with the following exceptions. Because no attempt was made to simulate energy deposition patterns in the lead glass, it was not necessay to run the cluster finding routine on the Monte Carlo data. Complete reconstruction efficiency was assured by requiring in the event selection a minimum energy deposition and ample cluster separation. Similarly it was not necessary to run the track finding routine on the Monte Carlo data. Rather, Monte Carlo events satisfying the loose requirements of the reconstruction program were selected. Complete reconstruction efficiency was then assumed.

Some general cuts were applied to the data to ensure the accuracy of the simulation. Data collected during periods when the operation of the apparatus was questionable were excluded. Reconstructed events were required to be well within

all aperatures. Also, events in the K' data set were required to satisfy a software equivalent of the hardware trigger. This eliminated the approximately 1% of all triggers in which a photon trigger was faked by leakage of hadronic shower energy from one glass section to another. An offline study of the trigger indicated that one group of nine blocks completely failed to supply photon triggers. This defect was associated with a failed linear adder circuit. The corresponding loss of reconstructable events was reduced by the fact that both photons were often capable of triggering the apparatus. A small number of Monte Carlo events was eliminated by including this trigger defect in the software trigger.

CHAPTER IV

DATA REDUCTION

A. Event Reconstruction and Event Selection

In this chapter we describe the procedures used to reconstruct $\pi^+\pi^-\pi^0$ events, the criteria used to select $K^e \to K_S \pi^0$ and $K_L \to \pi^+\pi^-\pi^0$ decays and the backgrounds to the selected event samples.

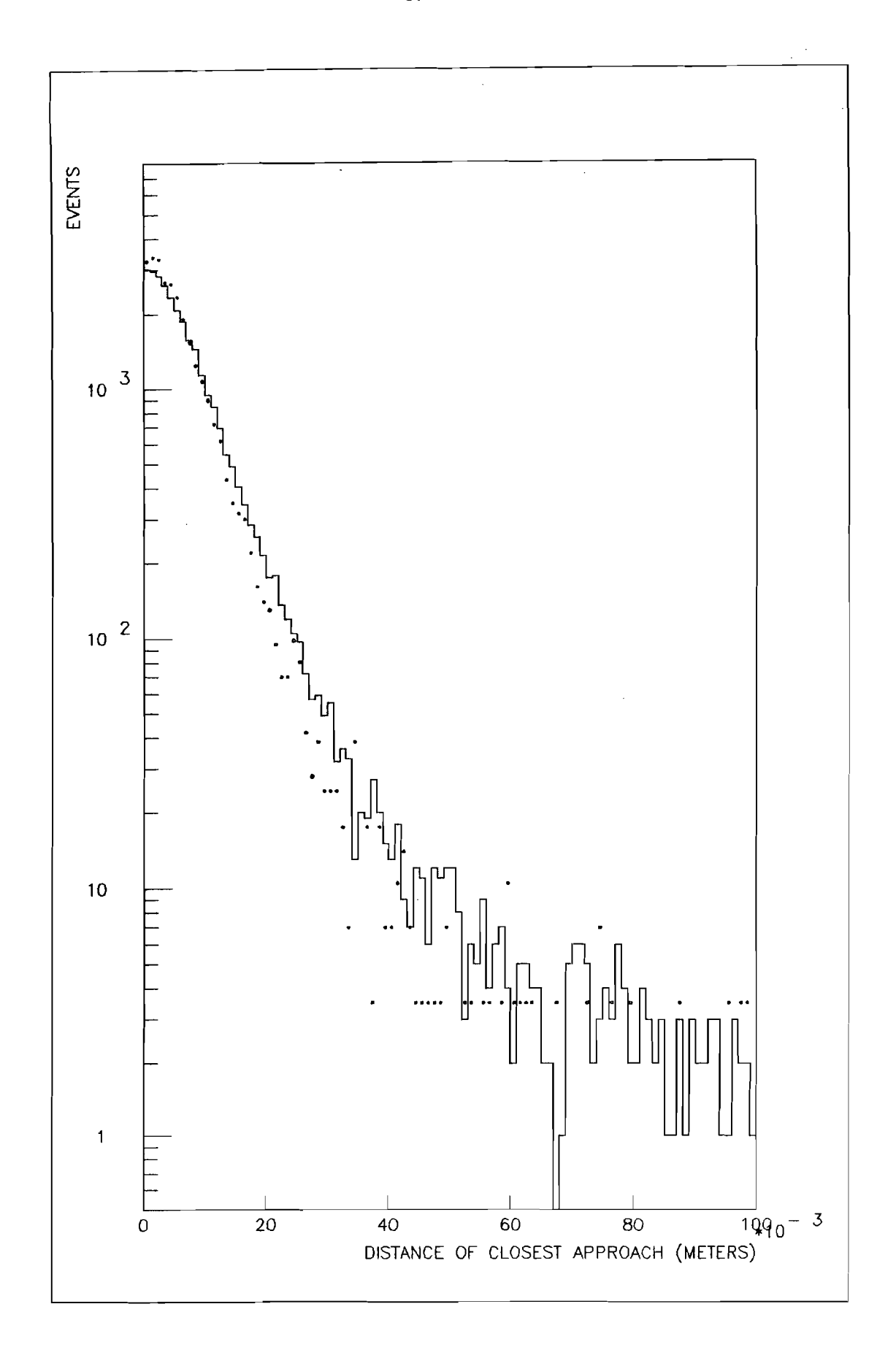
Event reconstruction involved the association of tracks with hits in the drift chambers, the identification of photon showers in the lead glass, and the reconstruction of the corresponding momentum vectors and event topology. The track finding algorithm searched for events with a pair of charged particles of opposite sign charge and considered all possible two track combinations of hits in the drift chambers satisfying a minimum number of hits requirement. In case of an inefficiency leading to a left right ambiguity, both possibilities were included. In the bend view, the downstream track segments were required to correlate to the two G counters that were hit with allowance made for multiple scattering and resolution and to roughly meet the upstream track segments in the center of the magnet. In addition, the track projections to the plane of the HV hodoscope were required to be contained roughly within the active area of the hodoscope. By these devices, even in the presence of accidental hits and inefficiencies, the number of

possible pairings was tremendously reduced. The best possible track pair was then selected based upon the number of hits and the χ^2 of the fit to the tracks. Approximately 40 % of the triggers contained same charge tracks, an unacceptable combination of inefficiencies, or a high multiplicity of out of time stale tracks and were not reconstructable. The track finding efficiency for reconstructable events was estimated by a handscan to be greater than 95% and was not expected to depend upon momentum or track position. It therefore affected K^* and $K\pi_3$ events equally and was not a concern in the normalization.

To determine the momentum of the charged particles, the drift chamber hits associated with a track were fit to a kinked line with the introduction of a pseudohit at the center of the analyzing magnet. In the least squares fit, a 400 micron resolution was associated with the pseudohit. The particle momentum was determined from the fitted bend angle according to the field map.

The vertex associated with a charged track pair was found by minimizing the distance between the extrapolations of the two upstream track segments. Because of multiple Coulomb scattering and drift chamber resolution, the two segments did not in general extrapolate exactly to a common point. Instead a line segment was found which connected the two points between which the distance between the two tracks was a minimum. The center of this line segment was taken as the reconstructed vertex. The length of the line (distance of closest approach) provided a measure of the goodness of the vertex reconstruction and was required to be less than 10 cm. In Figure 15, the distribution of the distance of closest approach for

Figure 15. Distribution of the distance of closest approach of tracks for $K\pi_3$ decays. The Monte Carlo prediction is superposed.



 $K\pi_3$ events is compared to the prediction of the Monte Carlo. A slight discrepancy was observed and was ascribed to incomplete understanding of the drift chamber alignment.

Cluster finding in the lead glass involved a simple peak search algorithm that required a minimum cluster energy of 200 MeV. Clusters not associated with charged tracks were considered as possible photon candidates and were chosen so as to minimize the bias in the selected event sample. A minimum photon energy requirement of 3 GeV ensured that both photons from a π^{o} decay were above the K' photon trigger threshold. In addition, candidate photon clusters were required to be well within the volume of the detector and well separated from each other and from the clusters associated with the two charged tracks. Because hadronic showers are typically broader than electromagnetic showers, and exhibit large fluctuations in shape, the overlap problem was studied in detail, using actual identified clusters. In order to reduce the overlap induced energy resolution to 1%, a minimum photon- hadron separation of 23 cm was required. This requirement also ensured that the calculated photon positions were unaffected by overlap. Events for which the $\pi^+\pi^-$ invariant mass was less than 380 MeV were identified as $K_L \!\!\to\! \pi^+ \pi^- \pi^0$ decays and the origin of the π^o was assumed to be at the reconstructed vertex. (The kinematic maximum $\pi^+\pi^-$ invariant mass for a $K_L \rightarrow \pi^+\pi^-\pi^0$ decay is 363 MeV.) Otherwise, the event was assumed to have originated in the K' production target and the $\pi^+\pi^-$ momentum vector was extrapolated to the target and the π^0 was assumed to have originated at this point. The invariant mass of a photon pair could then be calculated based upon the positions and energies in the lead glass. We considered only fully reconstructable events so at least two photon candidates were required. In case of an accidental photon candidate (3.9% probability), the pair of photon candidates which gave the best π^0 mass was selected. The 2γ mass was then required to be within 15 MeV of the accepted π^0 mass. Transverse momenta were calculated with respect to a line drawn from the proton target to a point in the K' production target. For K' decays, this point was the π^0 origin defined above. For $K_L \rightarrow \pi^+\pi^-\pi^0$ decays, this point was determined by extrapolating the 3-momentum vector of all three pions through the vertex to the K' target.

In Figure 16a, the distribution of the $\pi^+\pi^-$ mass for a partial sample of such reconstructed events is shown. The two features in the charged mass distribution resulted from $K\pi_2$ and $K\pi_3$ decays. One observes that candidates for $K_S\pi^0$ production may be separated from $K\pi_3$ candidates on the basis of the $\pi^+\pi^-$ mass alone. The distribution of the vertex along the beam direction for the event sample is shown in Figure 16b and is concentrated in the decay region. Neutron interactions in the material at either end of the decay region contributed a slowly varying component to the charged mass distribution. We will describe below each of the three components of the K' data: the $K_L \to \pi^+\pi^-\pi^0$ events, the $K_S\pi^0$ events, and the neutron events.

In order to reduce the neutron background, extra photons with an energy larger than 10 GeV were disallowed and, for $K\pi_3$ candidates, the vertex was

Figure 16. Distribution of a) the $\pi^+\pi^-$ invariant mass and b) the reconstructed vertex along the beam direction for events in which two charged particles and one π^0 were reconstructed. Neutron interactions in material at either end of the decay region contributed a smoothly varying component to the mass distribution.

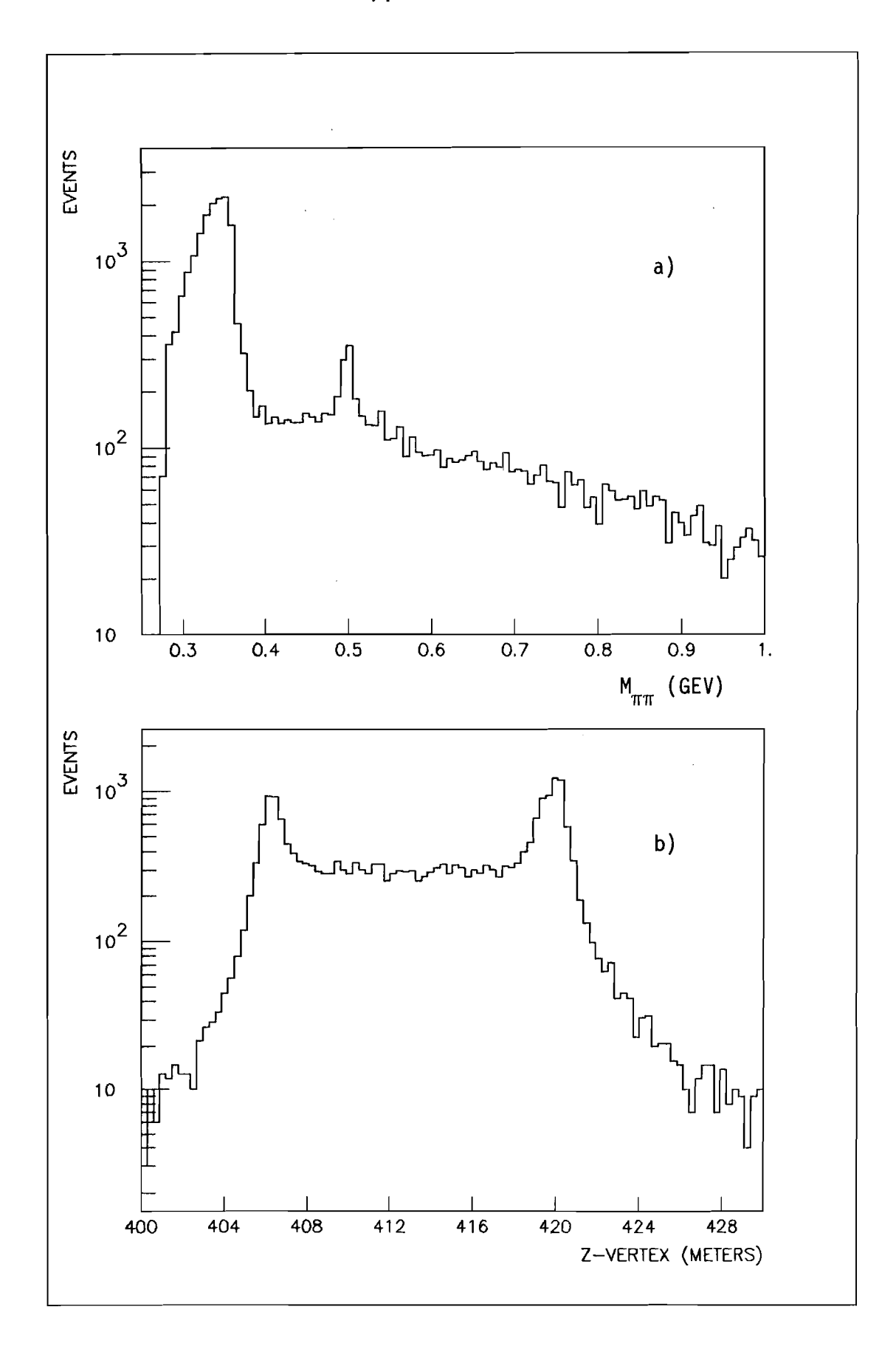


Figure 17. Distribution of the $\pi^+\pi^-$ invariant mass for $K\pi_3$ events. The Monte Carlo prediction is superposed. A cut at .38 GeV was applied.

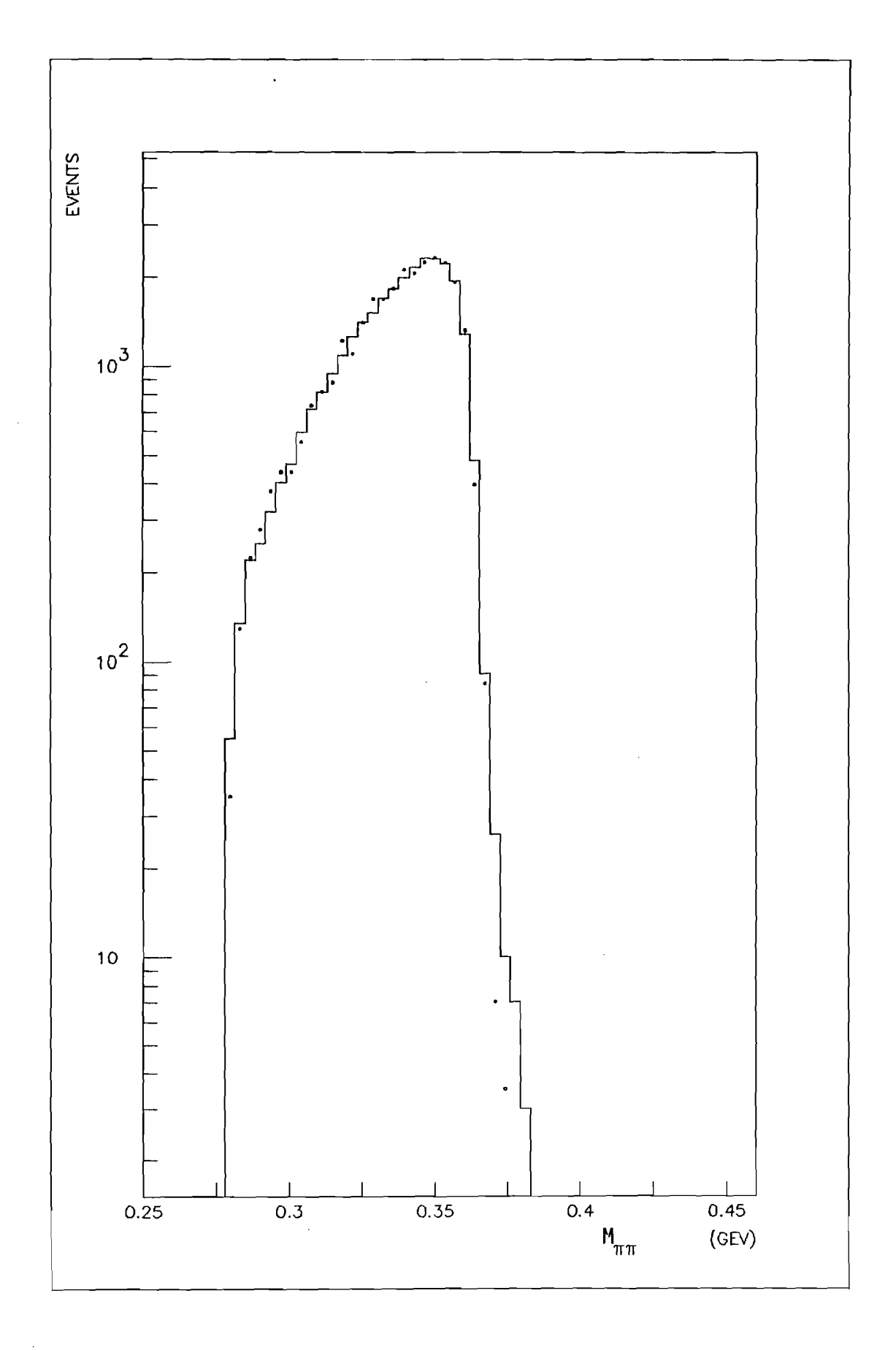


Figure 18. Distribution of the $\gamma\gamma$ invariant mass for $K\pi_3$ events. The Monte Carlo prediction is superposed.

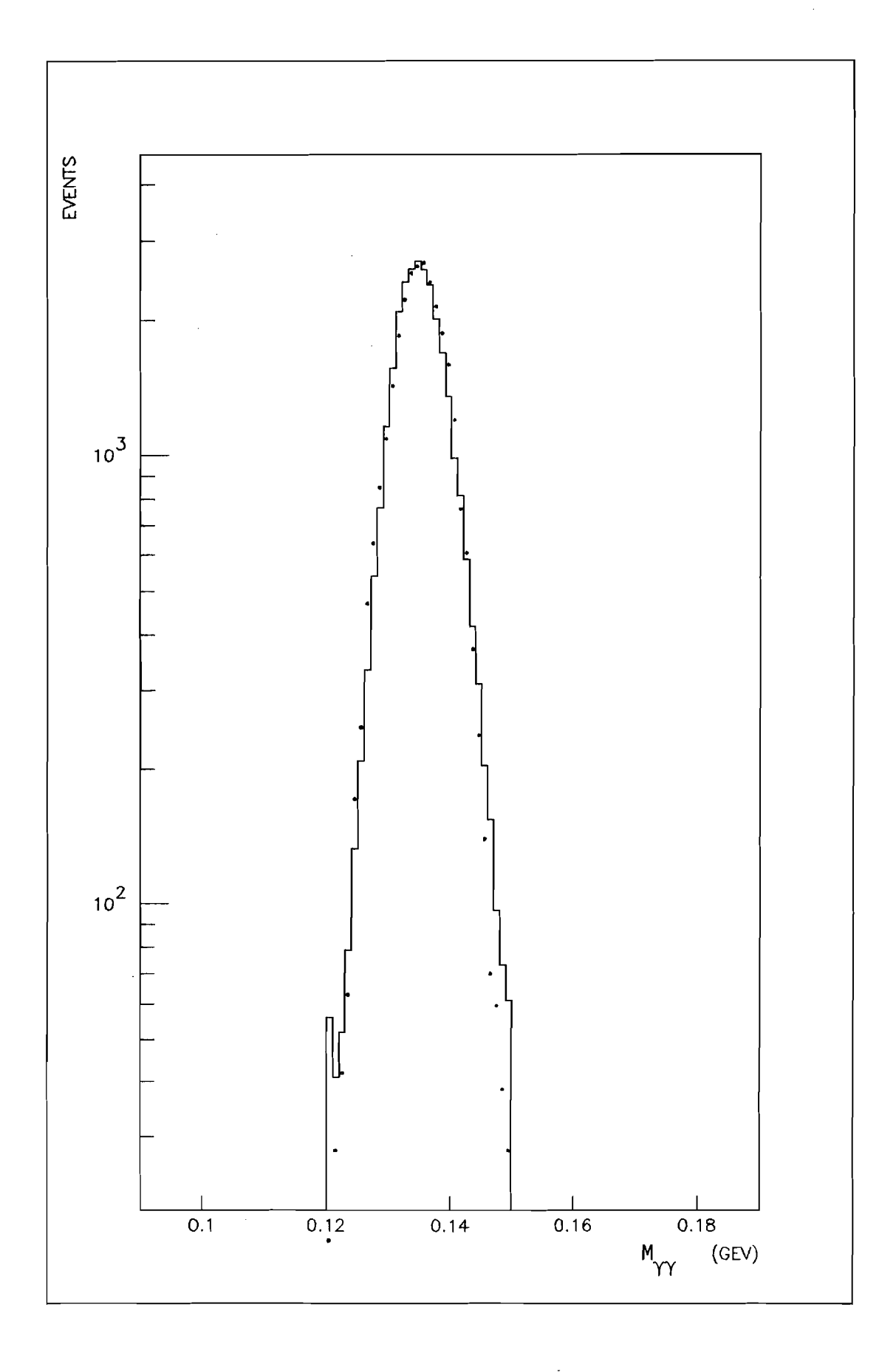


Figure 19. Distribution of the $\pi^+\pi^-\pi^0$ mass for $K\pi_3$ events. The Monte Carlo prediction is superposed.

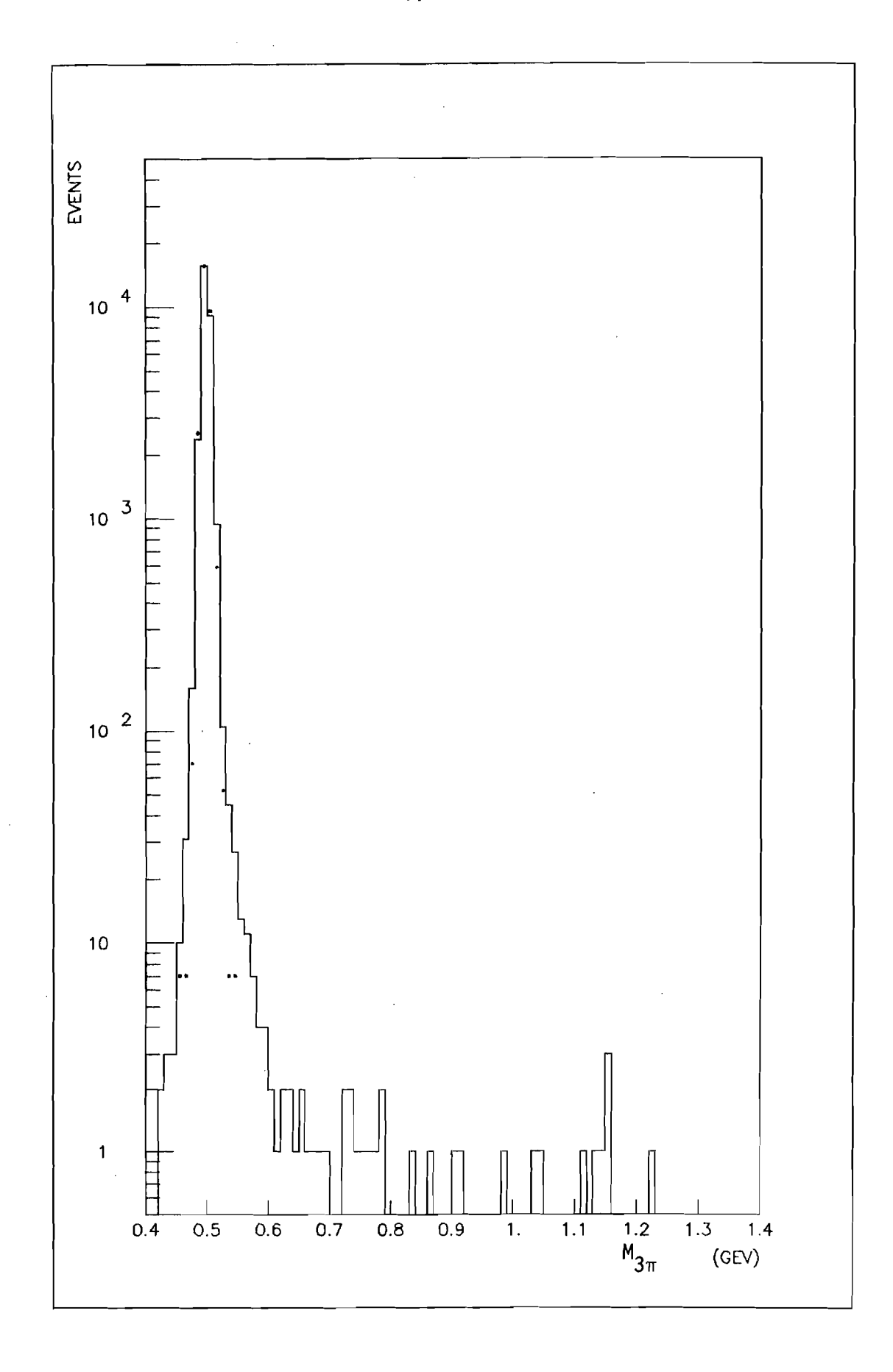


Figure 20. Transverse momentum distributions for $K\pi_3$ events for the two targets. The Monte Carlo predictions are superposed.

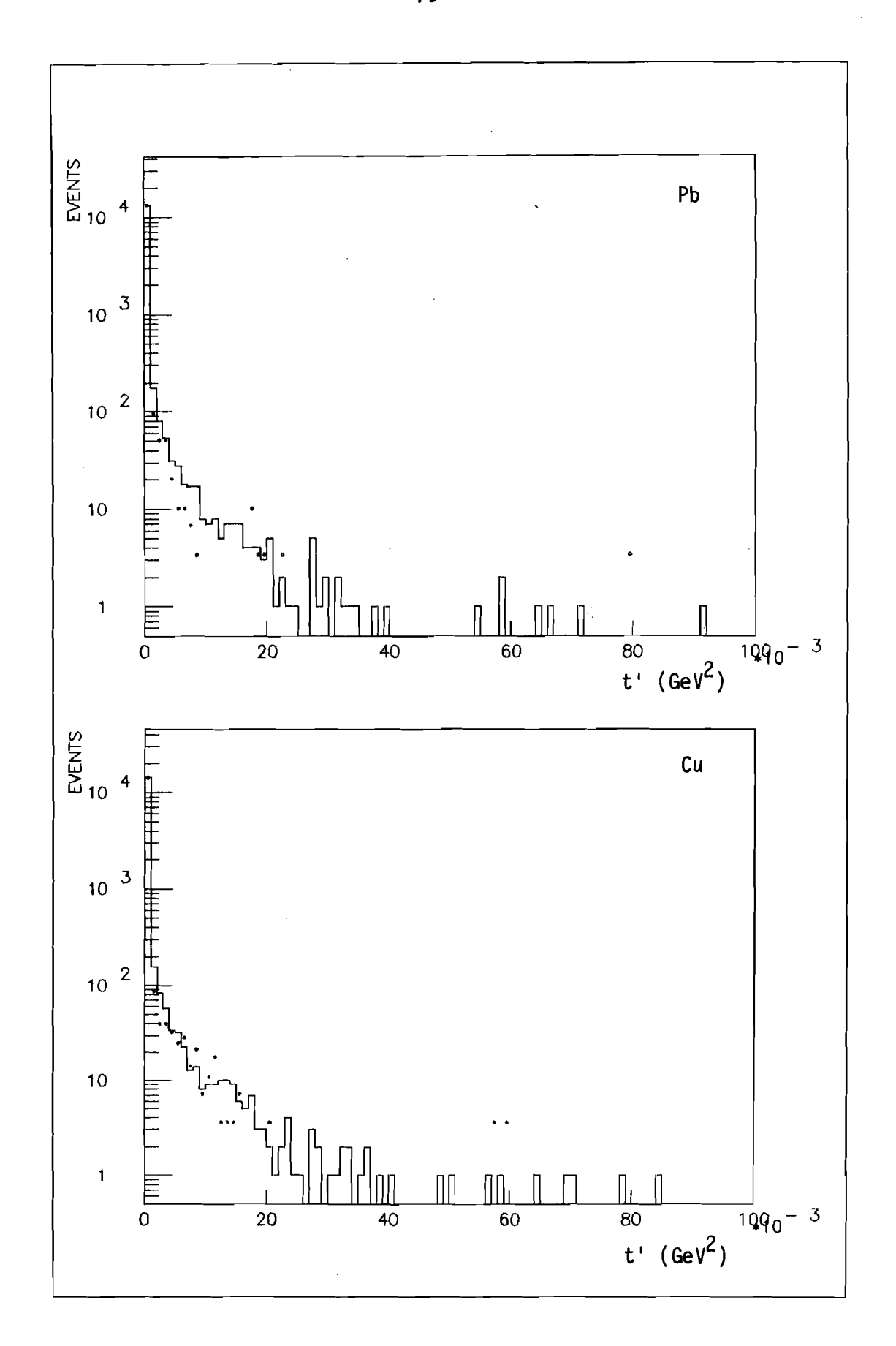
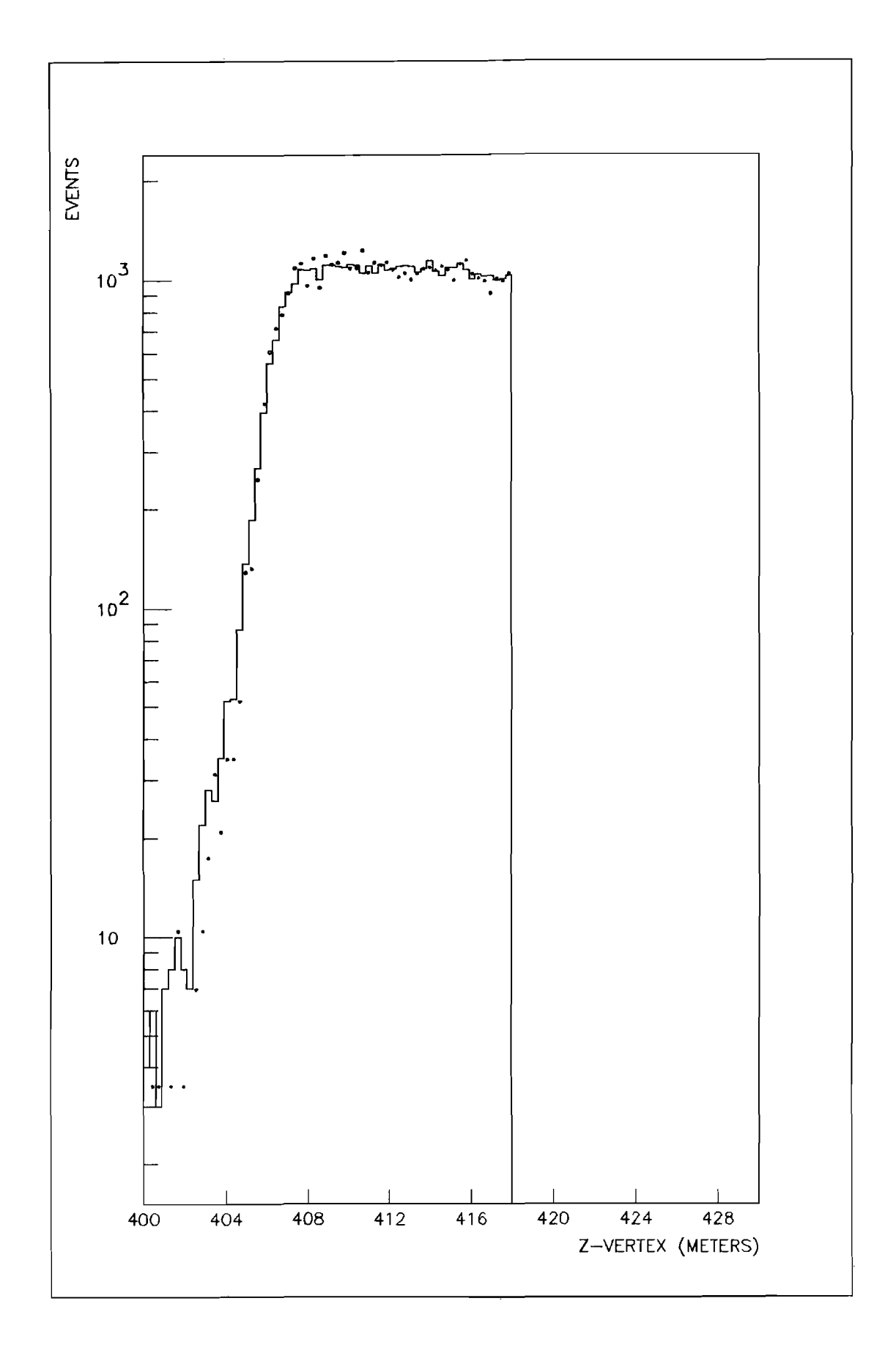


Figure 21. Vertex distribution for $K\pi_3$ events before the application of the upstream vertex cut. The Monte Carlo prediction is superposed.



required to be within the range 410-418 meters, while for K^{\bullet} candidates, the vertex was required to be less than 418 meters. A vertex cut at the upstream end of the decay region for K^{\bullet} candidates involved an unacceptable loss of events. In addition, the μ hodoscope was placed in veto to suppress events in which a pion decayed in flight.

B.
$$K_L \rightarrow \pi^+ \pi^- \pi^o$$
 Events

A sample of $K_L \rightarrow \pi^+\pi^-\pi^0$ decays were selected by the requirements that the $\pi^+\pi^-\pi^0$ invariant mass be in the range .47 - .53 GeV and that the transverse momentum squared be less than .02 GeV². In Figures 17-21, distributions of kinematic variables for $K\pi_3$ decays are compared with Monte Carlo predictions. The distribution of the $\pi^+\pi^-$ mass (Figure 17) reflects the kinematics of the decay as observed in the laboratory. The $\gamma\gamma$ mass distribution (Figure 18) is approximately Gaussian and the resolution was well simulated. The $\pi^+\pi^-\pi^0$ mass distribution (Figure 19) showed that the background was reduced to a negligible level. There was a small tail in the distribution of transverse momentum squared (Figure 20) which was attributed to elastic scattering of the K_L beam in the K^{\bullet} targets although the exact shape was not well determined by our data. In Figure 21, the vertex distribution for select $K_L \rightarrow \pi^+\pi^-\pi^0$ decays, before the application of the upstream vertex cut, is shown. The resolution smearing of the upstream edge was well simulated by the Monte Carlo.

Flux normalization decays were cleanly separated from background. The agreement between data and Monte Carlo for the distributions of kinematic variables indicated that the acceptance was well understood. This was confirmed by comparisons between data and Monte Carlo of the illuminations at various aperatures in the apparatus.

C. $K^{\bullet} \rightarrow K_S \pi^{\bullet}$ Events

Decays of the K^* were selected using the mass constraint on the $\pi^+\pi^-$ system. In Figure 22, the $\pi^+\pi^-$ mass in the region of the K_S mass is shown. A clear K_S signal was seen on top of a flat background. The arrows indicate the cuts used to divide the events into K_S rich and K_S wing samples. The K_S rich sample contained the desired $K^* \rightarrow K_S \pi^0$ decays while the K_S wing sample was representative of the neutron background.

The $\pi^+\pi^-\pi^o$ mass for K_S rich events is shown in Figure 23, for various bins of transverse momentum for the two targets. At small t' a clear signal for K^o (890) production was seen. An almost pure K' (890) sample was selected by requiring a $K_S\pi^0$ mass in the range .8 to 1.0 GeV with t' < .01 GeV^2 . The vertex distribution for these events, shown in Figure 24, was characterized by the K_S lifetime. The vertex distribution of the neutron background was estimated from K_S wing events and was subtracted in order to better compare the K_S vertex distribution with the prediction of the Monte Carlo. The $\gamma\gamma$ mass distribution is shown in Figure 25. The projections of the decay angular distribution in the Gottfried-Jackson frame

Figure 22. Distribution of the $\pi^+\pi^-$ invariant mass in the neighborhood of the K_S mass. The arrows indicate the cuts which defined the K_S enriched sample.

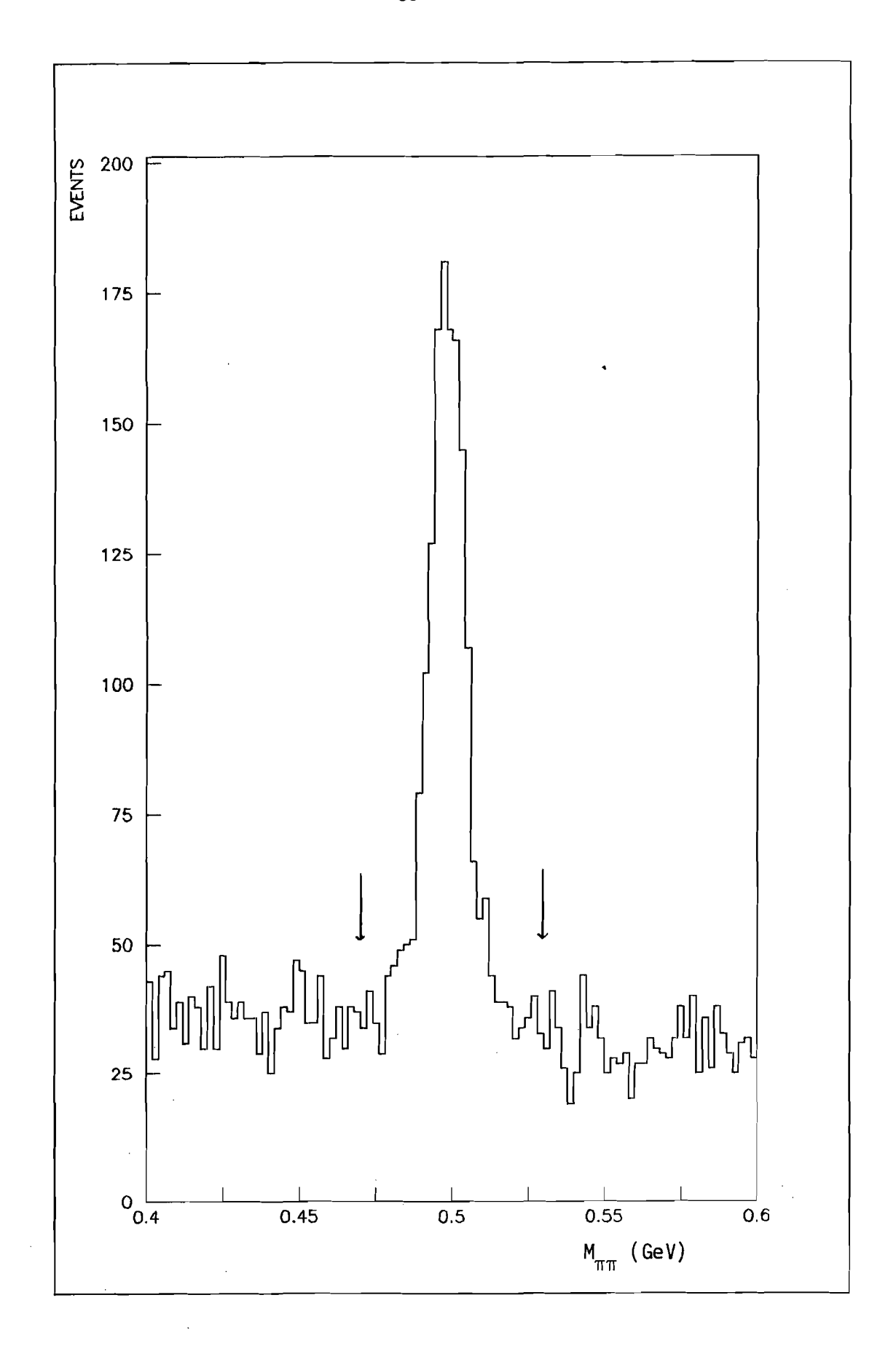


Figure 23. Distribution of the $K_S\pi^0$ invariant mass for the K_S rich event sample for various bins of t' for the two targets.

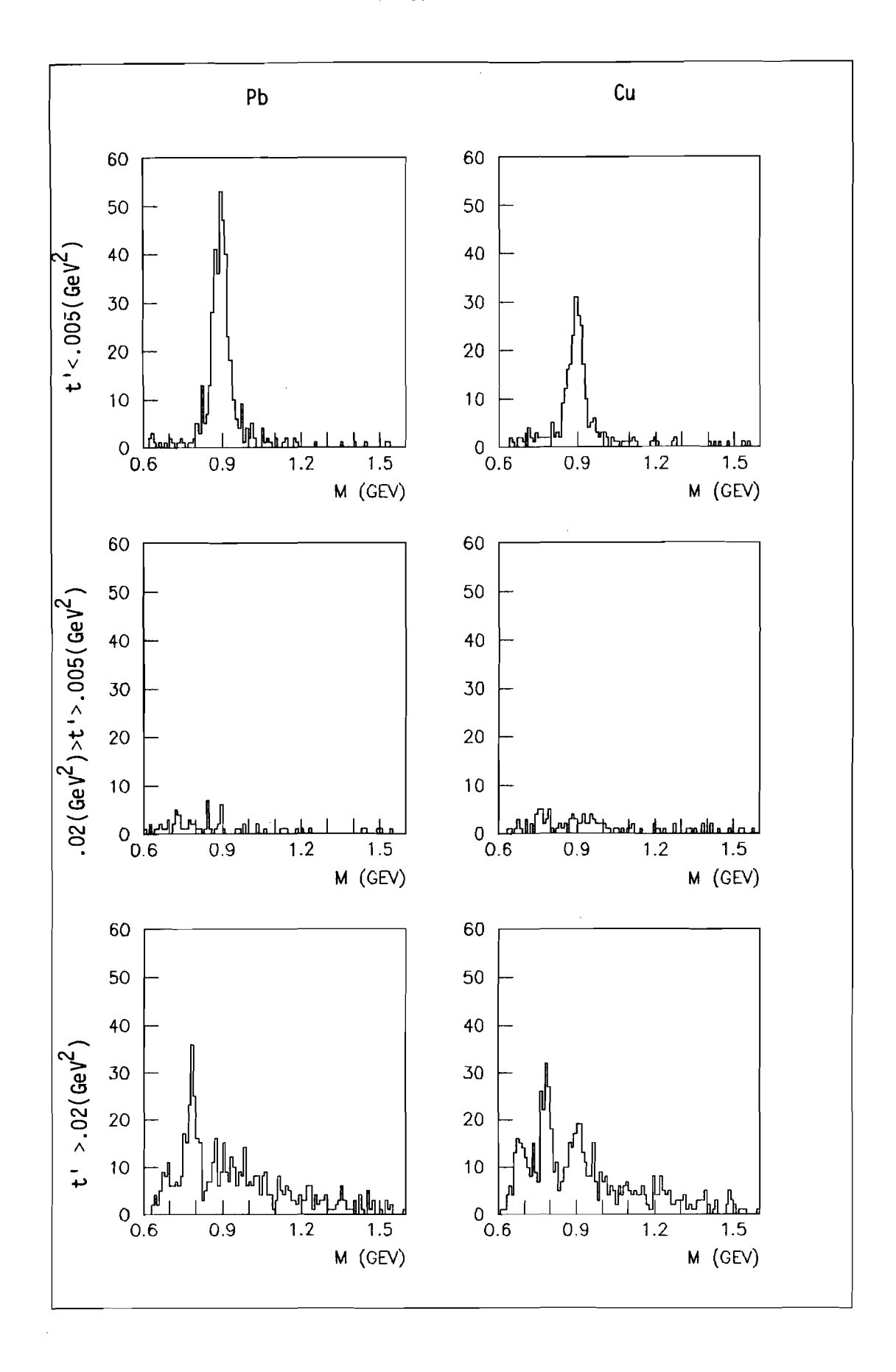


Figure 24. Distribution of the K_S vertex along the beam direction for $K^{\bullet} \to K_S \pi^{\bullet}$ events in the mass range .8-1.0 GeV^2 with $t' < .01 \; GeV^2$. The neutron background was subtracted in order to better compare with the Monte Carlo.

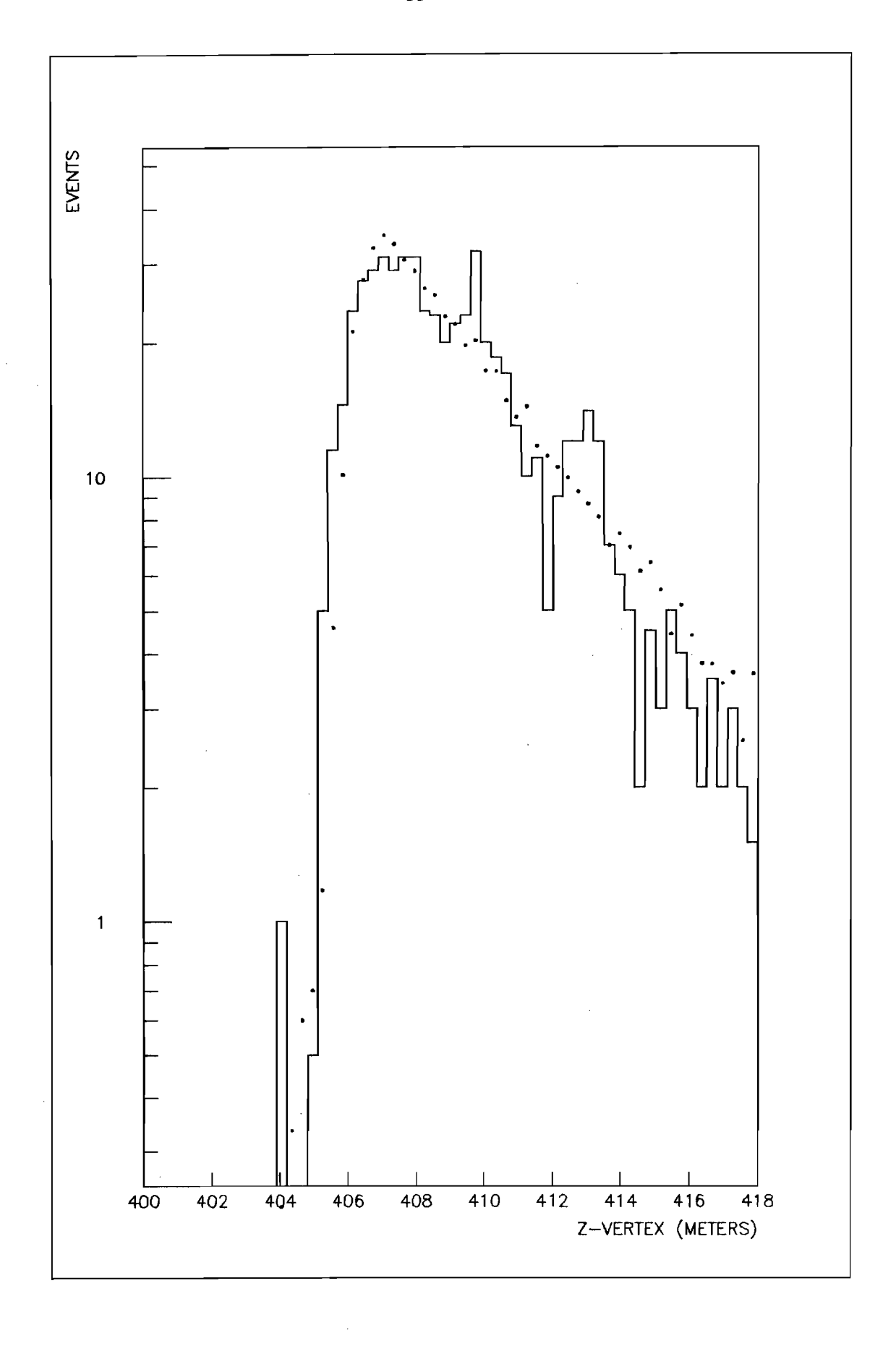


Figure 25. Distribution of the reconstructed π^o mass for $K^o \to K_S \pi^o$ events in the mass range .8-1.0 GeV^2 . The Monte Carlo prediction is superposed.

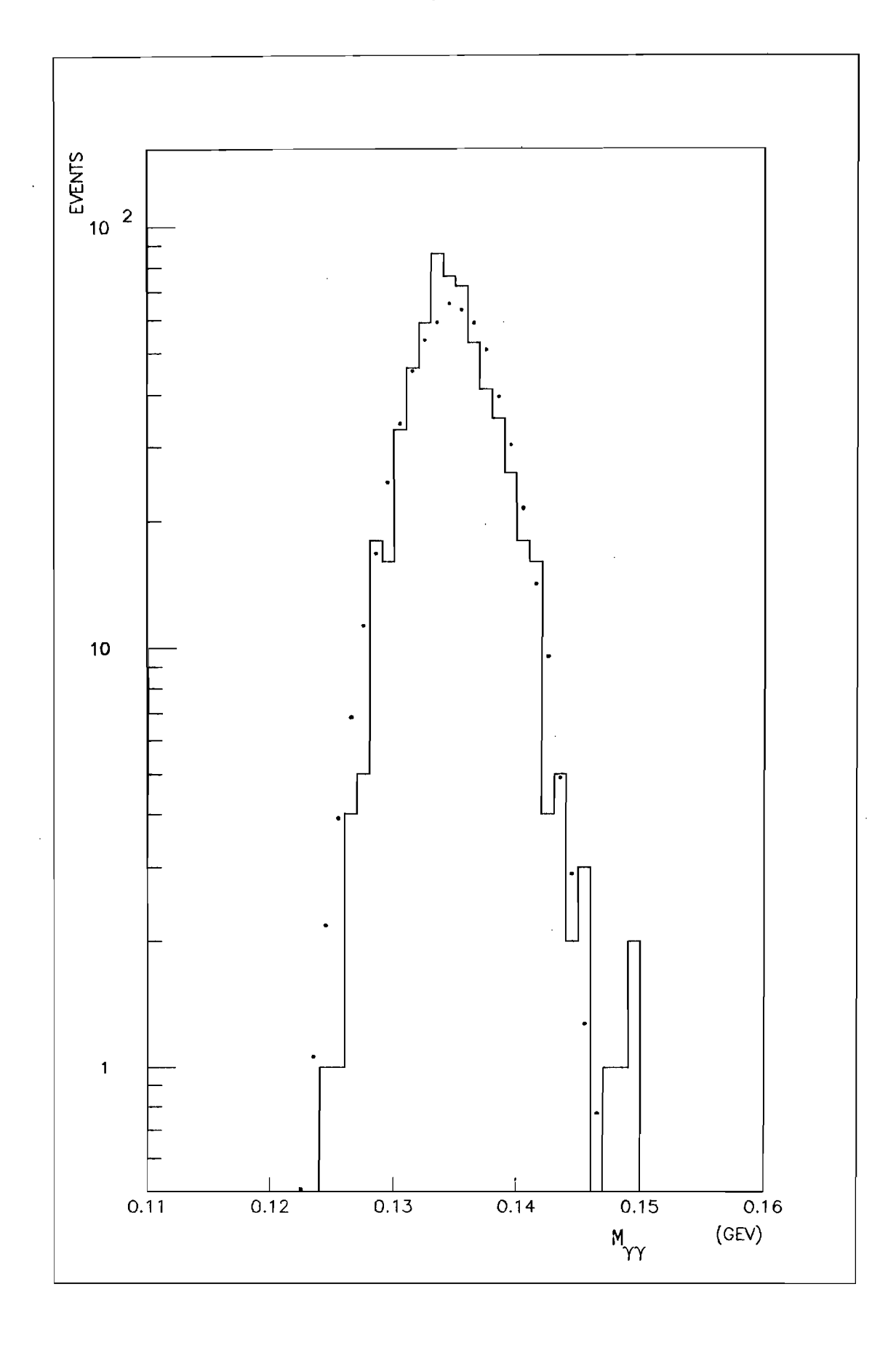


Figure 26. Decay angular distributions in the Gottfried-Jackson frame for $K^{\bullet} \rightarrow K_S \pi^{\bullet}$ decays. The prediction of the Monte Carlo is superposed.

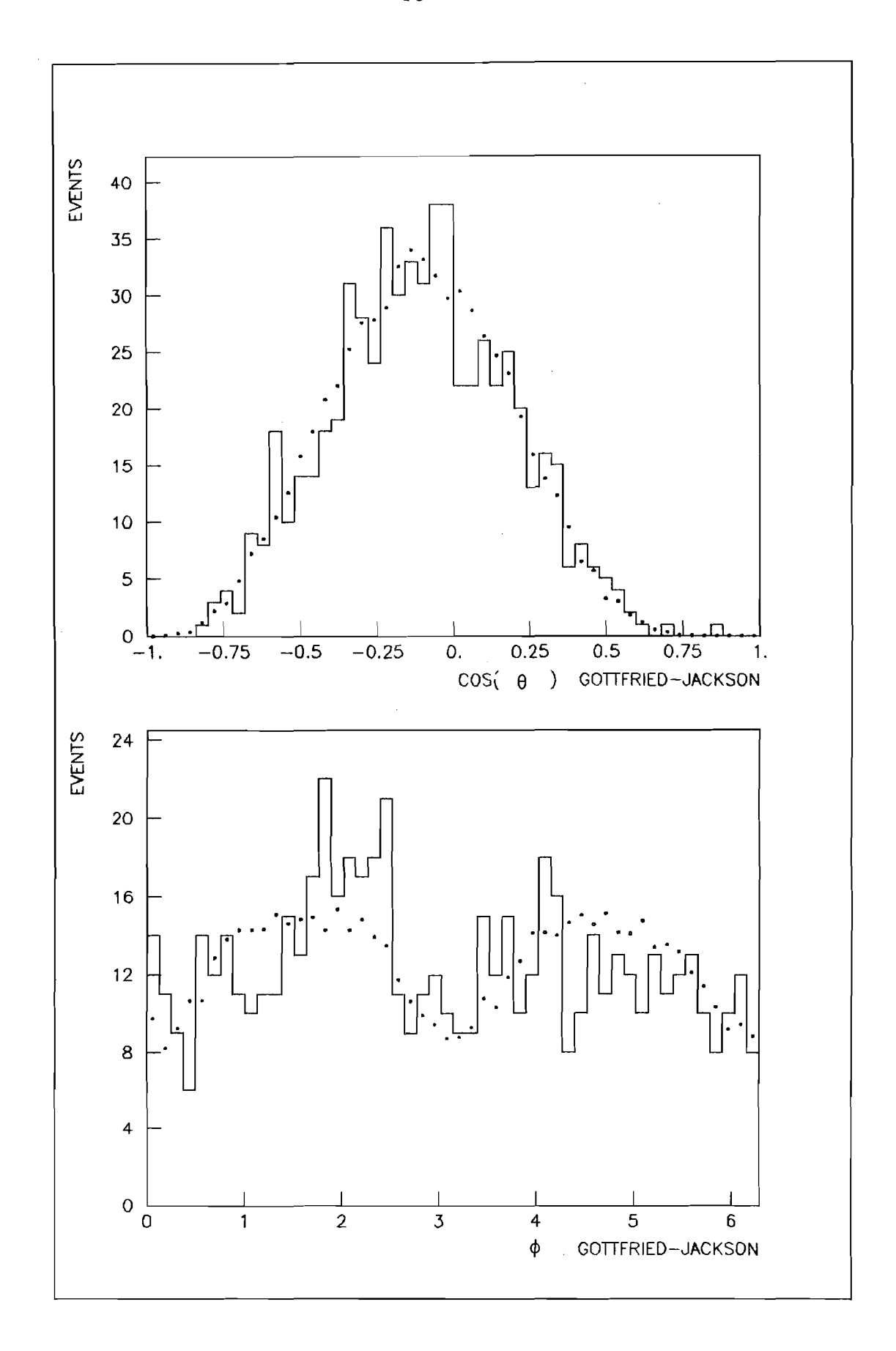
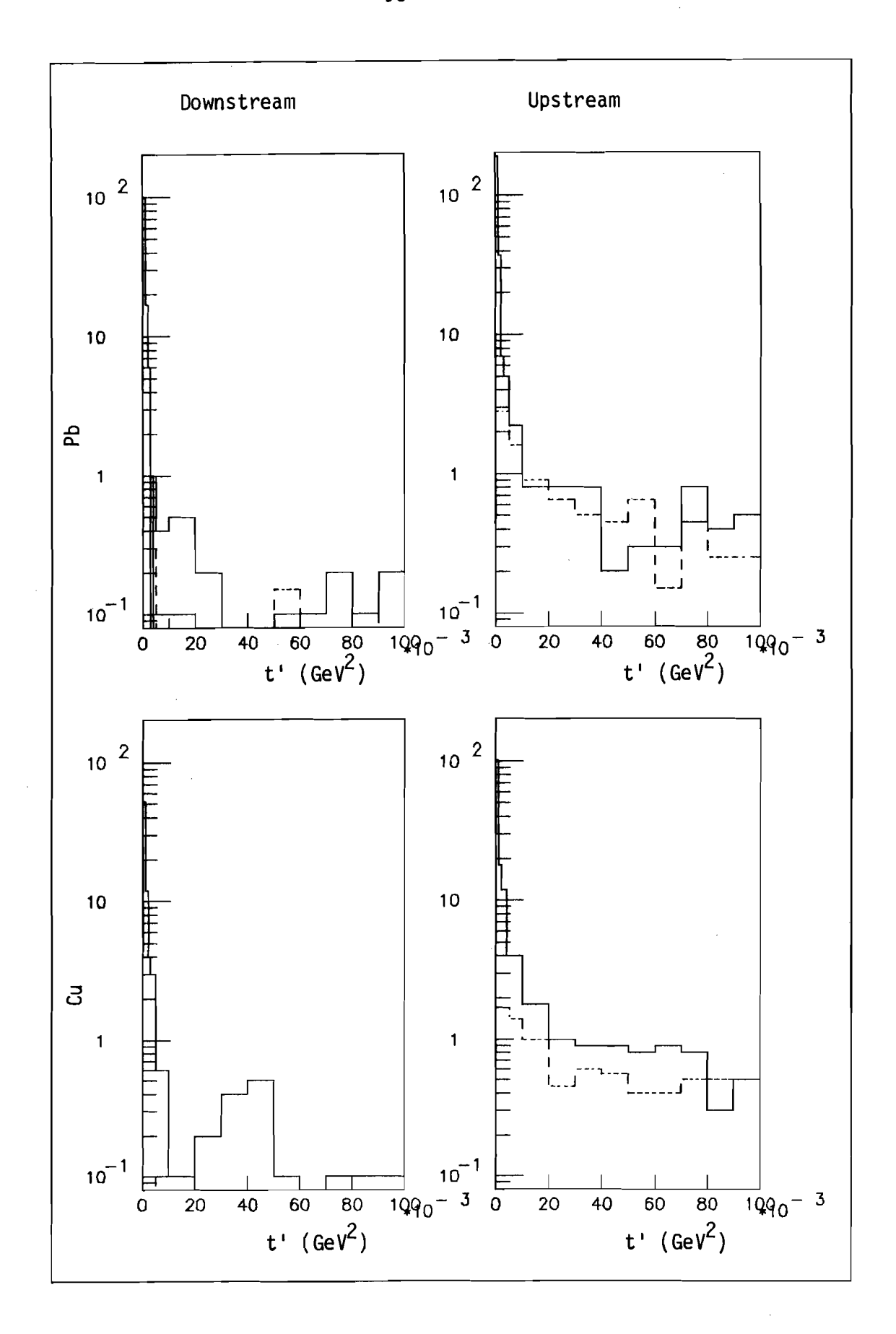


Figure 27. Transverse momentum distributions for K^{\bullet} events in the upstream and downstream regions of the decay volume for the two targets. Superposed are the estimates of the neutron background as determined from K_S wing events.



are exhibited in Figure 26 and were found to be consistent with the distributions expected for the Coulomb production of the K^{\bullet} (890). The shift in the centroid of the distribution in $\cos(\theta)$ was understood as an acceptance effect. The distribution in ϕ was subject to severe resolution effects which resulted from the fact that the definition of ϕ involves the normal to the production plane. In the forward direction, the production plane is not defined. Near to the forward direction a discontinuous resolution function for the variable ϕ results. This projection therefore contained very little information.

In Figure 27, the t' distributions for the two targets are shown for events for which the $K_S\pi^0$ mass was in the range .8-1.0 GeV. A boundary at 410.0 meters was used to divide the data according to the $\pi^+\pi^-$ vertex position into upstream and downstream samples with the downstream sample observed to be comparatively neutron background free. The neutron background as estimated from K_S wing events is also shown. The estimate represents all events from the charged mass ranges .41 - .47 GeV and .53 - .59 GeV which satisfied the other cuts imposed on the K' candidates, with each event given a weight of 1/2. According to this background estimate, the observed $K' \rightarrow K_S\pi^0$ events were produced almost exclusively at small momentum transfer.

D. Neutron Background Events

In order to understand the neutron background to the $K^{\bullet} \rightarrow K_S \pi^{\bullet}$ signal, the K_S wing events were studied with various mass hypotheses, ie. under the

assumption that the charged tracks were combinations of pions, kaons, and protons. An identifiable A decay mass signal was seen in the distribution of the mass of the two charged particles under the hypothesis that the positively charged track was a proton and that the negatively charged track was a π^- . The energy sharing in the A decay is highly asymmetric in the lab frame and may be characterized by an asymmetry parameter which is defined in terms of the magnitudes of the particle momenta by $ASYM = (|\vec{p}| - |\vec{\pi}|) / (|\vec{p}| + |\vec{\pi}|)$. Decays of Λ 's were eliminated by removing events for which ASYM > .6 in coincidence with the mass cuts shown in Figure 28. No other stable particles were identified. In particular, no $\overline{\Lambda}$ signal was seen which indicated that the A's were produced predominately by neutrons, rather than by the K_L 's in the beam. Also, no charged hyperon signal was seen which suggested that the observed hyperons were produced in the K' targets rather than in the window downstream of the RA counters. The remaining K_S wing events resulted from unstable particle production. In Figure 29, the $\pi^+\pi^-\pi^0$ mass spectrum is shown. A clear ω signal was seen on top of a smoothly varying background. No other unstable states were identified.

Figure 28. Proton-pion invariant mass distribution. The momentum asymmetry variable ASYM defined in the text was required to exceed 0.6. The arrows indicate the cuts used to eliminate Λ decays.

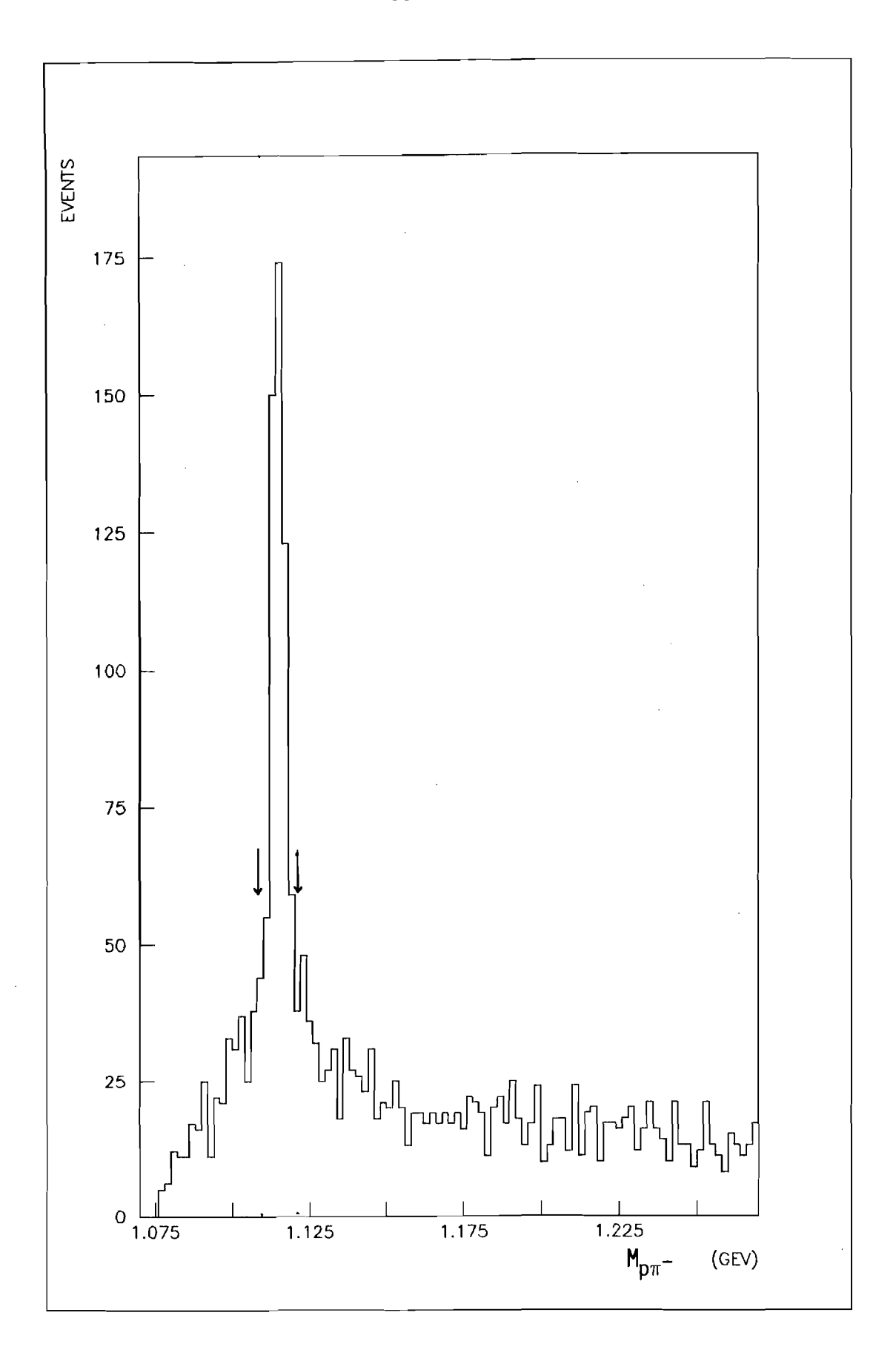
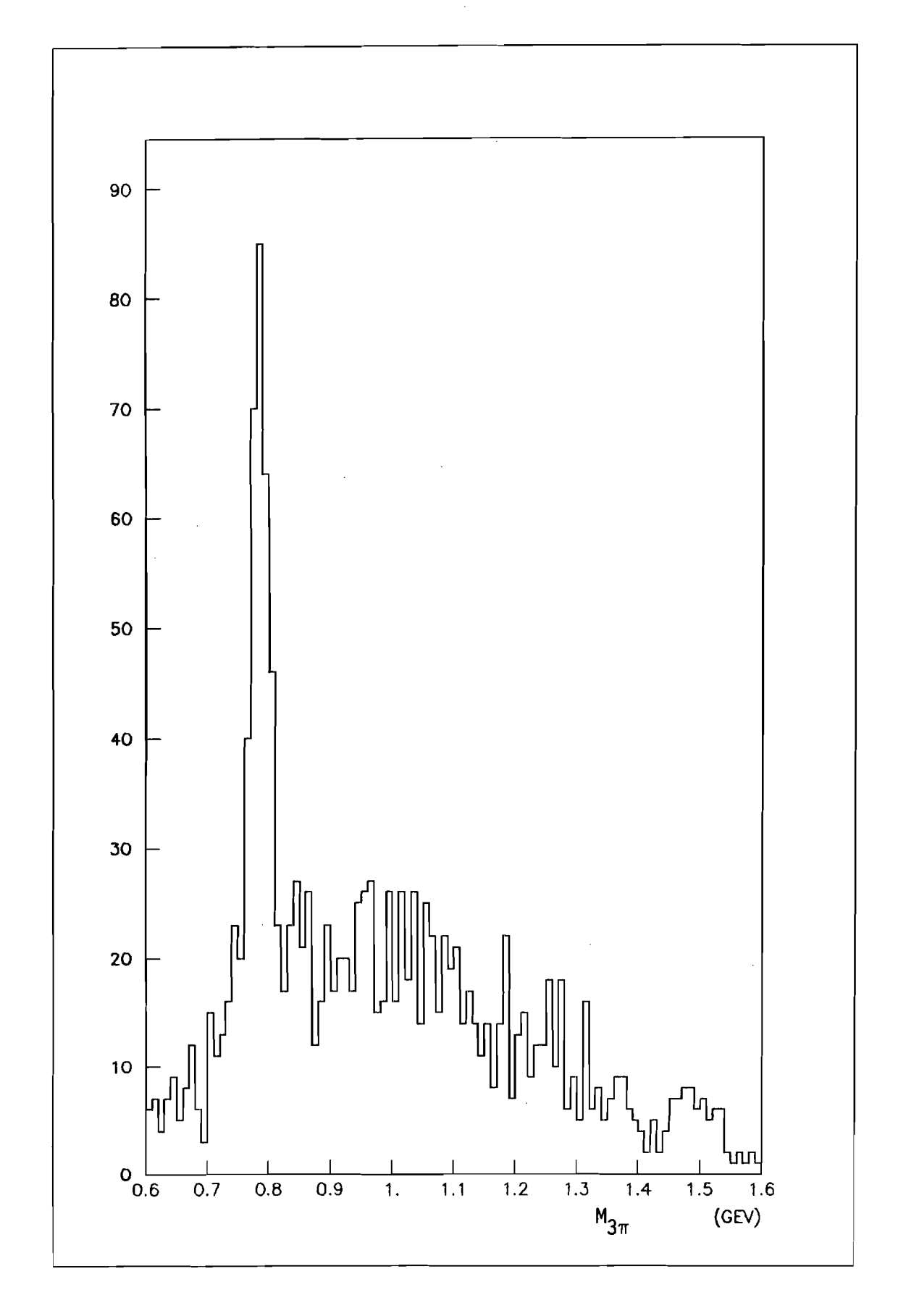


Figure 29. Distribution of the $\pi^+\pi^-\pi^0$ mass for K_S wing events. The peak corresponds to $\pi^+\pi^-\pi^0$ decays of the ω .



CHAPTER V

NORMALIZATION OF OBSERVED K' DECAYS

In this chapter, we describe the normalization of the observed $K' \rightarrow K_S \pi^o$ decays. The production cross section for each target was determined from the number of K' decays in bins of transverse momentum according to the formula:

$$\frac{d\sigma}{dt'} = \frac{\Delta N^{\circ}/\Delta t'}{\left\{T \frac{N_o}{A} \cdot F \cdot E \cdot CF\right\}}$$
 (5.1)

where ΔN^{\bullet} is the number of events in the $K_S \pi^{\bullet}$ invariant mass range .8-1.0 GeV^2 and in the t' bin $\Delta t'$, T is the thickness of the target in gm/cm^3 , $N_o=6.022\times10^{23}$ is Avogadro's number, A is the weight of the target material, the flux factor F is the number of K_L mesons which passed through the target, E is the efficiency of the apparatus for detecting $K^{\bullet} \rightarrow K_S \pi^0$ decays including the geometrical acceptance and losses in the event selection, and CF represents a product of correction factors. In each t' bin, the neutron background was estimated using the K_S wing events and subtracted. The efficiency factor was determined by applying the same event reconstruction and event selection criteria to Monte Carlo simulated data as were applied to real data. The factor CF included corrections for branching ratios, for losses not included in the Monte Carlo determination of the efficiency, and for empty target background. These corrections are listed in Table 4. A K^0 (890) $\to K^0$ π^0 branching ratio of 1/3 and the world average $K_S \to \pi^+\pi^-$ branch-

103
TABLE 4
NORMALIZATION CORRECTION FACTORS

Copper	Lead
1/3	1/3
0.6861±.0024	0.6861±.0024
0.7227±.0033	0.4692±.0019
0.9865±.0002	0.9865±.0002
1.0320±.0070	1.0130±.0010
	1/3 0.6861±.0024 0.7227±.0033 0.9865±.0002

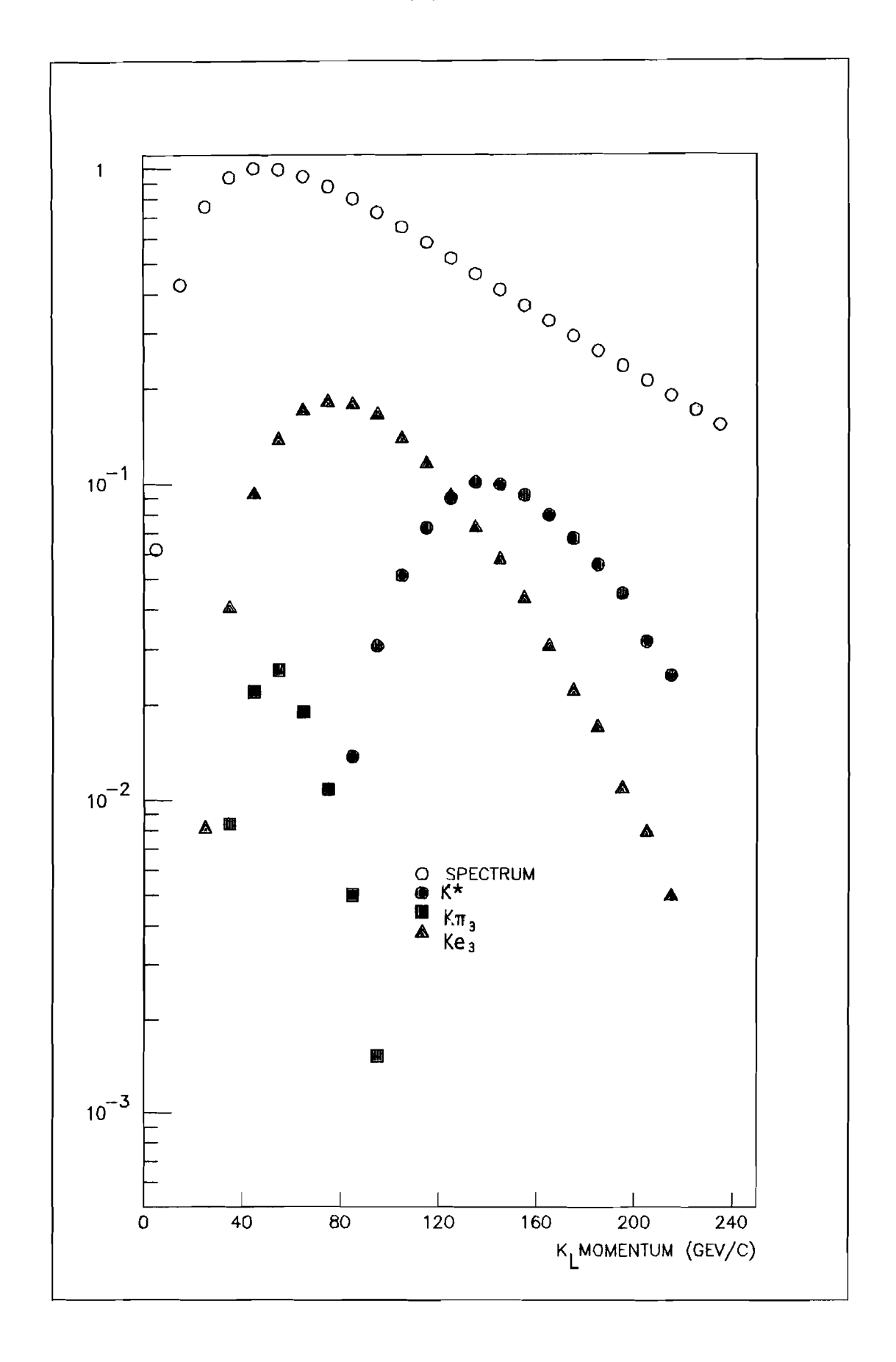
ing ratio were assumed. No correction for the $\pi^0 \rightarrow \gamma \gamma$ branching fraction was required as this decay was common to the K' and $K\pi_3$ events. A correction for photon conversion in the K' targets was calculated using theoretical pair production cross sections. 18 Photon conversion elsewhere in the apparatus was common to the K' and $K\pi_3$ events with the exception of conversions in material such as the RA counters and the vacuum window at the upstream end of the decay region between the K' production target and the upstream vertex cut applied to the $K\pi_3$ events. A correction for this difference was required. A fractional empty target background correction was made. To calculate this correction, the acceptances for Coulomb production in material both upstream and downstream of the K' production targets were found with the Monte Carlo. Coulomb production rates were calculated for each type of material relative to the rate for production in the K' targets and pair conversion losses due to the presence of the targets were included. The empty target background calculation was checked with a search for Coulomb excitation in the charged mode data. The expected number of $K' \rightarrow K_S \pi^0$ events due to Coulomb production in extraneous material in the "empty beam" was predicted on the basis of the K' data. Accounting for the acceptance difference between the two triggers and using the Ke₃ decays for absolute flux normalization, 6±3 events were expected in the mass range .8 to 1.0 Gev and the t' range range $t' \le .01$ GeV^2 . We observed 5 ± 2 events.

The incident K_L flux in each beam was calculated by correcting the observed number of $K\pi_3$ events for detection efficiency and for the $K_L \rightarrow \pi^+\pi^-\pi^0$ branching

ratio. It was important to account for the variation of the flux with momentum. The $K\pi_3$ events were observed at a lower momentum than the $K^* \rightarrow K_S \pi^0$ events. In order for the observed $K\pi_3$ events to provide the flux normalization in the momentum range over which the K^* events were observed, we required a knowledge of the shape of the incident momentum spectrum. We measured the shape over the widest possible momentum range using Ke_3 events selected from the charged mode data set. In Figure 36, the acceptances for K^0 (890) events and $K\pi_3$ events for the K^* trigger are shown. The acceptance for Ke_3 events with the charged mode trigger is also shown in the figure and is seen to cover the entire momentum range. The shape of the momentum spectrum as determined from the Ke_3 events is also shown. Given the shape of the momentum spectrum, the flux at any momentum could be found by normalizing the spectrum shape to the observed number of $K\pi_3$ decays.

To determine the shape, a clean sample of Ke_3 decays was selected. The variable E/P was required to exceed .85 for one particle which was identified as the electron and to be less than this value for the other particle which was identified as the pion. To eliminate events due to neutron interactions, the reconstructed vertex was required to be within the range 410-418 meters. To eliminate $K\mu_3$ decays, the μ hodoscope was placed in veto and a minimum charged track momentum of 10 GeV was required. No photon candidate clusters with energy above 2.5 GeV were allowed. Residual background due to $K\pi_3$ events was eliminated by requiring that the kinematic variable $P_0^{\prime\prime}$ 2 be less than the kinematic minimum for $K\pi_3$ decays. 19

Figure 30. Momentum dependance of the acceptance for K^{0} , $K\pi_3$, and Ke3 decays. The Ke_3 decays were used to determine the shape of the momentum spectrum which is also shown (with arbitrary normalization).



After this cut, the size of the residual background was estimated to be 1.8% from a plot of E/P with all cuts applied except for a cut on the E/P variable itself.

The determination of the momentum spectrum from Ke_3 events was complicated by the fact that the neutrino was not observed and consequently the parent momentum could only be determined up to a two fold ambiguity. The two solutions solutions of the kinematic constraint equations for the parent momentum may be expressed in the form:

$$\begin{bmatrix} P_{high} \\ P_{low} \end{bmatrix} = \frac{\alpha P_{e,||} \pm E_e \sqrt{BRAC}}{E_e^2 - P_{e,||}^2} ; \alpha = \frac{m_K^2 - m_e^2}{2} ; BRAC = \alpha^2 - m_K^2 (E_e^2 - P_{e,||}^2)$$
(5.2)

Here, m_e is the $\pi^{\pm}e^{\pm}$ invariant mass, $P_{e,||}$ is the component of the observed momentum along the incident K_L direction which was given by the line between the proton target and the observed decay vertex, $E_e = E_x + E_e$ is the energy of the charged particle pair, and m_K is the K_L mass. To determine the spectrum, accounting for the ambiguity and for acceptance and resolution effects, the data was binned in both P_{high} and P_{low} and a fit was made to the resulting two dimensional distribution. Let A_{ij} be the number of $K_L \rightarrow \pi e \nu$ events found with P_{low} in the i-th momentum bin and with P_{high} in the j-th momentum bin. Let B_{ijk} be the probability that a K_L , incident upon the target with momentum in the k-th momentum bin, decayed in the decay region in the $\pi e \nu$ mode and was reconstructed to have P_{low} and P_{high} in the i-th and j-th momentum bins respectively. Let N_k be the K_L flux incident upon the target in the k-th momentum bin. Then we may write

$$A_{ij} = \sum_{k} B_{ijk} N_k \tag{5.3}$$

This is a matrix version of the integral equation relating the observed distribution of P_{high} and P_{low} to the incident spectrum. The flux N_k in each momentum bin was determined by numerical integration of a continuous spectrum chosen to correspond to the expected spectrum shape given a smoothly varying invariant K_L production cross section $\sigma_{inv}=Ed\sigma/d\vec{p}$ with account taken of decays between the K_L production point and the K^* production target:

$$\frac{dN}{dp} = \frac{p^2}{E} f(p)_{inv} e^{-\frac{m_E l}{E r}} ; \quad f(p)_{inv} = a (1-x)^b e^{-\epsilon x - dx^2}$$
 (5.4)

where x=p(GeV)/400, the energy is $E=\sqrt{m_k^2+p^2}$, l=406 meters is the distance of the K' targets from the K_L production point, and r=15.54 meters is the K_L decay length. The phenomenological form $f(p)_{ine}$ was characterized by four parameters (a,b,c,d) and was proportional to the invariant production cross section. The factor p^2/E converts the invariant cross section into the angular production cross section which when multiplied by the beam solid angle yields the flux in the beam. The exponential factor accounts for the decays which occur between the proton target and our apparatus. Acceptance and resolution effects were accounted for in the matrix B. This matrix was determined by applying to Monte Carlo data the same analysis routines as were applied to the real data to determine the matrix A.

The spectrum shape parameters were found by a numerical least squares solution of the matrix equation (5.3). The parameters resulting from the fit are given in Table 5. These parameters are highly correlated. The actual shape was found to be insensitive to the functional form assumed for f_{ins} . The spectrum was deter-

Parameter	Value	Covariance Matrix			
		a	b	c	d
a	.297 ×10 ⁶	.680×10 ⁸			
b	.275 × 10 ¹	.102×10 ⁴	$.127 \times 10^{-1}$		
c	.945 × 10 ¹	.180 ×10 ⁴	$.221 \times 10^{-1}$	$.398 \times 10^{-1}$	
d	851 ×10 ¹	669×10 ⁴	850×10 ⁻¹	152×10^{0}	.598 × 10°
		a	b	c	d

mined iteratively in that the results of the fit were used as input to the Monte Carlo and the matrix B redetermined. In fact, the fit was quite insensitive to the input spectrum in the Monte Carlo.

The spectrum shape as determined by this fitting procedure was checked in a number of ways. The goodness of fit ($\chi^2 = 1.3$ /d.o.f) indicated that the fit described the observed Ke3 data. A detailed check was provided by a comparison of distributions of kinematic variables between data and Monte Carlo. In Figure 31, the distribution of the variable BRAC defined above is shown. This variable is proportional to the square of the rest frame longitudinal component of neutrino momentum and is extremely sensitive to resolution effects. In Figure 32, the total observed charged momentum is shown. We show in Figure 33 the momentum distribution for unambiguous Ke3 events defined to be those for which $|P_{high}-P_{low}|/|P_{high}+P_{low}| < .1$. Good agreement with the Monte Carlo is found for these distributions. The observed distributions of transverse momentum and vertex as a function of momentum were also in agreement with the Monte Carlo predictions. The observed momentum distribution for $K_L \rightarrow \pi^+ \pi^- \pi^0$ events from the K^* data is compared in Figure 34 with the prediction of the Monte Carlo assuming the spectrum shape deduced from the Ke_3 events.

Additional checks were provided by the examination of other decay modes. CP violating $K_L \rightarrow \pi^+\pi^-$ decays were selected from the charged mode data set as follows. The μ hodoscope was placed in veto. The variable E/P was required to be less than .8 for both tracks. Photons were disallowed. The pion momenta were

Figure 31. Distribution of the variable BRAC (defined in the text) for $K \rightarrow \pi e \nu$ decays. The Monte Carlo prediction is superposed.

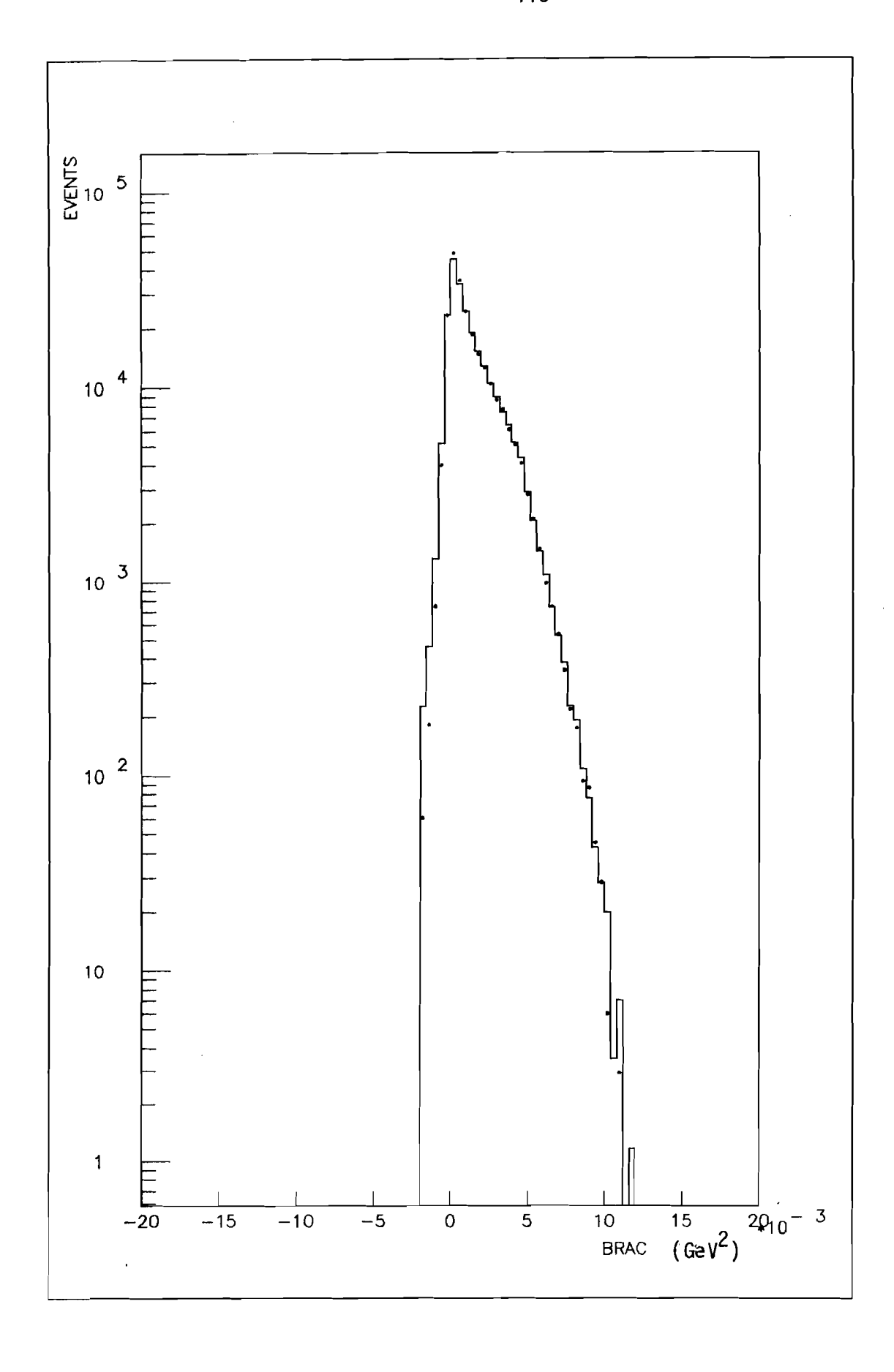


Figure 32. Distribution of the total reconstructed momentum for Ke_3 decays. The Monte Carlo prediction is superposed.

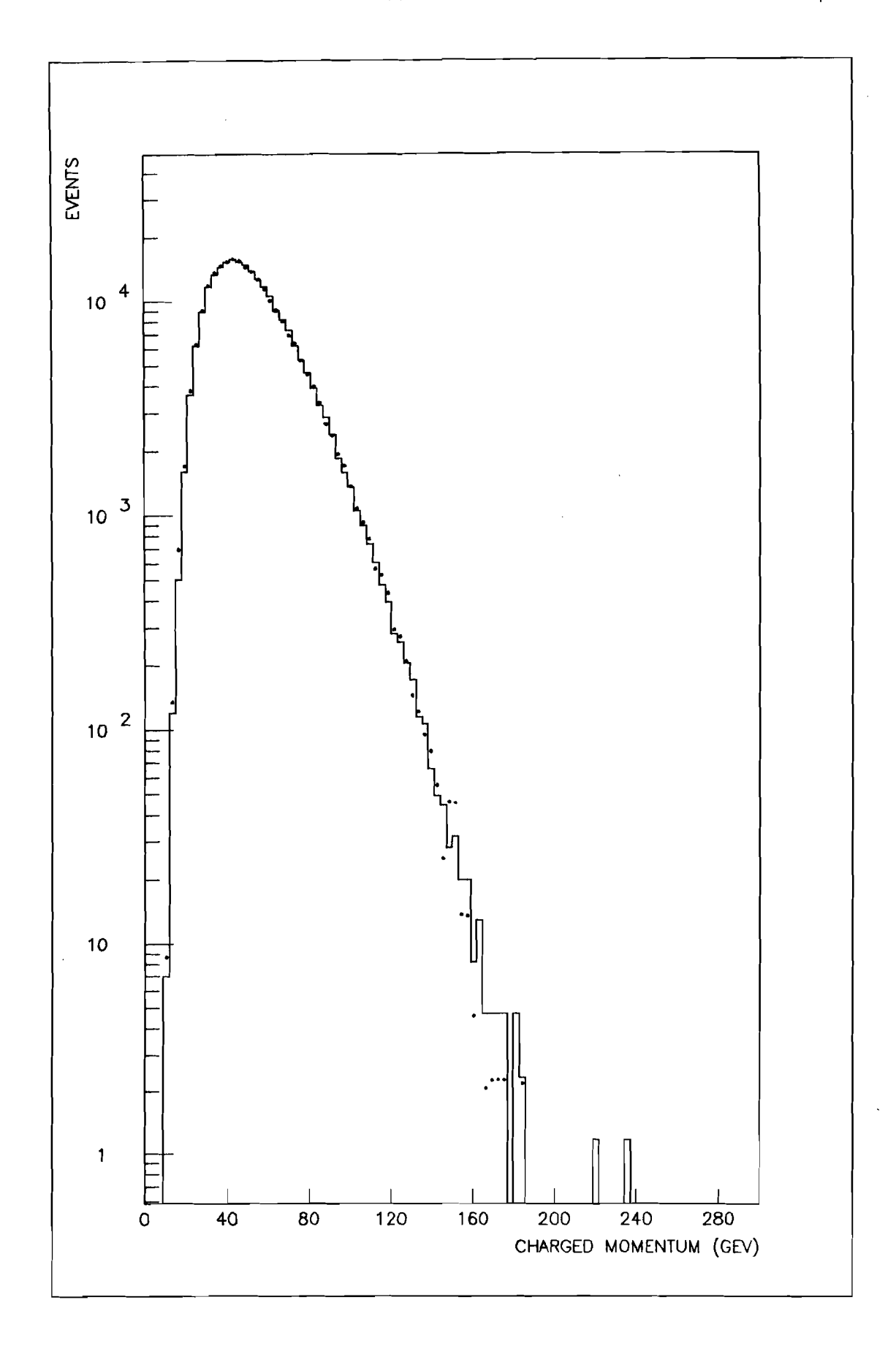


Figure 33. Distribution of the parent K_L momentum for unambiguous Ke_3 events. The Monte Carlo prediction is superposed.

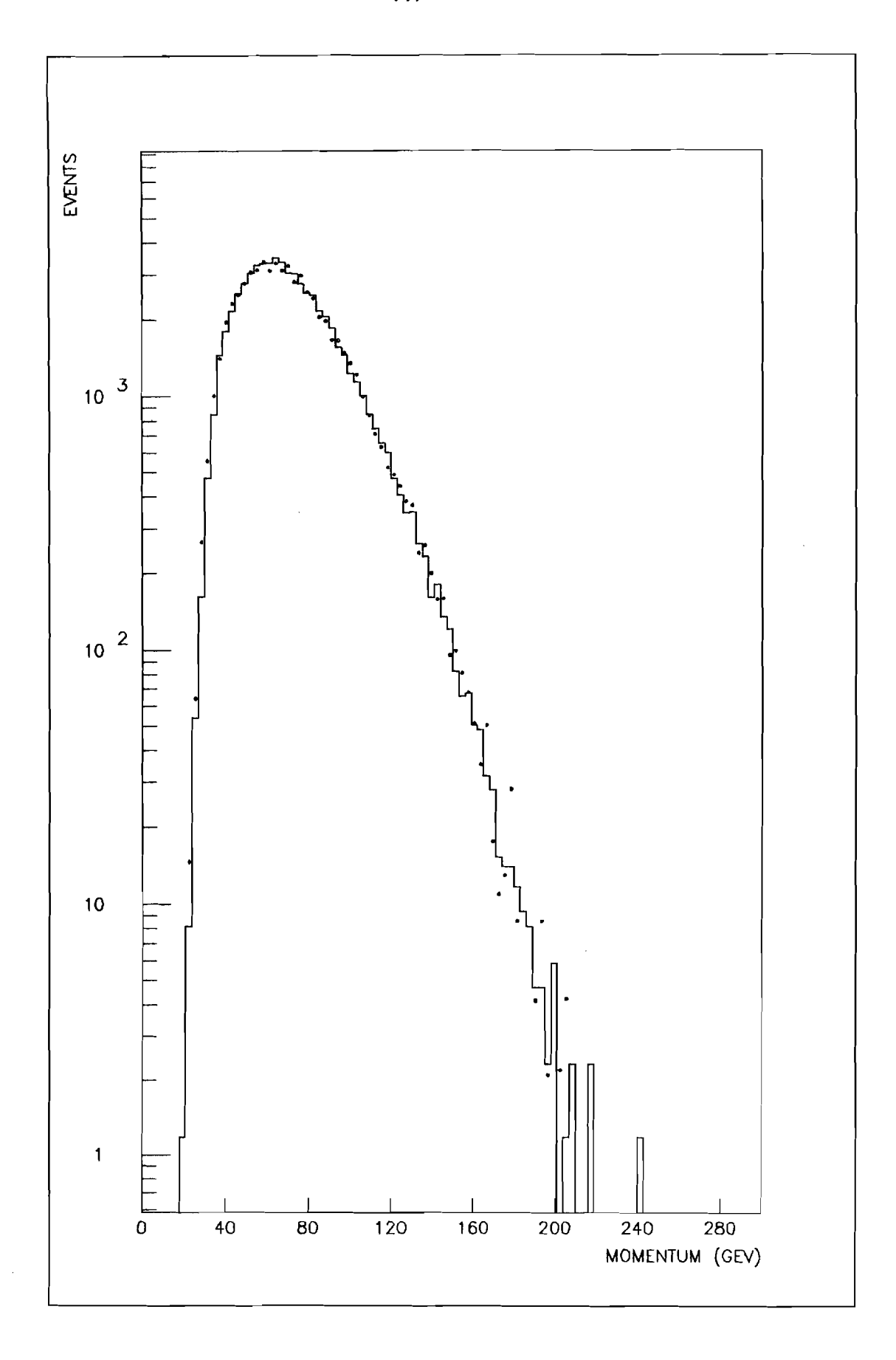


Figure 34. K_L momentum distribution for $K\pi_3$ decays. The Monte Carlo prediction is superposed.

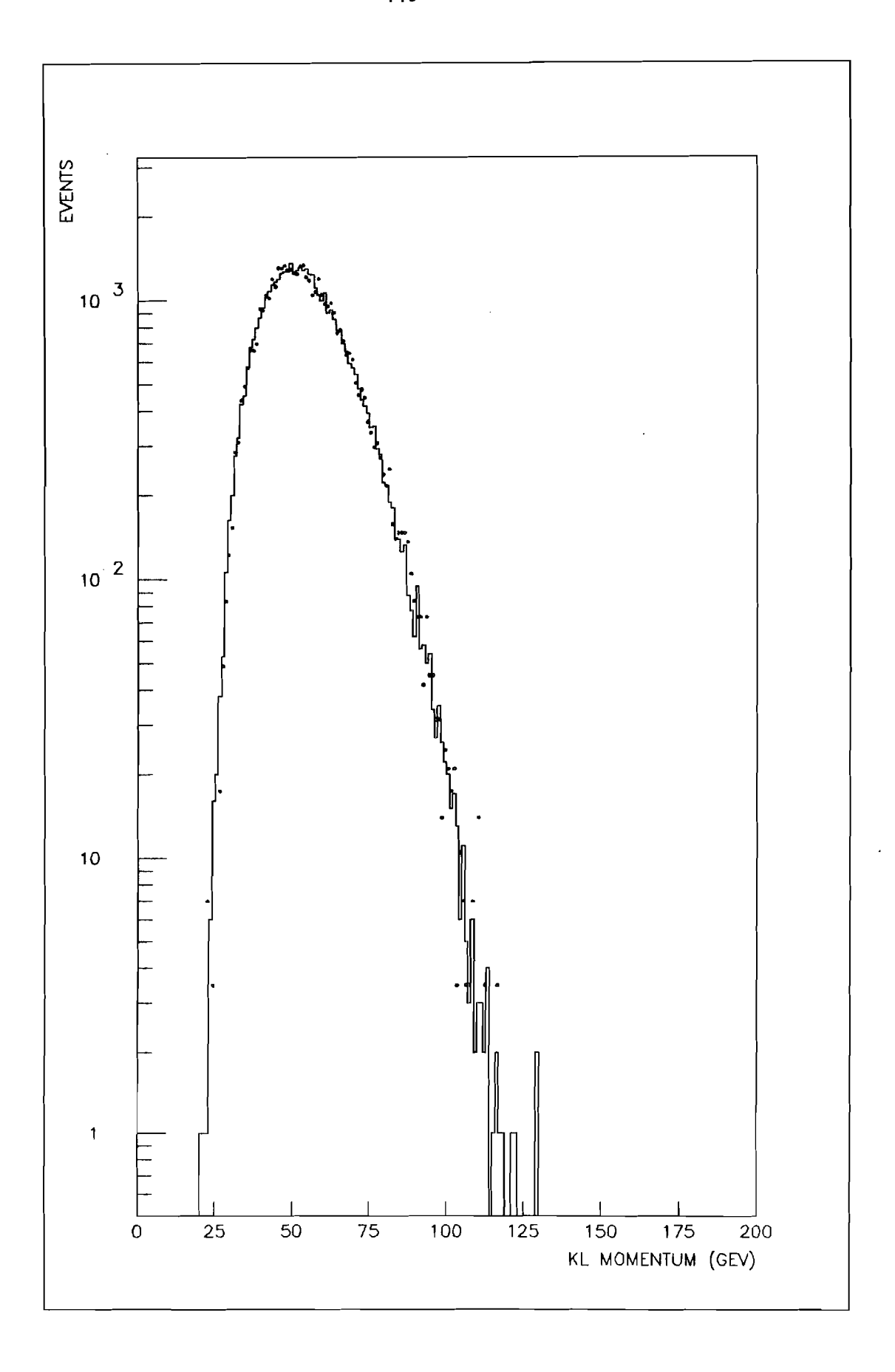


Figure 35. Distributions for $K_L \rightarrow \pi^+\pi^-$ decays. In the upper figure, the $\pi^+\pi^-$ mass distribution is shown and in the lower figure the transverse momentum distribution is shown. The Monte Carlo prediction is superposed.

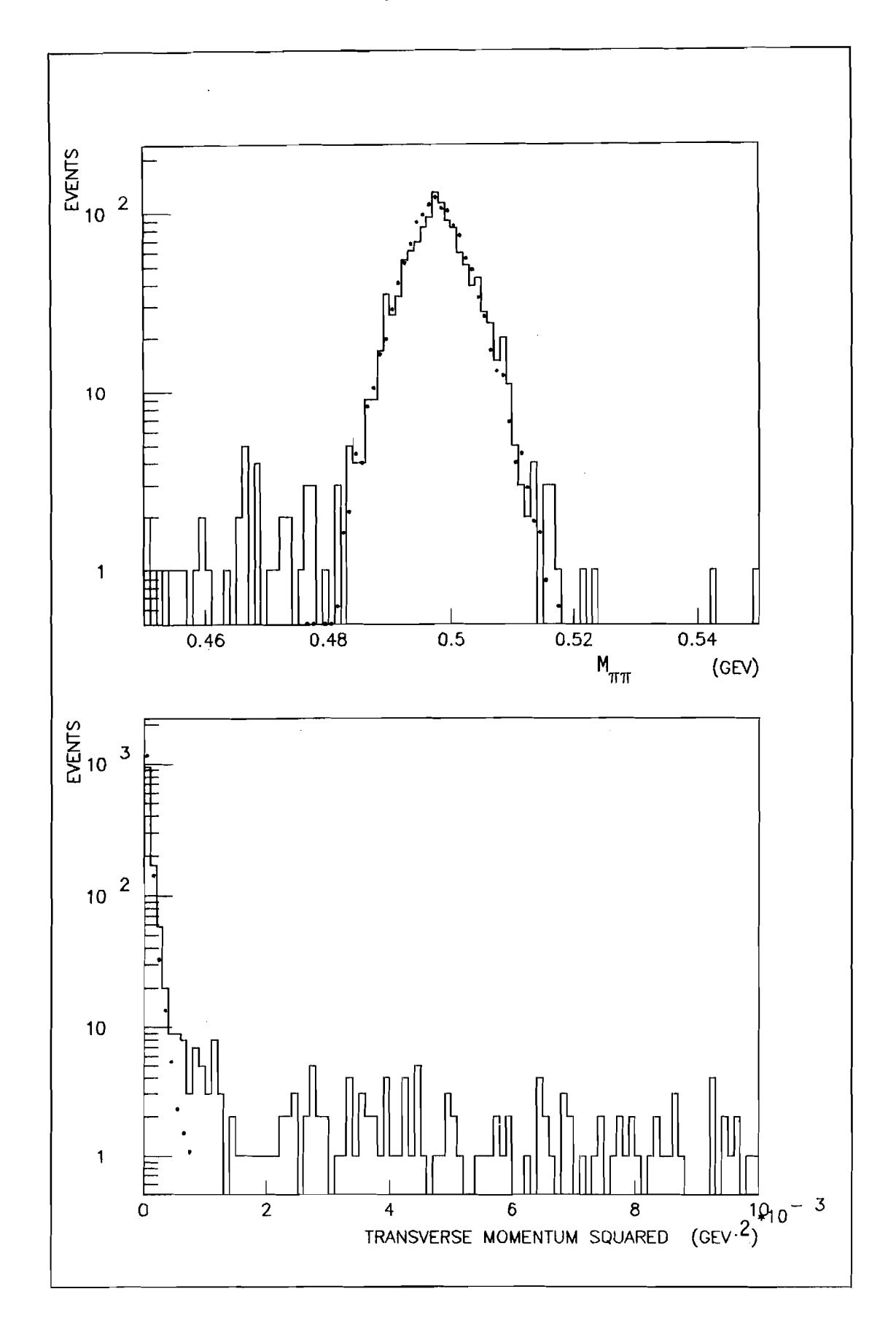


Figure 36. Momentum distribution for identified $K_L \rightarrow \pi^+\pi^-$ events. The Monte Carlo prediction is superposed.

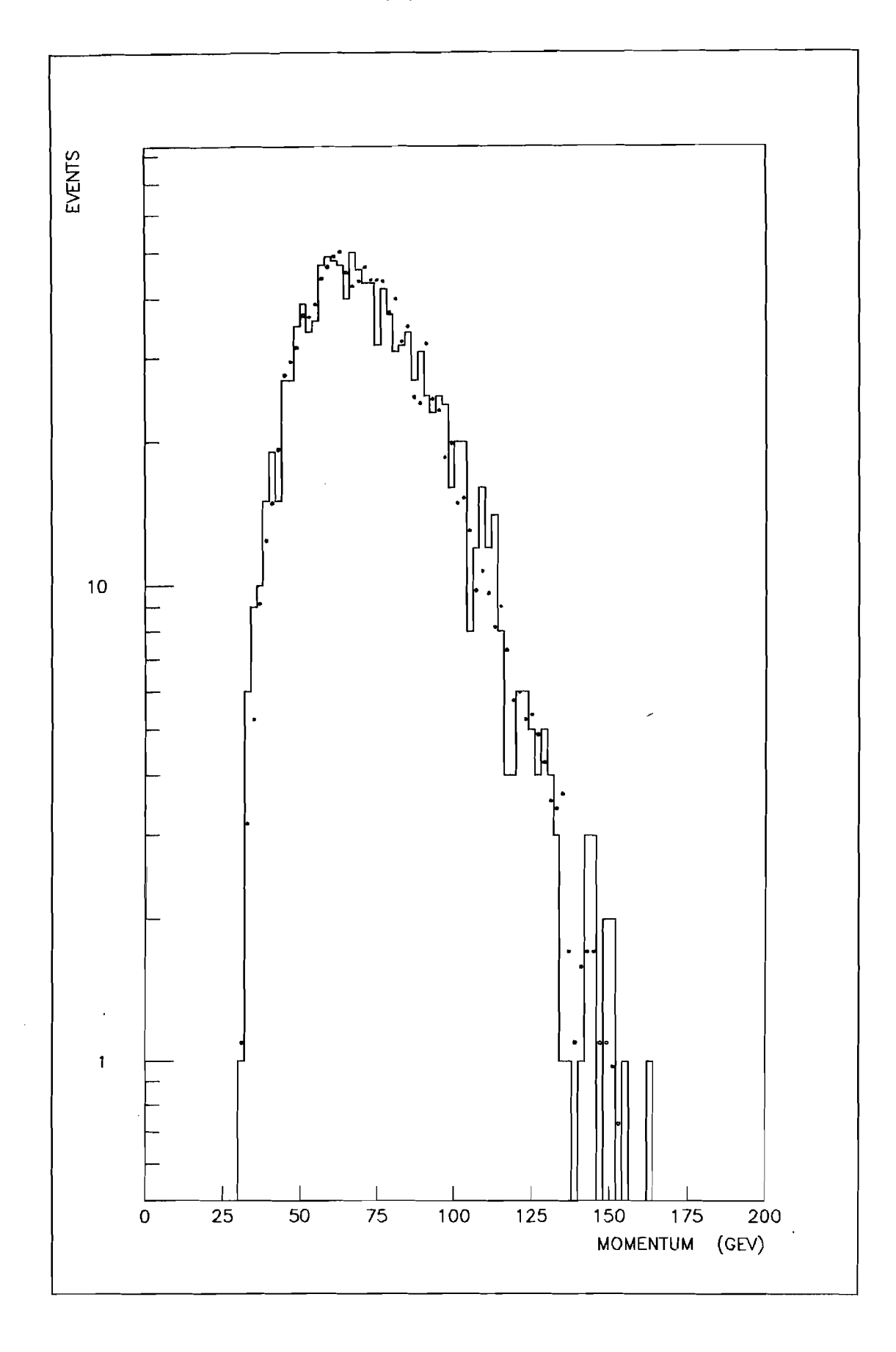
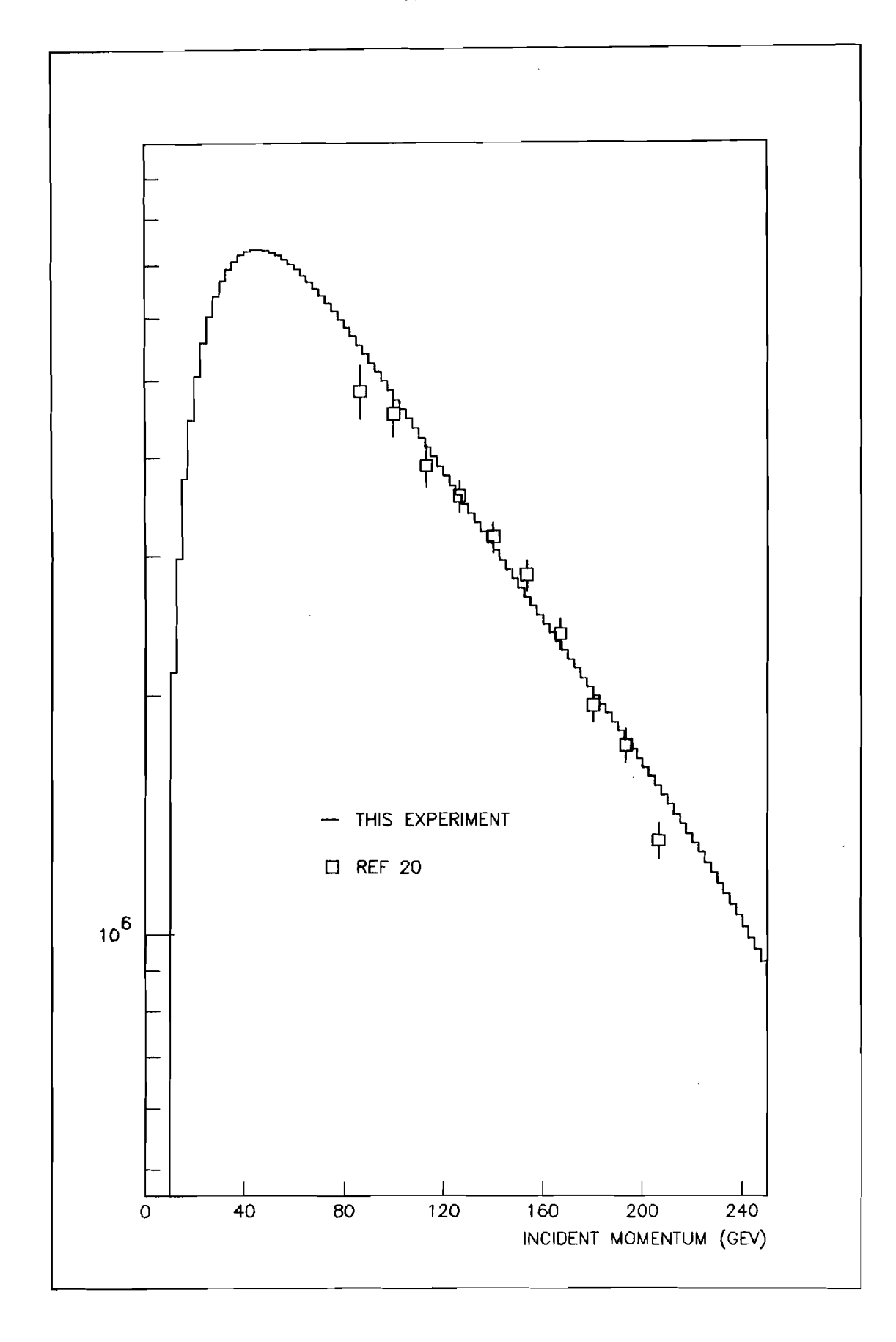


Figure 37. Comparison of momentum spectrum shape as deduced from Ke_3 events with the results of a previous measurement.



required to be greater than 10 GeV. The mass and transverse momentum distributions are shown in Figure 35. We selected events in the $\pi^+\pi^-$ mass range .48-.52 GeV and with t' < .002 GeV². In Figure 36, the momentum distribution for these events may be seen to agree with the Monte Carlo prediction based upon the fitted spectrum.

The spectrum shape is compared to the expected shape based upon a previous measurement in Figure 37. The data points come from a measurement of inclusive K_S production by 300 GeV protons on a berylium target at a production angle of .25 mrad.²⁰ The points have been scaled to our energy. The normalization is arbitrary. The effect of the small targeting angle is expected to be within the measurement error.

A global check of our understanding of the spectrum shape and of these decay modes was provided by a determination of the $K\pi_2$ and $K\pi_3$ branching ratios using the absolute flux as determined from the Ke_3 events, assuming the world average $K_L \rightarrow \pi e \nu$ branching ratio. Corrections were applied to account for the event selection procedures and systematic acceptance differences. These corrections and the results are shown in Tables 6 and 7. Both branching ratios were found to agree with the world averages.

TABLE 6 ${\tt CALCULATION~OF~THE}~K_L\!\!\to\!\!\pi^+\!\pi^-~{\tt BRANCHING~RATIO}$

	
Energy Range	40-120 GeV
Number of $K_L \rightarrow \pi^+ \pi^-$ decays	1142
Efficiency	$1.307 \times 10^{-8} \pm .013 \times 10^{-8}$
Incident Flux	$4.566 \times 10^8 \pm .059 \times 10^8$
Correction Factors	
Background subtractions	1.002±0.010
Pion absorption	1.012 ± 0.003
E/P event selection	1.025±0.005
Corrected branching ratio	1.99 × 10 ⁻³
Statistical error	0.06×10^{-3}
Systematic error	0.04×10^{-8}
World average branching ratio	2.03×10 ⁻⁸ ±0.05×10 ⁻⁸

^{*} Assumes b.r. $(K_L \rightarrow \pi e \nu) = .387 \pm .005$.

Energy Range	10-120 GeV
Number of $K_L \rightarrow \pi^+\pi^-\pi^0$ decays	5681
Efficiency	$8.506 \times 10^{-6} \pm .115 \times 10^{-6}$
Incident Flux"	$6.395 \times 10^8 \pm .083 \times 10^8$
Corrections Factors	
Background Subtractions	1.018±0.010
Pion absorption	1.012±0.003
E/P event selection	0.975±0.005
$\mathrm{b.r.}(\pi^0\!\!\to\!2\gamma)$	1.012±0.000
Photon losses	1.125±0.006
Corrected branching ratio	0.119
Statistical error	0.003
Systematic error	0.002
World average branching ratio	0.1239 ± 0.0020

^{**} Assumes b.r. $(K_L \to \pi e \nu) = .387 \pm .005$.

CHAPTER VI

EXTRACTION OF THE K° (890) RADIATIVE WIDTH

The K^{o} (890) is observed as a "resonance" with a relatively large intrinsic width and consideration of the line shape is important to the extraction of the radiative width. We now describe a theoretical model of the line shape and make a comparison with our data.

The finite width of the $K^{\sigma'}(890)$ may be accounted for by evaluating the production diagram (Figure 3) including the strong decay with the usual addition of an imaginary component to the pole in the propagator for the vector meson. In calculating the differential production cross section, the phase space for the observed final state, $K_S\pi^{\sigma}$, may be integrated out with the result:²¹

$$\frac{d\sigma}{dt dm} (K_L + A \to K_S \pi^0 + A) = \frac{d\sigma}{dt} (K_L + A \to K^* + A) \left[\frac{1}{\pi} \frac{m^2 \Gamma(K^* \to K_S \pi^0)}{(m^2 - m_0^2)^2 + (m_o \Gamma^{tot})^2} \right]$$
(6.1)

where the first factor is the narrow resonance production cross section, (2.1), considered now as a function of the mass m of the produced state. The covariant line shape is characterized by the central mass, m_o , and the total width, Γ^{tot} . The factor $\Gamma(K^* \rightarrow K_S \pi^0)$ is the partial width for the observed decay. We assume that the mass dependance of partial widths is given by

$$\Gamma \approx |g|^2 k^{2l+1} \tag{6.2}$$

where k is the rest frame decay momentum in the two body final state, with l=1 for both the p-wave $K\pi$ modes and the radiative mode, and the form factor, g, is a

function of k and hence depends on m. The functional dependance (6.2) is suggested by calculation of each decay partial width from a Lorentz covariant Born term.²² The form factor g accounts for finite size effects which produce a loss of coherence of the transition amplitude in the rest frame as the decay momentum k increases. We adopt the phenomenological prescription:

$$g(k) = \int_{\text{sphere}} dV e^{i\vec{k}\cdot\vec{x}} = \frac{3}{kR} (\cos kR - \frac{\sin kR}{kR})$$
 (6.3)

where R is a parameter representing the transition radius and is expected to be of order 1 fermi. Since the total width of the K^o (890) is dominated by the $K\pi$ channels and since the neutral and charged $K\pi$ channels are kinematically similar, $\Gamma(a^* \to K_S \pi^0)$ may be replaced by the total width if we suppress the branching ratio. Thus we have for K^o (890) production:

$$\frac{d\sigma}{dtdm} = 3\pi\alpha Z^2 \frac{\Gamma_o}{k_o^3} \frac{t - t_{min,o}}{t^2} |f_{C_o}|^2 BW(m); \qquad (6.4)$$

$$BW(m) = \frac{1}{\pi} \frac{m^{2} \Gamma^{tot}}{[m^{2} - m_{o}^{2}] + [m_{o} \Gamma^{tot}]^{2}} \left| \frac{g(k)}{g(k_{o})} \right|^{2}$$

$$\Gamma^{tot} = \Gamma^{tot}_{o} \left(\frac{q}{q_{o}} \right)^{3} \left| \frac{g(q)}{g(q_{o})} \right|^{2};$$

$$k = \frac{m^{2} - m_{K}^{2}}{2m};$$
(6.5)

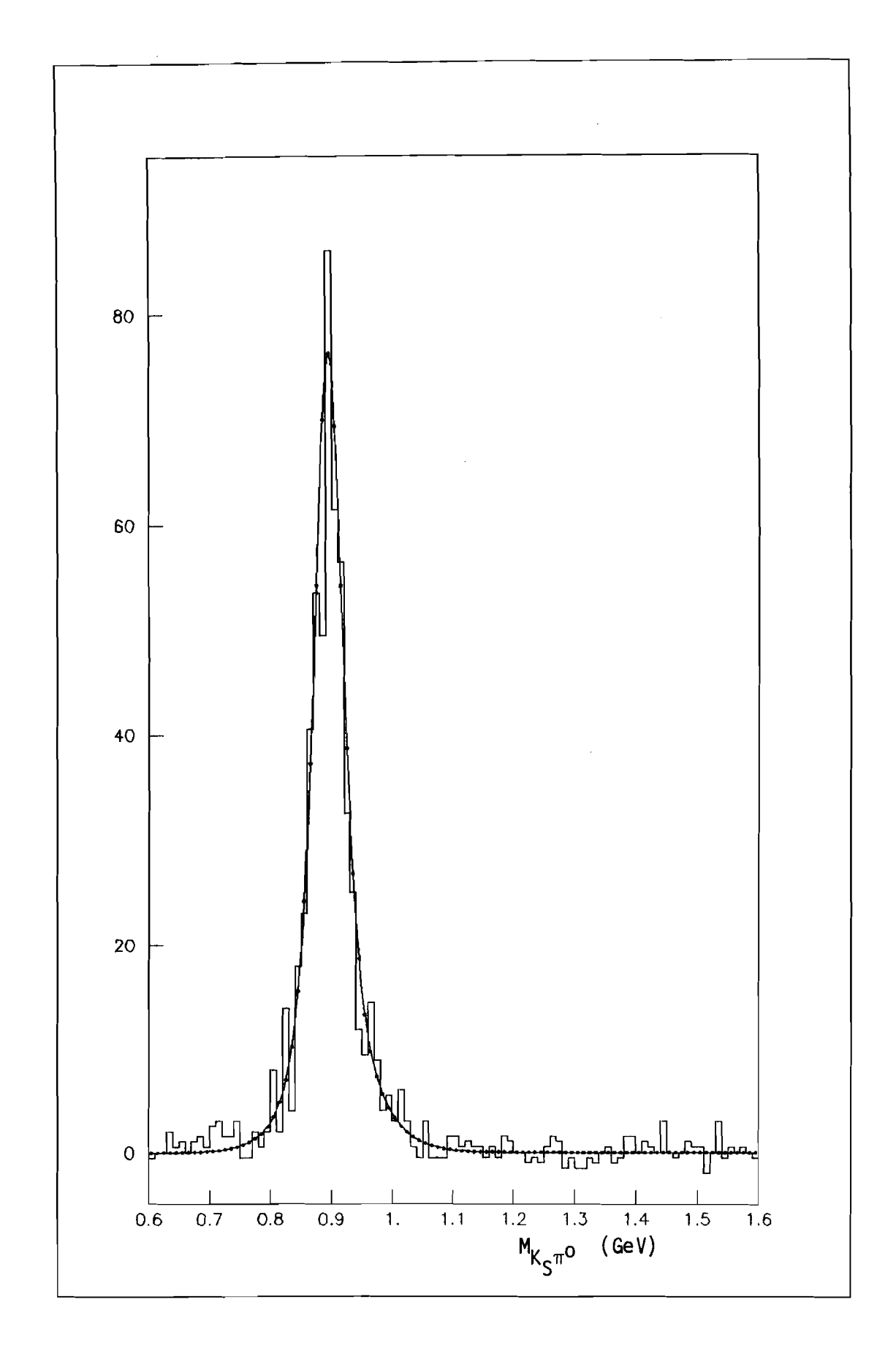
$$q^2 = [m^2 - (m_K + m_\pi)^2][m^2 - (m_K - m_\pi)^2]/4m^2$$

where the subscript o denotes quantities evaluated at the central mass m_o . The mass dependance of t_{\min} and of the nuclear form factor may be neglected. It should be pointed out that the assumption that the partial widths are mass independant is incompatible with our data and also with the minimal requirement that the production cross section vanish below the kinematic threshold for $K_S\pi^0$ production.

The $K_S\pi^0$ mass distribution for all events satisfying $t^*<.01~GeV^2$ is shown in Figure 38. The small neutron background was estimated from K_S wing events and subtracted. No evidence was seen for non resonant $K_S\pi^o$ production or for production of the K^o (1420). The distribution was therefore fit to the single resonance line shape given above. The line shape parameters included the total width Γ_o^{tot} , the mass m_o , and the transition radius R. In performing the fit, the theoretical line shape was convolved with a Gaussian mass resolution function with an energy averaged mass resolution as estimated by the Monte Carlo of 10.6 MeV. The result of the fit is shown superposed on the figure and the parameters were found to be $m_o=896.4\pm.6~{\rm MeV}$, $\Gamma_o^{tot}=49.8\pm1.4~{\rm MeV}$, and $R=1.1\pm.3~{\rm fermi}$. The resonance mass and width were found to be consistent with the world averages and the transition radius was of the expected size.

The K^0 '(890) radiative width was extracted by performing a fit to the energy averaged differential production cross section for each target. In order to minimize the effect of the uncertainty inherent in the phenomenological treatment of the line shape, we restricted further consideration to a small mass range (.8 - 1.0 GeV) symmetric about the central value m_o . The integral of the production cross section over this range has a weak dependance on the parameter R. The experimental differential cross sections were constructed by normalizing the number of $K_S\pi^0$ events in the mass range .8 - 10. GeV as described in the previous chapter. The event totals after the neutron background subtraction for $t' < .01 \text{ GeV}^2$ were 229 events and 355 events for the copper and lead targets respectively. We used the

Figure 38. Distribution of the $K_S\pi^0$ mass for events with $t'<.01\,GeV^2$. The result of a fit is superposed.



result of the fit to the mass shape to generate the mass distribution according to (6.5) in the Monte Carlo over the mass range .6 - 1.6 GeV. In this way, the effect of the mass cut .8-1.0 GeV, including resolution smearing, was incorporated into the efficiency relative to the integral of the line shape (6.4) over the mass range .6-1.6 GeV. This integral gives a correction factor C1=.8486 which was applied to the experimental differential cross section before comparing to the the narrow resonance formulae.

Forward strong and inelastic production were included in a fit to the resulting experimental differential cross section. The experimental cross section was fit to the form²³

$$\frac{d\sigma}{dt} = |\sqrt{\Gamma_o} T_C + e^{i\phi} \sqrt{C_S} T_S|^2 + \frac{d\sigma}{dt}$$

$$T_C = (3\pi\alpha Z^2/k_o^3)^{1/2} \frac{\sqrt{t'}}{t} f_C; T_S = 1 A \sqrt{t'} f_S; \frac{d\sigma}{dt'}$$
inelastic
$$= \alpha_A e^{-\beta t'}$$
(6.5)

The parameters of the fit were the radiative width Γ_o , the strong production coupling constant C_S , the relative phase ϕ , and target dependant normalizations α_A for the inelastic contributions. The inelastic cross sections were assumed to be characterized by a weak t' dependance determined by $\beta=8~GeV^{-2}$.

Expressions for the form factors f_C and f_S are given in Reference 23 and result from an optical model calculation of production in and about a nucleus described by a Wood-Saxon nuclear matter distribution. The nuclear radii, R_A , and skin thicknesses, a_A , were taken from electron scattering data ²⁴ to be $R_{Pb}=8.624 f$, $R_{Cu}=4.230 f$, $a_{Pb}=.582 f$, $a_{Cu}=.546 f$. The optical model calculations

tion accounts for nuclear absorption in the eikonal approximation: the effect of interactions with the individual nucleons in the nucleus is described by a complex refractive index which depends upon the K_L -nucleon total cross section σ_N and the ratio α of the real and imaginary parts of the K_L -nucleon forward elastic scattering amplitude. For purposes of this analysis, α was set to 0 and the value σ_N =17.3 millibarn was adopted in order to reproduce with the optical model the observed high energy K_L -heavy nucleus total cross sections.²⁵

Before being compared with the data, the theoretical expression (6.6) was averaged over the observed K^* energy spectrum. In addition, we accounted for the effect of resolution smearing in the variable t' by convolving the theoretical expression with a resolution function. For Gaussian transverse momentum resolution, the resolution smearing effect in t' may be expressed as

$$\frac{d\sigma}{dt} = \int d\vec{q}_i \frac{e^{-|\vec{q}_i - \vec{q}_i'|^2/2\Delta^2}}{2\pi\Delta^2} \frac{d\sigma}{dt'} = \frac{e^{-t' \cdot o/2\Delta^2}}{2\Delta^2} \int dt' \frac{d\sigma}{dt'} e^{-t' \cdot /2\Delta^2} I'(\left\{\frac{t' \cdot ot'}{\Delta^2}\right\}^{1/2})$$
(6.6)

where the subscript o denotes the observed value of the variable, I_o is the modified Bessel function of the first kind of order one, and the parameter Δ is the root mean square resolution in transverse three momentum. In case there is no intrinsic transverse momentum, one finds:

$$\frac{d\sigma}{dt'} = \delta(t') \rightarrow \frac{d\sigma}{dt'} = \frac{e^{-t' \cdot \sigma/2\Delta^2}}{2\Delta^2}$$
(6.7)

In Figure 39, the t' distribution for $K\pi_3$ decays is compared with the Monte Carlo and approximate exponential behavior is observed. The simulation slightly underestimated the transverse momentum resolution. The resolution for K^* events was

Figure 39. Transverse momentum distributions for $K_L \rightarrow \pi^+ \pi^- \pi^0$ decays for the two targets. The Monte Carlo prediction is superposed.

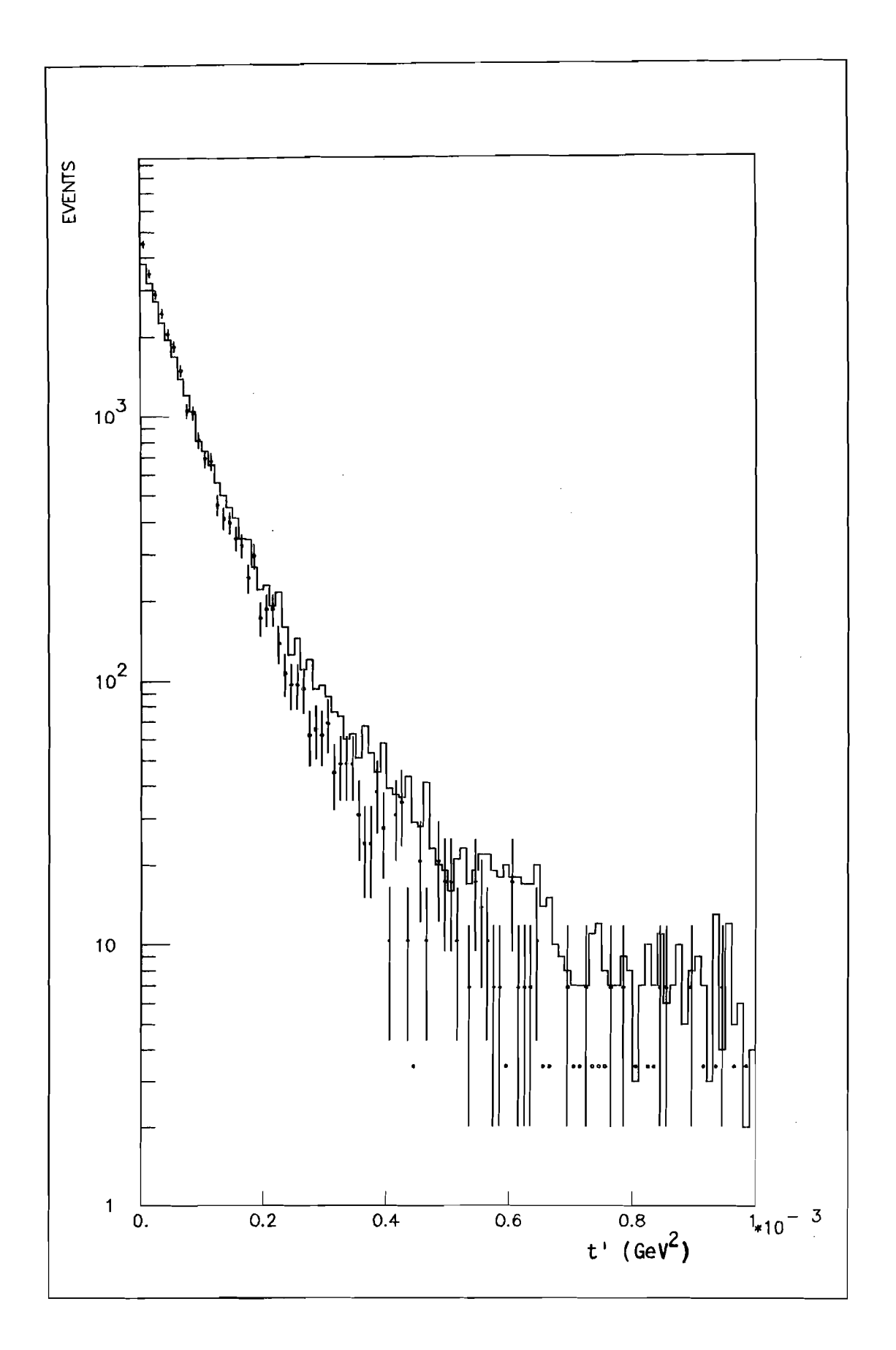


Figure 40. Experimental K^* differential production cross section for the copper target. The result of a fit described in the text is superposed.

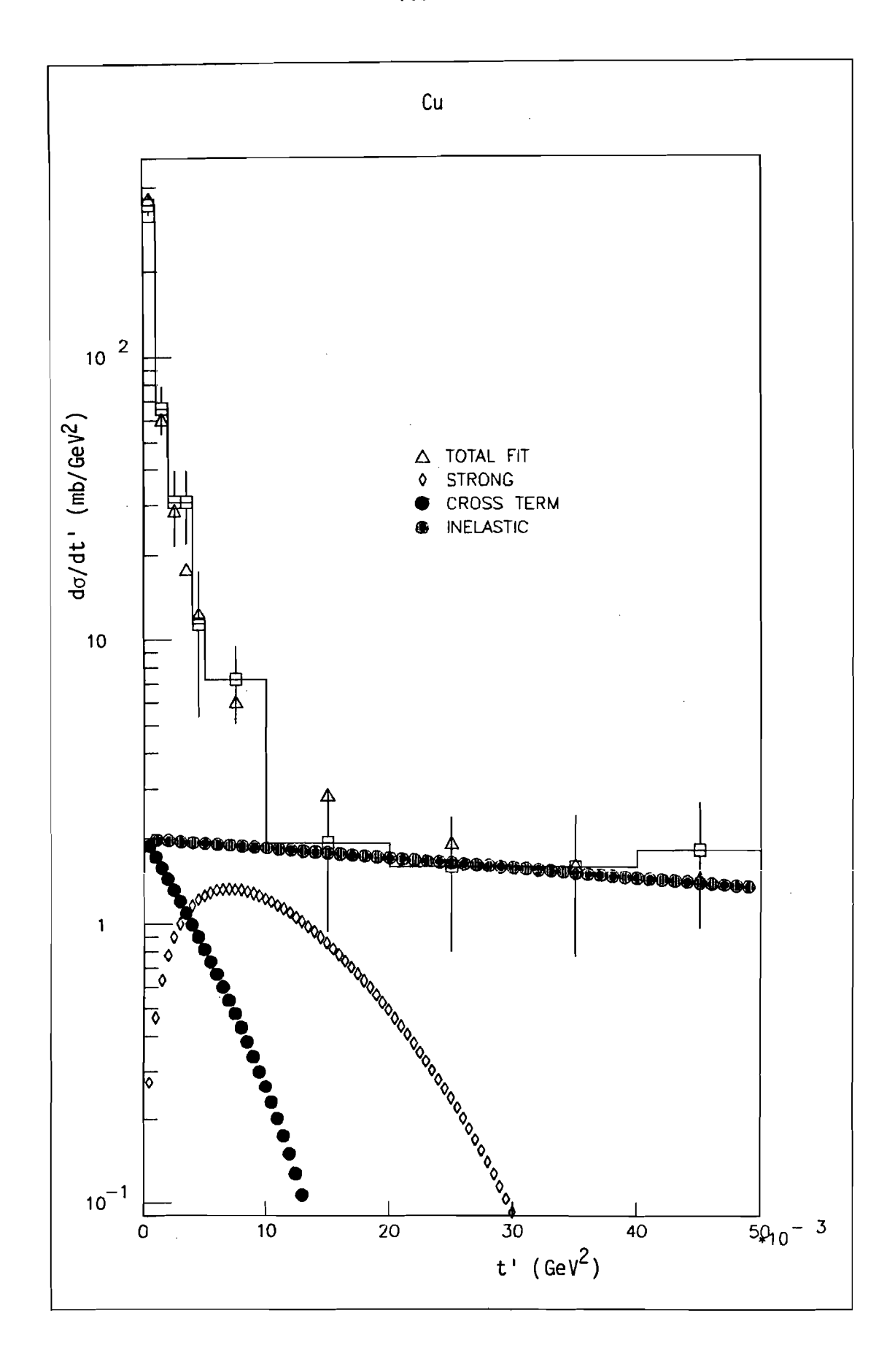


Figure 41. Experimental K^{\bullet} differential production cross section for the lead target. The result of a fit described in the text is superposed.

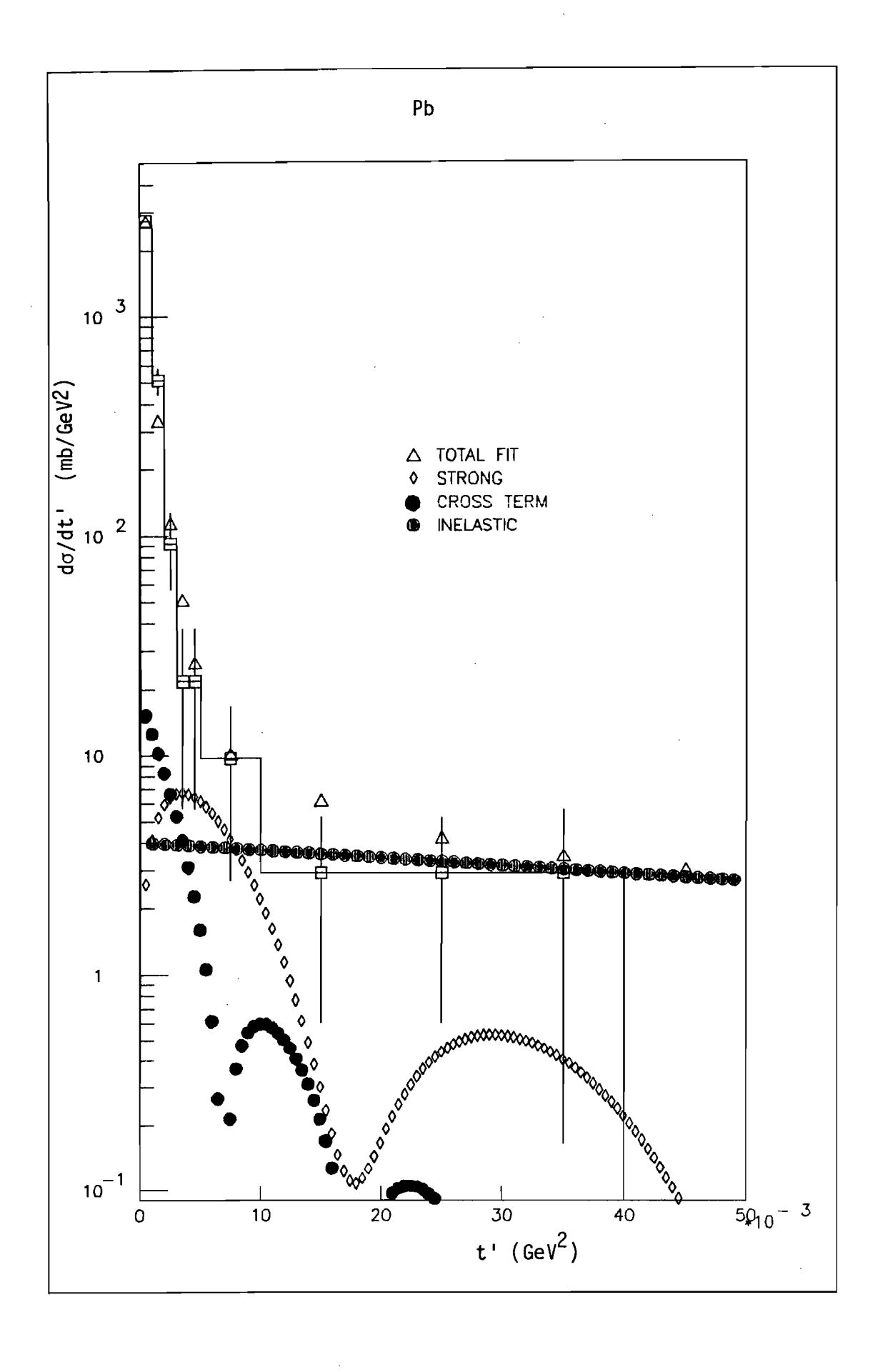
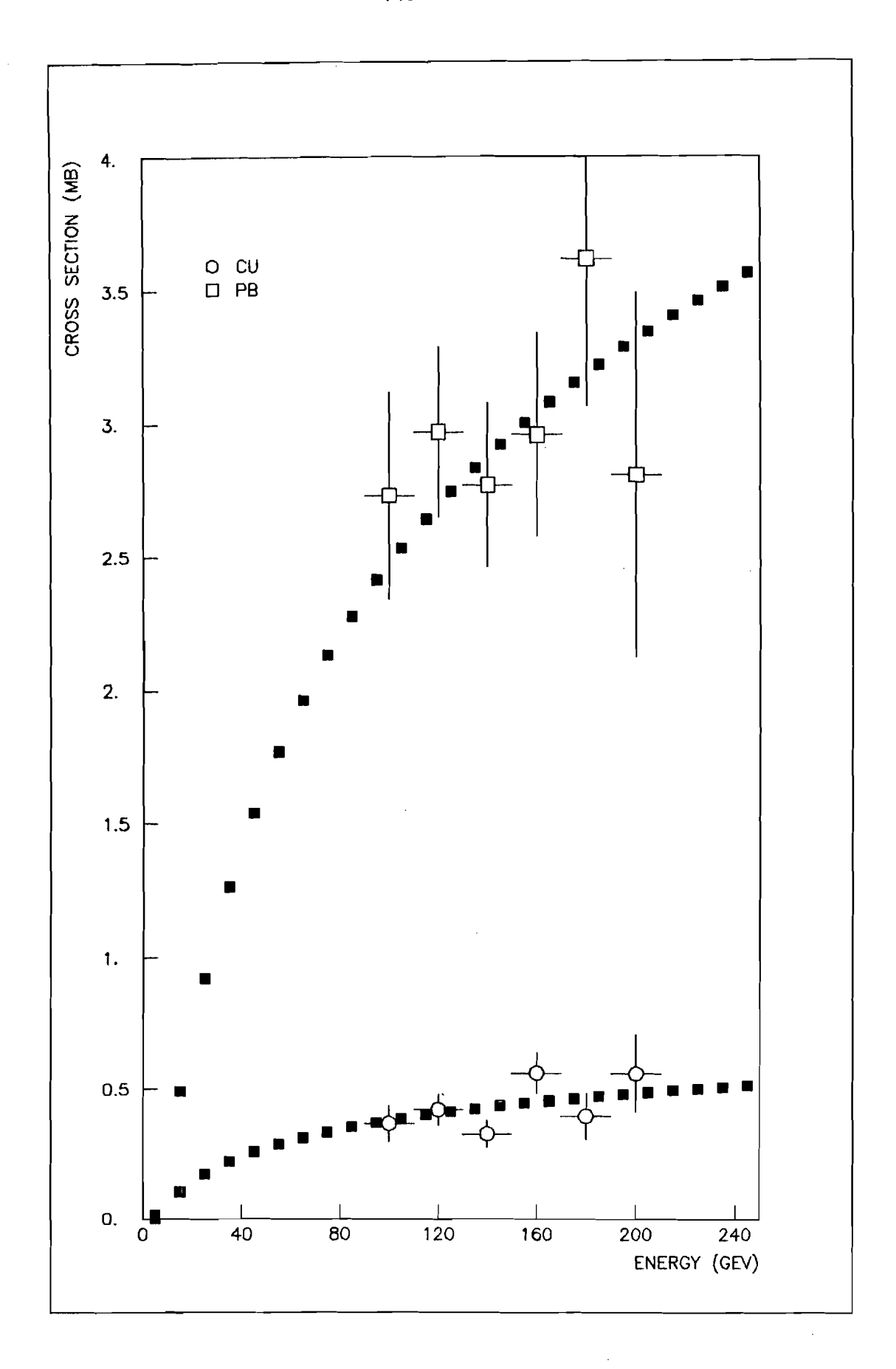


Figure 42. Energy dependance of the K^{o} (890) production cross section integrated from t'=0 to t'=.1 GeV^2 . The energy dependance expected for Coulomb production is superposed.



estimated from the Monte Carlo to be $\Delta^2=8\times 10^{-5}\,Ge\,V^2$. Increasing Δ^2 by the difference $(1\times 10^{-5}\,Ge\,V^2)$ between the data and Monte Carlo for the t' resolution for $K\pi_3$ events did not significantly alter the final result.

The experimental differential cross sections are shown in Figures 40 and 41. Fits to the cross sections were performed under a variety of assumptions with the results given in Table 8. First all parameters were allowed to vary and the fit was performed for the two targets separately and then for the two targets together, using the constraint the C_S and ϕ be independent of the target material. The number of parameters was reduced by fixing the inelastic contribution in Cu by the large t' behavior. The inelastic contribution for Pb was constrained to twice that for Cu. The parameter C_S was fixed by extrapolation from low energy data assuming that $C_S \approx 1/P_{lab}^0$. A two parameter fit for the radiative width and the phase was performed for the two targets together. The results of this last fit are shown superposed on the data in the figures. The contributions of the inelastic cross section, the strong cross section, and the interference term between the strong and Coulomb amplitudes are shown separately.

The radiative width was found to be independent of target and insensitive to the assumptions made in the fit. Although the parameters C_S and ϕ are not well determined by the data, the extrapolation of C_S from lower energy may be unreliable. The result of the fit to the two targets without constraints on the parameters was therefore adopted. The radiative width was found to be 116.5 ± 5.7 (statistical).

TABLE 8

RESULTS OF FITS TO THE DIFFERENTIAL CROSS SECTION

Γ	C_S	φ	α _{Cu}	α_{Pb}	χ^2 / d.o.f	Data used
(KeV)	(mb/GeV^2)	(radian)	(mb/GeV^2)	(mb/GeV^2)		in the fit
110.5±8.8	.296±.212	3.14±3.12	1.36±.41	•••	2.29/6	Cu
120.7±7.2	.016±.064	3.14±2.04		0.00±.08	10.9/6	РЬ
116.5±5.7	.096±.108	3.14±3.12	1.51±.42	0.00±.06	14.9/15	Cu + Pb
117.4±6.0	.52	1.73±.32	2.0	4.0	21.3/18	Cu + Pb#

[#] C_{S} , α_{C_4} and α_{P_b} constrained.

The results of the fit confirmed the expectation that the contribution due to strong production was small: the observed K' production at small t' was largely due to Coulomb production. This was corroborated by the energy dependance of the production cross section. In Figure 42, we exhibit the experimental cross section integrated from t'=0 to t'= 0.1 GeV^2 as a function of energy. The energy dependance expected in the Coulomb production model is shown superposed on the data points.

Estimates of systematic errors in the radiative width measurement are given in Table 9. The quantitative analysis of spectrum shape errors on our final result considered the effect of the statistical and systematic errors in the shape parameters on the ratio of the integral of the spectrum over the acceptance for K' events to the integral of the spectrum over the acceptance for $K\pi_3$ events. This ratio was determined numerically. It's variation with respect to the parameters describing the shape of the momentum spectrum was determined using the full covariance matrix of these parameters as determined by the fitting routine and the standard error was found to be 5.2 %, based on a sample of $2 \times 10^5 Ke_3$ decays. The variation in the ratio with respect to resolution was determined simply by comparing the results of fits obtained with different resolutions assumed in the Monte Carlo simulation. A 20% increase in the assumed drift chamber resolution changed the ratio by 1.4%.

Systematic error in the normalization would result if the spectrum shape differed between the K^{\bullet} and the charged mode data sets. It is important in this

TABLE 9
SYSTEMATIC ERROR ESTIMATES

Normalization	6.0 %	
Optical Model	3.0	
Mass Shape	1.5	
t' Resolution	1.1	
Normalization Correction Factors	0.7	
Total (in quadrature)	7.0 %	
·····	<u> </u>	

regard that the K' and charged data sets were obtained with the same proton targeting angle. Also, no significant difference in the momentum spectrum between the two beams was expected for a 0 degree targeting angle and variation of the spectrum across the beams was expected to be negligible. These assumptions were checked by a comparison of the observed momentum spectrum in different regions of the beams. No variation was observed. A further source of systematic error in the normalization was considered. The amount of neutron absorber, common to the two beams, was slightly larger for the K' running than for the charged mode running. A momentum dependance to the K_L absorption cross section could produce a spectrum shape difference. An estimate of the maximum expected cross section momentum dependance was based on the momentum dependance of the average of the K^+D and K^-D total cross sections.²⁷ The estimate for the corresponding normalization error is 1.5%. This effect was not included as a correction as the energy dependance of the total cross section on heavy nuclei appears to be moderated by inelastic screening effects. The statistical error in the $K\pi_3$ normalization sample and in the efficiencies and the uncertainty in the $K_L \rightarrow \pi^+ \pi^- \pi^0$ branching ratio were included in quadrature in the total normalization error.

The systematic error in the optical model calculation of nuclear absorption is dominated by uncertainty in the nuclear radius. It has been suggested that the neutron mean radius may exceed the mean proton radius in Pb by $\approx .5$ fermi. The Coulomb production amplitude is affected due to the absorption correction. The size of the effect was estimated by increasing the mean assumed charge radius

to the effective mean matter radius corresponding to this .5 fermi difference and found to be 2%. Uncertainties is the other optical model parameters also contribute to the error. The estimate of the error due to uncertainty in the mass shape corresponds to a .5 f decrease in the value of the transition radius as obtained from the fit to the mass shape. The effect of our incomplete understanding of the t' resolution for K' events was estimated by performing the fits to the t' distribution with a 20 % increase in the assumed resolution.

Adding in quadrature errors due to normalization, resolution, mass shape uncertainties, branching ratios, etc., we obtained a combined systematic error of 7.0%.

CHAPTER VII

SUMMARY AND CONCLUSIONS

Our final result for the K° (890) radiative width is $\Gamma(K^{\circ}$ (890) $\to K^{\circ} + \gamma$) =116.5±5.7 (statistical) ±8.1 (systematic) KeV. The only previous reported value for this quantity, 75±35 KeV, was obtained by a similar Coulomb production cross section measurement in the energy range 8-16 GeV (Reference 4) and the error in that case was dominated by systematic uncertainties in the identification of the Coulomb contribution to the total observed K^{o} (890) production. For the energy range of that experiment, coherent strong production was the dominant production mechanism. The radiative width was extracted by a simultaneous fit to the differential production cross sections for many nuclei. Systematic error may arise in this procedure due to the fact that the strong production amplitude is quite sensitive to the unknown details of the surface distribution on nucleons: the form factor f_S of the optical model amplitude depends upon the gradient of the nuclear matter density. In addition, the contribution of an isovector exchange amplitude, proportional to the neutron excess, was neglected in the analysis.²⁸ Our experiment was much less sensitive to these complications by virtue of the higher available beam energy.

Predictions for the radiative width of the K^{o} (890) on the basis of various

quark models and unitary symmetry ideas have ranged from 50 KeV to 250 KeV (Reference 2 and references therein). The model dependance of radiative width predictions may be alleviated by taking ratios. Of particular interest is the ratio of the radiative widths of the K^{o*} and K^{+*} . In the naive quark model, these two states are free of uncertainties due to SU(3) mixings and, in the radiative width ratio, phase space and spatial overlap factors are expected to cancel. In addition, symmetry-breaking effects are expected to be pronounced due to the presence of the strange quark. In the naive quark model, the ratio may be expressed in terms of quark moments alone:

$$\frac{\Gamma(K^{\circ}(890))}{\Gamma(K^{+\circ}(890))} = \left[\frac{\mu_{\circ} + \mu_{d}}{\mu_{\circ} + \mu_{u}}\right]^{2}$$
(1.4)

Combining the result of our measurement and of the result of the recent measurement of the K^+ (890) radiative width, 51 ± 5 KeV, the experimental radiative width ratio is $2.28\pm.29$. In the SU(6) limit, the theoretical prediction for this ratio is 4. The experimental ratio strongly suggests that symmetry breaking must be introduced. The direction of the required symmetry breaking is consistent with the hypothesis that the strange quark magnetic moment is reduced in relation to the moments of the up and down quarks by quark mass splitting. In the naive SU(6) quark model in which baryon magnetic moments are determined by the Dirac moments of the constituent quarks, the values $m_w=337$ MeV, $m_d=322$ MeV and $m_s=510$ MeV may be derived from the proton, neutron, and A magnetic moments.²⁹ The quark mass splitting is consistent with expectations based upon

hadron mass phenomenology: symmetry breaking is associated with a large strange quark mass and charge symmetry is respected by the approximate degeneracy of the up and down quarks. With these quark masses the radiative width ratio is predicted to be 1.64. If the spatial overlap factors are set equal to unity and relativistic phase space is assumed, equation (1.2) may be used to provide absolute predictions for the two radiative widths based upon the quark moments deduced from baryons. These predictions are 135 KeV for the radiative width of the K^{o} (890) and 82 KeV for the radiative width of the K^{+} (890).

It is interesting that the radiative width ratio may be predicted on the basis of baryon magnetic moments in a more model independant way. Within the context of the nonrelativistic quark model, relations between baryon magnetic moments have been derived which are independant of the angular momentum structure of the baryons. 30 Although the existing data does not determine all the free parameters of such a model, sum rules may be tested. In particular, using equations (6a) and (6b) of reference 30, one deduces the following equality:

$$\left[\frac{\Sigma^{-}+\Xi^{-}}{\Sigma^{+}+\Xi^{0}}\right] = \frac{\mu_{s}+\mu_{d}}{\mu_{s}+\mu_{u}}$$
(7.1)

where on the left-hand-side, the particle name denotes the corresponding magnetic moment. This equality is expected to hold under quite general assumptions whether or not there is a non s-wave component to the baryon wavefunctions. Thus the radiative width ratio may be expressed directly in terms of the experimental values for the hyperon magnetic moments appearing in (7.1) with no

values for the hyperon moments are used³¹, the radiative width ratio is predicted to be $2.51\pm.29$. The improved agreement with the experimental radiative width ratio over the naive SU(6) prediction support the idea that a successful interpretation of baryon magnetic moments in the context of a nonrelativistic quark model may require the assumption of configuration mixing.

Other interpretations of the deviations of the measured values of vector meson radiative widths and of baryon magnetic moments from the predictions of the naive quark model are possible. 32 Sea effects, relativistic and recoil effects, and corrections to the longwavelength approximation may play a role. The naive quark model is simply extended in quantum chromodynamics motivated bag and soliton models. Such quasirelativistic models suggest that the effective mass, m_q , of the naive model, is related to the total energy of the confined quark and does not represent the intrinsic mass alone.³³ It is easily shown that even a massless quark possesses a finite magnetic moment when confined in a spherical square well. The moment is, in that case, proportional to the confinement radius. The naive non relativistic quark model predictions are reproduced in such a model assuming small "current quark" masses and a common confinement scale. A complete understanding of vector meson radiative widths and of baryon magnetic moments awaits the development of a more refined theory of the static and quasistatic properties of hadronic matter.

APPENDIX A

CALCULATION OF RADIATIVE DECAYS IN THE QUARK MODEL

It is possible to give a relativistic quark model treatment of radiative decays, given a specific model of the spatial structure such as the bag or harmonic oscillator model. However we will restrict ourselves here to a non-relativistic treatment which gives simple results with the minimal number of assumptions.

The electromagnetic interaction of the j-th quark is given in the Pauli approximation by:

$$H_{interaction} = \frac{-e_j}{m_i} \vec{A}(\vec{x}_j) \cdot \vec{p}_j + \vec{\mu}_j \cdot \vec{B}(\vec{x}_j)$$
 (A.1)

where $\vec{\mu}_j$ is the quark magnetic moment operator. For transitions between eigenstates of the total spin, we may neglect the first term in the interaction and write the interaction Hamiltonian for a meson as:

$$H_{interaction} = \sum_{j} -\vec{\mu}_{j} \cdot \vec{B}(\vec{z}_{j})$$
 (A.2)

The amplitude describing a transition from an initial hadronic state h_i to a final hadronic state h_f with the emission of a photon described by a plane wave of wave vector \vec{k} and polarization vector $\vec{\epsilon}$ is:

$$H_{fi} = \langle h_f \mid \sum_{j} \vec{\mu}_{j} \cdot (\vec{\epsilon} \times \vec{k}) \left\{ \frac{2\pi}{\omega} \right\}^{1/2} e^{i\vec{k} \cdot \vec{x}_{j} - \omega t} | h_i \rangle \tag{A.3}$$

Because the meson states are considered as eigenstates of the relative quark orbital angular momentum, it is appropriate to change to center of mass coordinates:

$$\vec{r} = \vec{z}_1 - \vec{z}_2 \; ; \; \vec{R} = \frac{m_1 \vec{z}_1 + m_2 \vec{z}_2}{m} \; ; \; m = m_1 + m_2$$
 (A.4)

We write:

$$|h_i\rangle = |i\rangle e^{i\vec{p}_i\cdot\vec{R}-E_it}; \quad |i\rangle = |\chi_i\rangle \psi_i(r)$$
 (A.5)

where the internal wavefunction is expressed as a product of spin and space wavefunctions and E_i and \vec{p}_i are the total energy and momentum of the initial state. A similar wavefunction describes the meson in the final state. Changing variables and expanding the exponentials we obtain

$$H_{fi} = \langle h_{f} \left\{ \frac{2\pi}{\omega} \right\}^{1/2} e^{i(\vec{k} \cdot \vec{R} - \omega t)} \vec{\epsilon} \times \vec{k} \cdot \vec{M} | h_{i} \rangle \tag{A.6}$$

$$\vec{M} = (\vec{\mu}_1 + \vec{\mu}_2) + (\vec{\mu}_1 \frac{m_2}{m} - \vec{\mu}_2 \frac{m_1}{m}) i \vec{k} \cdot \vec{r} - (\mu_1 (\frac{m_2}{m})^2 + \mu_2 (\frac{m_1}{m})^2) (\vec{k} \cdot \vec{r})^2 + \dots$$
(A.7)

The first term in (A.7) is the spin magnetic moment operator $\vec{\mu} = \vec{\mu}_1 + \vec{\mu}_2$ and contributes to the M1 transition $J^P = 1^- \rightarrow J^P = 0^-$. In particular this operator describes the $K^{o*}(890) \rightarrow K^o + \gamma$ transition. The second term contributes to the M2 transition from the P-wave, spin triplet, tensor states ($J^P = 2^+ \rightarrow J^P = 0^-$), in particular the transition $K^{o*}(1430) \rightarrow K^o + \gamma$. The third term gives the $O(k^2)$ correction to the M1 amplitude. Considering the decay in the rest frame of the initial state, one obtains the S-matrix element:

$$S_{fi} = (2\pi)^4 \delta^4 (P_f + P_{\gamma} - P_i) \frac{M_{fi}}{\sqrt{2E_f} \sqrt{2m_i} \sqrt{2\omega}}$$
 (A.8)

where the invariant amplitude is identified as:

$$M_{i} = \sqrt{4\pi} \sqrt{2E_{i} 2m_{i}} \langle f | \vec{\epsilon} \times \vec{k} \cdot \vec{M} | i \rangle \tag{A.9}$$

The factor $\sqrt{2E_f \ 2m_i}$ arises from the noncovariant normalization of the wave functions. The radiative width is readily calculated using the formula:

$$\Gamma_{fi} = \frac{1}{32\pi^2 m_i^2} \sum |M_{fi}|^2 k d\Omega_k \tag{A.10}$$

One finds in the long wavelength approximation that the vector meson radiative width is given by:

$$\Gamma(V - P + \gamma) = \frac{4}{3} k^3 \frac{E_P}{m_V} |\vec{\mu}_{PV}|^2 |I_{PV}|^2$$

$$|\vec{\mu}_{PV}| = |\langle \chi_P | \vec{\mu}_1 + \vec{\mu}_2 | \chi_V \rangle| = |\mu_q - \mu_{\overline{q}}|$$

$$I_{PV} = \int d\vec{r} \ \psi_P^* \cdot \psi_V$$
(A.11)

where I_{PV} is the internal spatial wavefuction overlap integral, $k = \frac{(m_V^2 - m_P^2)}{2m_V}$ is the

rest frame decay momentum, and $E_P = \sqrt{m_P^2 + k^2} = \frac{1}{2} (1 + (\frac{m_P}{m_V})^2)$.

The radiative width of a tensor meson may be found by assuming wavefunctions for the initial and final states of the form:

$$|T> = |J=2, J_z=2> = |S=1, S_z=1> Y_{1,1}(\theta, \phi) f_T(r)$$
 (A.12)
 $|P> = |J=0, J_z=0> = |S=0, S_z=0> Y_{0,0}(\theta, \phi) f_P(r)$

where we have written out the space and spin factors explicitly. One finds:

$$\Gamma(T \to P + \gamma) = \frac{k^5}{30} \frac{E_P}{m_T} |\tilde{\mu}|^2 |r_{TP}|^2$$

$$|\tilde{\mu}| = |\langle S = 0, S_z = 0| \left\{ \mu_1 \vec{\sigma}_1 \frac{m_2}{m} - \mu_2 \vec{\sigma}_2 \frac{m_1}{m} \right\} |S = 1, S_z = 1 > |$$

$$r_{TP} = \frac{1}{4\pi} \int dV f_P^*(r) \cdot r \cdot f_T(r) |$$
(A.13)

where r_{TP} is the transition radius.

APPENDIX B

SEARCH FOR COULOMB PRODUCTION OF THE K (1430)

The Coulomb production formulae given in Chapter 2 encompass the production of more highly excited states of the K^0 than the K^0 (890). In particular, the K^0 (1430) state may be expected to be produced. The K^0 (1430) is a broad (full width = 100 MeV), tensor state ($J^P=2^+$) and is known to decay strongly to $K^0\pi^0$. In the naive quark model, this state is described as a bound state of an antistrange quark and a down quark with unit relative orbital angular momentum and with the quark spins aligned. The radiative transition K^0 (1430) $\to K^0 + \gamma$ is a magnetic quadrupole transition.

We found no evidence for the Coulomb production of this state. With reference to Figure 38 in which the $K_S\pi^0$ mass distribution is shown for events with t' $< .01 \text{ GeV}^2$, we observed 11 events in the mass range 1.32-1.52 GeV with a background of 9 ± 2 events estimated with events in the K_S wings. As the observed events were consistant with the background estimate, we could only derive an upper limit for K^0 (1430) production. The upper limit was derived under some simplifying assumptions. We neglected strong production and assumed that the production rate was given by the narrow resonance formula for the total Coulomb production cross section in the approximation that the nucleus was a completely absorbing "black sphere":

$$\sigma(K_L + A \to K^*(1430) + A) = 5\pi\alpha Z^2 \frac{\Gamma(K^* \to K + \gamma)}{k^3} \left\{ 2\ln \left[\frac{2}{\sqrt{t_{\min}} R_A} \right] - 2.154 \right\}$$
(B.1)

where R_A is the nuclear radius and the other factors are as defined for Equation (2.1) with 1.426 MeV as the mass of the produced particle. The nuclear radii were taken as $R_{Cu}=4.23$ f and $R_{Pb}=6.62$ f.

The normalization procedure was similar to that described in Chapter V. The efficiency was found with the Monte Carlo assuming in this case a decay angular distribution in the Gottfried-Jackson frame of the form:

$$\frac{dN}{d\Omega}(K^{0}(1430) \to K^{0}\pi^{0}) \approx |Y_{2,1} + Y_{2,-1}|^{2} \approx \sin^{2}\theta \cos^{2}\theta \sin^{2}\phi$$
 (B.2)

Our sensitivity to the K^0 (1430) radiative width was reduced relative to our sensitivity to the K^0 (890) radiative width by the $K^*(1430) \rightarrow K\pi$ branching fraction (.448) and by the difference in the values of the kinematic factors appearing in (B.1). After including the energy-averaged efficiency, the flux, the target nuclear number density, and the correction factors discussed in Chapter V, we calculated using (B.1) at the mean accepted production energy (145 GeV) a sensitivity of .0282 events/KeV and .0373 events/KeV for the copper and lead targets respectively. Combining the sensitivities of the two targets and assuming that the statistical error in the background estimate was uncorrelated with the statistical error in the signal, we derived an upper limit for the radiative width of the K^0 (1430) of 84 KeV (90% c.l.).

The upper limit may be compared with the radiative width of the K^+ (1430)which has been measured to be 240±45 KeV³⁴, in fair agreement with a prediction by J. Babcock and J. Rosner based upon unitary symmetry ideas and the Melosh transformation.³⁵ This same theory in fact predicts that the radiative width of the K^0 (1430) vanishes. However it is not obvious what effect symmetry breaking might have upon the predictions.

A naive quark model prediction for the radiative widths of the strange tensor mesons incorporating symmetry breaking effects may be simply derived (see Appendix A). In the longwavelength approximation, the amplitude for the magnetic quadrupole transition between meson states for which the total quark spin S is a good quantum number (ie. assuming LS coupling) is in the notation of Chapter 1 and Appendix A:

$$M_{TP} = \langle T \middle\{ \mu_1 \vec{\sigma}_1 \frac{m_2}{m} - \mu_2 \vec{\sigma}_2 \frac{m_1}{m} \middle\} i \vec{k} \cdot \vec{r} \middle| P \rangle$$
 (B.3)

which may be compared with the magnetic dipole amplitude:

$$M_{VP} = \langle V \Big| \mu_1 \vec{\sigma}_1 + \mu_2 \vec{\sigma}_2 \Big| | P \rangle$$
 (B.4)

From these two expressions, the ratio of the neutral and charged tensor meson radiative widths may be deduced by inspection. Assuming that the spatial wavefunctions in the neutral and charged states are the same, in the ratio of the radiative widths, the matrix element of the relative quark coordinate operator, r, cancels. Hence the transition amplitude ratio is determined by the spin matrix element just as in the vector meson case and, aside from the simple quark mass factors, the tensor and vector meson transition operators differ only in the relative sign of the amplitudes for each of the two quarks. Because we assume that the quark spin wavefunction is common to the vector and tensor states, we may write down the tensor meson radiative width ratio by analogy to the vector meson case:

$$\frac{\Gamma(K^{0}(1430) \to K^{0}\gamma)}{\Gamma(K^{+}(1430) \to K^{+}\gamma)} = \left[\frac{\mu_{s}m_{d} - \mu_{d}m_{s}}{\mu_{s}m_{u} - \mu_{u}m_{s}} \frac{m_{s} + m_{u}}{m_{s} + m_{d}}\right]^{2}$$
(B.5)

If the quark mass are deduced from baryon magnetic moments, the ratio is predicted to be .054 and if the measured value of the K^+ (1430) radiative width is taken as input, the K^0 (1430) radiative width is predicted to be 13 KeV, in agreement with our upper limit. Explicit calculation in the naive quark model of the tensor meson radiative width yields:

$$\Gamma(T \to P + \gamma) = \frac{k^5}{30} \frac{E_P}{m_T} |\tilde{\mu}|^2 |r_{TP}|^2$$

$$|\tilde{\mu}| = |\langle S = 0, S_z = 0| \left\{ \mu_1 \vec{\sigma}_1 \frac{m_2}{m} - \mu_2 \vec{\sigma}_2 \frac{m_1}{m} \right\} |S = 1, S_z = 1 > |$$

$$r_{TP} = \frac{1}{4\pi} \int dV f_P^*(r) \cdot r \cdot f_T(r)$$
(A.13)

where r_{TP} is the transition radius. Assuming the aforementioned quark masses and a transition radius of 1 fermi, the naive quark model predicts a K^+ (1430) radiative width of 174 KeV and a K^0 (1430) radiative width of 9.4 KeV. In the SU(6) symmetry limit, the naive quark model predicts that the radiative width of the K^0 (1430) vanishes, in agreement with the prediction of J. Babcock and J. Rosner. The disparity between the radiative widths of the neutral and charged states even

when symmetry breaking is allowed may be understood in the naive model as a consequence of the destructive interference of the transition amplitudes for the two quarks. The agreement between the experimental results and the theoretical predictions confirms this simple picture.

REFERENCES

- 1. C. Becchi and G. Morpurgo, Phys. Rev. 140B, 687 (1965).
- 2. P. J. O'Donnell, Rev. Mod. Phys. <u>53</u>, 673 (1981).
- J. L. Rosner, in High Energy Physics-1980, proceedings of the XXth International Conference, Madison, Wisconsin, edited by L. Durand and L. G. Pondrom (AIP, New York, 1981).
- 4. W. C. Carithers et al., Phys. Lett. 35, 349 (1975).
- C. Chandlee et al., Phys. Rev. Lett. <u>51</u>,168 (1983);
 D. Berg et al., Phys. Lett. <u>99</u>B, 119 (1981).
- 6. A. Halprin, C. M. Anderson and H. Primakoff, Phys. Rev. 152, 1295 (1966).
- 7. H. Primakoff, Phys. Rev. <u>81</u>, 899 (1951).
- 8. T. Jenson et al., Phys. Rev. D27, 26 (1983);
 - G. Berlad et al., Annals of Phys. <u>75</u>,461 (1973);
 - C. Bemporad et al., Nucl. Phys. <u>B51</u>, 1 (1973);
 - G. Morpurgo, Nuovo Cimento 31, 569 (1964).
- 9. K. Gottfried and J. D. Jackson, Nuovo Cimento 33, 309 (1964).
- 10. J. D. Jackson, Nuovo Cimento 34, 1644 (1964).
- 11. B. Winstein, L. S. Littenberg (private communication).
- 12. L. Stodolsky, Phys. Rev. 144, 1145 (1966).

- 13. R. H. Bernstein et al. (to be published).
- 14. D. P. Coupal, Ph.D. thesis, University of Chicago (unpublished).
- H. J. Frisch et al., IEEE Transactions on Nuclear Science, vol. NS-27,150 (1980).
- 16. Particle Data Group, Phys. Lett. 111B, 1 (1982).
- 17. CERNLIB, subroutine W601.
- 18. Y. S. Tsai, Rev. Mod. Phys. 46, 815 (1974).
- 19. C. Y. Chien, Phys. Lett. 35B, 261 (1971).
- 20. P. Skubic et al., Phys. Rev. D 18, 3115 (1978).
- 21. J. D. Jackson and H. Pilkuhn, Nuovo Cimento 33, 906 (1964).
- C. Quigg and F. von Hippel in Experimental Meson Spectroscopy, edited by
 C. Baltay and A. H. Rosenfeld (Columbia University Press, New York, 1970).
- 23. G. Faldt et al., Nucl. Phys. <u>B41</u>, 125 (1972);
 - G. Faldt, Nucl. Phys. <u>B43</u>, 591 (1972).
- 24. C. W. De. Jager et al., Atomic Data and Nuclear Data Tables 14,479 (1974).
- 25. A. Gsponer et al., Phys. Rev. Lett. 42, 9 (1979).
- 26. W. Molzon, Ph.D. thesis, University of Chicago (unpublished).
- 27. A. S. Carroll et al., Phys. Lett. 61 B,303 (1979).
- 28. A. N. Kamal and G. L. Kane, Phys. Rev. Lett. 43 551 (1979).

- 29. F. E. Close, Introduction Quarks and Partons, (Academic, New York, 1979).
- R. G. Sachs, Phys. Rev. D <u>23</u>, 1148 (1981);see also
 L. Brekke and R. G. Sachs., Phys. Rev. D <u>28</u>, 1178 (1983).
- 31. The Σ⁻ moment (-1.10±.03 n.m.) is taken as the average of two recent measurements: L. Deck et al., Phys. Rev. D 28, 1 (1983) (Σ⁻=-.89±.14) and D. W. Hertzog et al., Phys. Rev. Lett.,
 51, 1131 (1983) (Σ⁻=-1.111±.031±.011).
- 32. J. Franklin, Phys. Rev. D <u>29</u>, 2648 (1984).
 M. Betz and R. Goldflam, Phys. Rev. D <u>28</u>, 2848 (1983);
 J. Parmentola, Phys. Rev. D <u>29</u>, 2563 (1984).
- 33. T. D. Lee, Particle Physics and Introduction Field Theory
 (Academic, New York, 1981).
- 34. S. Cihangir et al., Phys. Lett. 117B, 123 (1982).
- 35. J. Babcock and J. Rosner, Phys. Rev. D 14, 1286 (1976).

_
_
•
•
_
•
—
•
•
•
_
_